İZMİR KÂTİP ÇELEBİ ÜNİVERSİTESİ
2010
GRADUATE SCHOOL OF NATURAL AND APPLIED SCIENCES

Optimization of Nb-Ti-B Master Alloy in Aluminum A356 Parts with General Factorial and Neuro-Regression

Submitted to the Graduate School of Natural and Applied Sciences in partial fulfillment of the requirements for the degree of

Master of Science

in Material Science & Engineering

by

Batuhan Doğdu

ORCID 0000-0003-4110-7341

July, 2023

This is to certify that we have read the thesis **Optimization of Nb-Ti-B Master Alloy in Aluminum A356 Parts with General Factorial and Neuro-Regression** submitted by **Batuhan Doğdu**, and it has been judged to be successful, in scope and in quality, at the defense exam and accepted by our jury as a MASTER'S THESIS.

APPROVED BY:

Advisor: **Assoc. Prof. Onur Ertuğrul**
İzmir Kâtip Çelebi University

Co-advisor: **Assoc. Prof. Levent Aydın**
İzmir Kâtip Çelebi University

Committee Members:

Assoc. Prof. Mertol Gökelma
İzmir Institute of Technology

Assistant Prof. Bahadır Uyulgan
İzmir Dokuz Eylül University

Assistant Prof. İsmail Doğan Külcü
İzmir Kâtip Çelebi University

Date of Defense: July 24, 2023

Declaration of Authorship

I, **Batuhan Doğdu**, declare that this thesis titled **Optimization of Nb-Ti-B Master Alloy in Aluminum A356 Parts with General Factorial and Neuro-Regression** and the work presented in it are my own. I confirm that:

- This work was done wholly or mainly while in candidature for the Master's degree at this university.
- Where any part of this thesis has previously been submitted for a degree or any other qualification at this university or any other institution, this has been clearly stated.
- Where I have consulted the published work of others, this is always clearly attributed.
- Where I have quoted from the work of others, the source is always given. This thesis is entirely my own work, with the exception of such quotations.
- I have acknowledged all major sources of assistance.
- Where the thesis is based on work done by myself jointly with others, I have made clear exactly what was done by others and what I have contributed myself.

Date: 6.07.2023

Optimization of Nb-Ti-B Master Alloy in Aluminum A356 Parts with General Factorial and Neuro-Regression

Abstract

The grain refinement process applied as a strengthening mechanism in Al-Si casting alloys is of critical importance in the case of A356 alloy, which is mainly used in the automotive industry. Following the fading and poisoning effects caused by the use of Ti-B-containing grain refiners, researchers have been searching for a new grain refiner composition. After the positive effects of the Nb-B containing grain refiner master alloy, which has been studied in detail in recent years, were observed, but these effects did not produce any significant results, studies on the Nb-Ti-B ternary composition were carried out, and it was revealed that the grain refining effectiveness increased and the optimum Nb-Ti-B values were proportionally revealed by thermodynamic calculations. However, since these values have not been analyzed from a statistical point of view with real-time tensile test data, this gap in the literature has been filled with this study. In this study, the elemental ratios of Nb, Ti and B were determined using a factorial experimental design approach and the castings were completed in a laboratory environment where the casting parameters could be precisely maintained at boundary conditions. The tensile test results were processed and compared with the optimization data using general factorial regression in Minitab 20 and neuro-regression in Mathematica, an innovative data processing technique that combines machine learning and regression analysis. In addition, chemical analysis with OES, XRF methods, microstructure analysis with optical metal microscopy and SEM, phase analysis on selected samples with XRD method and metallographic findings are shared. According to the results obtained, while the optimum composition could not be explained with a statistical consistency with the general factorial regression method,

the phenomenon in which the effect of Nb, Ti and B elements on the tensile test of A356 alloy was revealed with neuro-regression, with R2 = 0.999 without data memorization. Since that step of the work may be called as preliminary study, there are plenty of rooms and opportunities for enhancement of the model with feedbacked tensile test data.

Keywords: A356 alloy, grain refinement, optimization, Al-Nb-Ti-B

Alüminyum A356 Parçalarda Nb-Ti-B Master Alaşımının Genel Faktöriyel ve Sinirsel Regresyon ile Optimizasyonu

Öz

Al-Si döküm alaşımlarında bir güçlendirme mekanizması olarak uygulanan tane inceltme işlemi, ağırlıklı olarak otomotiv endüstrisinde kullanılan A356 alaşımı söz konusu olduğunda kritik bir öneme sahiptir. Ti-B içeren tane incelticilerin kullanımının neden olduğu solma ve zehirlenme etkilerinin ardından, araştırmacılar yeni bir tane inceltici bileşimi arayışına girmişlerdir. Son yıllarda detaylı olarak çalışılan Nb-B içeren tane inceltici ana alaşımın olumlu etkilerinin görülmesi ancak bu etkilerin kayda değer bir sonuç üretmemesi üzerine Nb-Ti-B üçlü bileşimi üzerinde çalışmalar yapılmış ve tane inceltme etkinliğinin arttığı ve optimum Nb-Ti-B değerlerinin oransal olarak ortaya çıktığı termodinamik hesaplamalarla ortaya konmuştur. Ancak bu değerler gerçek zamanlı çekme testi verileri ile istatistiksel açıdan analiz edilmediği için literatürdeki bu boşluk bu çalışma ile doldurulmuştur. Bu çalışmada, Nb, Ti ve B element oranları faktöriyel deneysel tasarım yaklaşımı kullanılarak belirlenmiş ve dökümler, döküm parametrelerinin sınır koşullarda hassas bir şekilde korunabildiği bir laboratuvar ortamında tamamlanmıştır. Çekme testi sonuçları, Minitab 20'de genel faktöriyel regresyon ve makine öğrenimi ile regresyon analizini birleştiren yenilikçi bir veri işleme tekniği olan Mathematica'da nöral regresyon kullanılarak işlenmiş ve optimizasyon verileri karşılaştırmalı analize tabii tutulmuştur. Ek olarak, OES, XRF yöntemleri ile kimyasal analiz, optik metal mikroskobu ve SEM ile mikroyapı analizi, XRD yöntemi ile seçilen numuneler üzerinde faz analizi ve metalografik bulgular paylaşılmıştır. Elde edilen sonuçlara göre, optimum alaşım kompozisyonu genel faktöriyel regresyon yöntemi ile istatistiksel bir tutarlılıkla açıklanamazken, Nb, Ti ve B elementlerinin A356 alaşımının çekme testi üzerindeki etkisinin nöro-regresyon ile veri ezberleme

olmaksızın R2 = 0,999 ile ortaya konduğu olgu ortaya konmuştur. Çalışmanın bu aşaması ön çalışma olarak adlandırılabileceğinden, modelin geri beslemeli çekme testi verileriyle geliştirilmesi için pek çok alan ve fırsat bulunmaktadır.

Anahtar Kelimeler: A356 alaşımı, tane inceltme, optimizasyon, Al-Nb-Ti-B

I dedicate it to myself, who hesitated to do a PhD after his master's thesis, but who completed his PhD and took this thesis in his hand and looked at this page in near future...

Acknowledgement

I would like to express my endless gratitude to my esteemed teacher, Associate Professor Dr. Onur Ertuğrul, with whom I had the chance to work together since the undergraduate education period, and to Associate Professor Dr. Levent Aydın, who helped me to add a different perspective to my study with his mentorship. In addition, I would like to express my gratitude to CMS Jant and Makina Sanayi for supporting me to realize the study, to Mr. Ömer Burak Çe, Senior Manager of R&D and Laboratory, who always stood behind me in the problems I encountered, to Caner Kalender, who was with me at every moment with his support during the complicated laboratory process of the study, and to all my friends in my R&D department who took my workload from me during the thesis writing process. Finally, I would like to send my greetings to Mr. Emre Çubuklusu, who has imposed the R&D mentality on me, has always managed to keep my motivation at the highest level and has always managed to keep me locked on the target with the right guidance.

Even though they are far away from me, I would like to thank my brother Oğuzhan and my mother for their motivation and moral support during this process.

I would like to dedicate this study to my best friend, my girlfriend and my future wife Melis, who has given me the greatest support in this whole master thesis process. I expect the same support from her in my PhD study.

Table of Contents

List of Figures

List of Tables

List of Abbreviations

SEM	Scanning Electron Microscope
TEM	Transmission Electron Microscope
XRF	X-Ray Fluorescence
DoE	Design Of Experiment
R	Run Order
Q	Growth Restriction Factor
RPT	Reduce Pressure Test
OES	Optical Emission Spectroscopy
EDS	Energy Dispersive Spectroscopy
ANN	Artificial Neural Network
Ppm	Part per million
NM	Nelder-Mead Algorithm
DE	Differential Evolution Algorithm
SA	Simulated Annealing Algorithm
RS	Random Search Algorithm
YS	Yield Strength
TS	Tensile Strength
%E	Elongation
QI	Quality Index
Al	Aluminum
Si	Silicon
Mg	Magnesium

Cu	Copper
Mn	Manganese
Zn	Zinc
Na	Sodium
Sr	Strontium
Nb	Niobium
Ti	Titanium
B	Boron

List of Symbols

ε	Total strain
σ	Stress
μ	micron
σy	Yield stress [MPa]
σt	Tensile stress [MPa]
ΔH	Enthalpy Change
ΔS	Entropy Change
$\Delta G v$	Net Bulk Free Energy
α	Alpha Phase
θ	Theta Degree
β	Beta phase

Chapter 1

Literature Overview

1.1 Aluminum and Aluminum Alloys

The term "aluminum" originated from the word "alumen", which refers to the Greek alum mineral. Initially procured in an impure form by Hans Christian Örsted in 1825, it was later isolated as a pure element by Wöhler in 1827. The industrial production of aluminum began in 1886 when Charles Martin Hall at USA and Paul T. Heroult in France independently conducted electrolysis. The invention of Werner von Siemens' dynamo in 1886 and K.J.Bayer's development of the Bayer process, which enabled the production of alumina from bauxite, simplified large-scale aluminum production, making it the second most utilized metal worldwide, following iron and steel.

Aluminum, represented by the symbol Al, has an atomic number of 13 and an atomic weight of 27. With a density of 2.7g/cm3, aluminum has a melting point of 660°C. When alloyed, its pure tensile strength of around 49 MPa can increase to 700 MPa. Additionally, it possesses excellent corrosion resistance due to the protective oxide layer that forms on its surface.

Aluminum is the most abundant metal on Earth and the third most abundant element behind silicon and oxygen in the planet's crust. It is typically found as aluminum oxide and in other combined forms. Bauxite, the ore containing aluminum compounds, is a form of hydrated aluminum oxide.

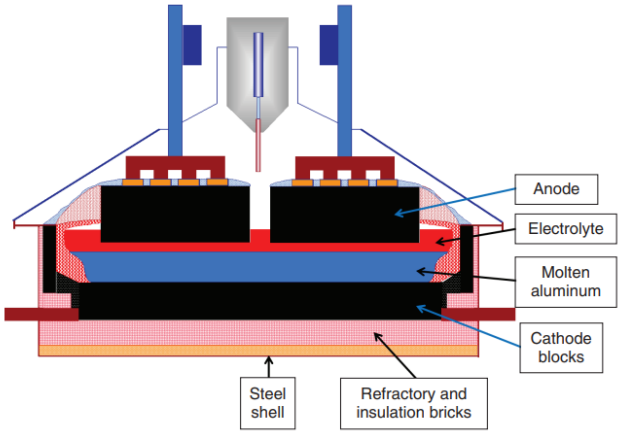

Figure 1.1: Representation of the electrolysis process[1].

The process of aluminum production occurs in two phases. In the initial phase, the Bayer method is employed to derive alumina from bauxite ore. During the subsequent phase, electrolysis is utilized to produce aluminum from the alumina. Aluminum's global abundance is accompanied by a multitude of exceptional attributes, such as low density, efficient heat conduction, ductility, impressive corrosion and oxidation resistance, elevated electrical and thermal conductivities, significant reflectivity, non-magnetic properties, recyclability, and affordability.

Pure aluminum is generally not applied directly because it cannot effectively exhibit its characteristics; instead, aluminum is combined with other elements through alloying. Common alloying components include manganese, silicon, zinc, copper, tin, and magnesium. There are two primary categories of aluminum alloys: wrought aluminum alloys and cast aluminum alloys, with each further subdivided into heat treatable and non-heat treatable classes. A classification of the cast and wrought alloys, based on their alloying constituents, is presented in Figure 1.2.

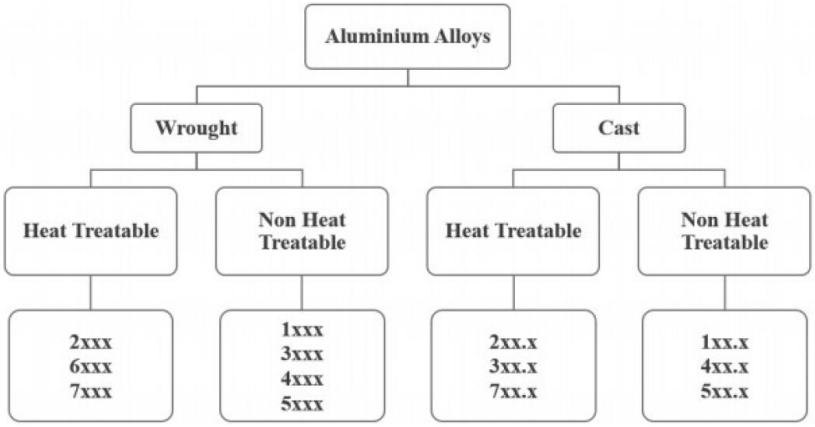

Figure 1.2: Classification of Aluminum Alloys [2].

1.1.1 Cast Aluminum Alloys

Aluminum is a very suitable metal for the casting industry. A low melting point is used in casting processes due to its low density. Aluminum also castable by the sand, investment, die casting process. Reasons for using aluminum alloys in casting processes:

- Low melting point
- Low density
- Good mechanical properties
- Good chemical stability
- High heat conductivity
- Good surface quality
- Dimensional stability
- Good elongation values
- High heat conductivity

Based on the selection of casting techniques for aluminum alloys, constraints in section thickness may present challenges both on the component's surface and in the microstructure as a result of the solidification time's influence on intricate geometric configurations.

A number of aluminum casting alloys can achieve exceptionally elevated mechanical properties through heat treatment. Additional methods to enhance the mechanical properties of aluminum casting alloys encompass eutectic modification, grain size refinement and control of impurity level. Final properties that cause the use of aluminum casting alloys: machinability, hardness, mechanical properties, corrosion resistance, specific strength.

Aluminum alloys are the most commonly used aluminum alloys in the casting industry. Aluminum silicon alloys are indicated with the code 4xxx.x in the casting alloys classification or 3xxx.x if the alloy contains Magnesium or Copper.

These alloys constitute the majority of aluminum casting alloys, and thanks to the high fluidity provided by Silicon, the production of complex and thin section parts can be achieved by casting processes.

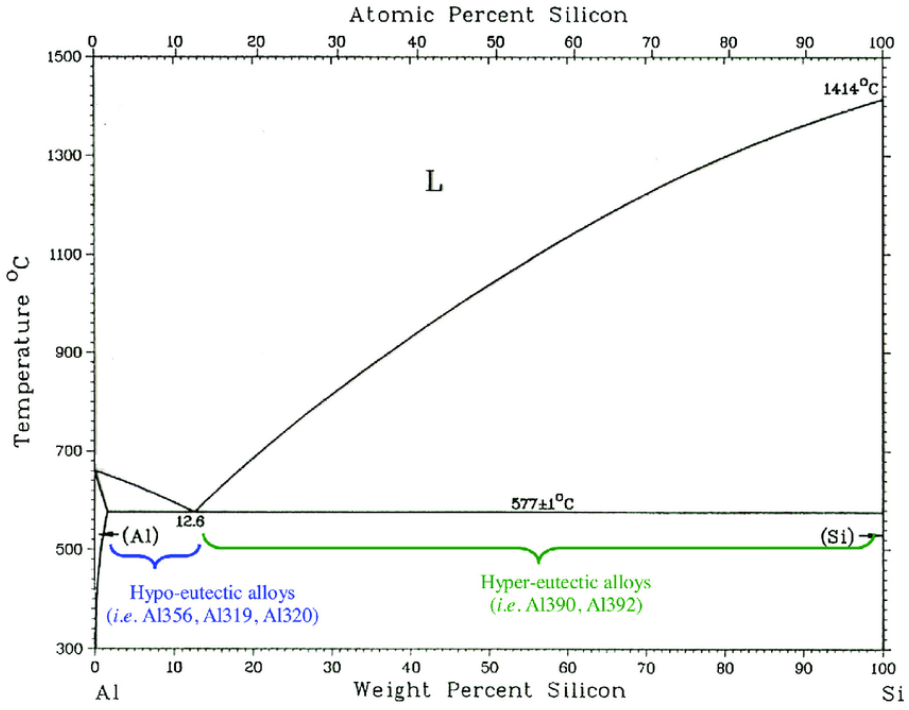

Figure 1.3: Al-Si phase diagram showing hypo-and hyper-eutectic alloys [3].

Aluminum Silicon alloys can be divided into hyper-eutectic, eutectic, and hypo-eutectic categories. Hypo-eutectic alloys are those with less silicon content than their eutectic composition, generally containing 5-10% silicon. They are applied in scenarios that demand high strength and ductility. Eutectic aluminum-silicon alloys, with 10-13% silicon content, primarily comprise the Al-Si eutectic phase. Their well-known attributes include exceptional casting capabilities, excellent flowability, good abrasion resistance, and impressive ductility. Hyper-eutectic Aluminum Silicon alloys possess a silicon content between 15-20% and encompass the primary silicon phase within the Al-Si eutectic phase. These alloys are utilized in applications that necessitate wear resistance, such as motor chains with outstanding wear resistance. [4].

1.1.1.1 A356 Alloy

The 3xx series represents the most commonly employed family of aluminum casting alloys. The A356 alloy, which will be utilized in this project, is a member of this family. Aluminum alloys with silicon as the primary alloying constituent exhibit excellent castability and corrosion resistance.

Table 1.1: Elemental composition of A356 alloy.

Alloy/Element	**Si**	**Fe**	**Cu**	**Mn**	**Mg**	**Zn**	**Ti**	**Other elements**	**Al**
A356	6.5-7.5	0.2	0.2	0.1	0.25-0.45	0.1	0.2	0.2	Balance

Enhancing the structures of Al-Si alloys can be accomplished by incorporating minor quantities of copper, magnesium, or nickel. While silicon imparts favorable casting properties to these structures, magnesium contributes to yield and rupture strengths. The A356 alloy, which belongs to the hypo-eutectic silicon alloys, is extensively utilized in the automotive sector. Optimal physical and mechanical properties are attained when the A356 alloy, containing copper and magnesium in addition to silicon, is used in its heat-treated form. Through heat treatment, magnesium forms an Mg2Si phase with silicon.

1.1.1.2 Heat Treatment Process of Aluminum Alloys

Heat treatment is a process that combines heating and cooling operations, which are timed and applied to metals and alloys in their solid state to achieve desired characteristics. The objectives of heat treatment include enhancing ductility, alleviating internal stresses, refining grain size, increasing strength and hardness, and improving machinability and toughness[5]

Heat treatments for aluminum alloys are commonly denoted by letters such as F, O, H, W, and T. In these abbreviations, F stands for 'as produced,' O signifies 'annealed,' H denotes 'strain hardening applied,' and W represents 'solution heat-treated.' The letter T indicates that the alloy has first undergone solutionizing followed by aging. Numbers adjacent to the T symbol specify different heat treatment variations. The T6 heat treatment encompasses solutionizing, quenching, and artificial aging [6].

Table 1.2: Temper designations and their steps [6].

Temper Designation	**Explanation**
T1	Shaped through cooling process and aged naturally.
T2	Cold worked and naturally aged for cooling.
T3	Solution heat treated, followed by cold working and natural aging.
T4	Solution heat treated and aged naturally.
T5	Hot worked for cooling and then artificially aged.
T6	Solution heat treated, quenched, and artificially aged afterward.
T7	Solution heat treated and subsequently artificially aged.
T8	Solution heat treated, cold worked, and artificially aged later.

T9	Solution heat treated, aged artificially, and cold worked subsequently.
T10	Cooled from high temperature, cold worked, and artificially aged.

The Aluminum Association has defined heat treatment definitions and terms. In the T6 heat treatment process, the solution step targets to enhance the solubility of solid state of alloy elements by increasing the temperature of the alloy the temperature higher than solidus. At this elevated temperature, the element solubility such as magnesium and copper, beneficially impact the alloy's tensile properties, is increased. Following the solution heat treatment, quenching involves rapidly cooling the alloy to prevent the precipitation of dissolved elements within the lattice, yielding an over-saturated lattice structure at room temperature. The aging process step ensures the reinforcement of elements that contribute to increased strength by forming stable precipitates within the structure. Artificial aging takes place in a constant temperature furnace.

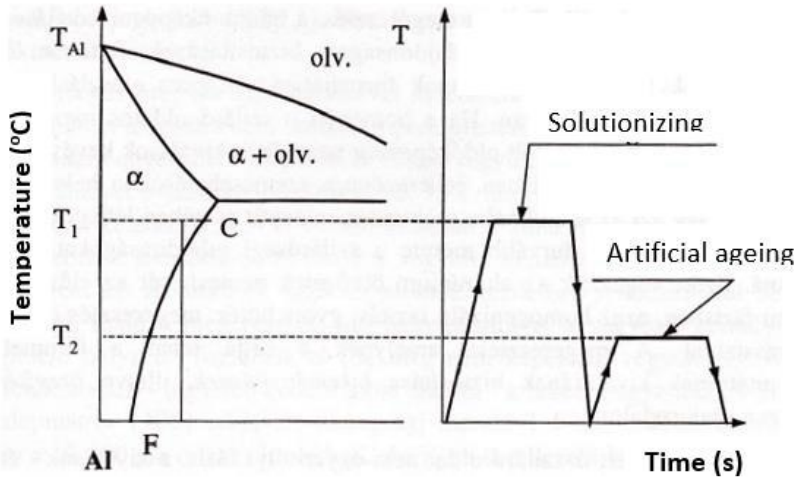

Figure 1.4: Process of the precipitation hardening[7]

The initial stage of precipitation hardening is the solution treatment. This process involves heating above the solvus temperature for several hours, resulting in a homogeneous solid solution. The goal of creating this solution is to fully dissolve the precipitates, enabling the formation of fine precipitates in the subsequent heat treatment stage, thereby achieving optimal strength properties. Consequently, to attain a homogeneous solid solution, it is necessary to heat the alloy to a temperature, T1 (as

shown in Figure 1.4), above its solidus line and maintain this temperature until the homogeneous solid solution evolves. The temperature T1 should be chosen above the solvus line but below the eutectic temperature, with the aim of achieving complete dissolution of the precipitates[8]

Following the solution treatment, the alloy is rapidly cooled to room temperature, a process known as quenching (e.g., with water). The objective of quenching is to inhibit the formation of precipitates at this stage of heat treatment, thereby creating an over-saturated solution of α-solids.

This phenomenon is akin to the formation of martensite through the hardening heat treatment of steel. However, the outcome for aluminum alloys is quite different: while martensite is the hardest microstructural component in steels—owing to the stress effect of trapped carbon atoms within the solid solution—α-solids in aluminum alloys experience a relatively modest increase in strength within the supersaturated α-solid solution.

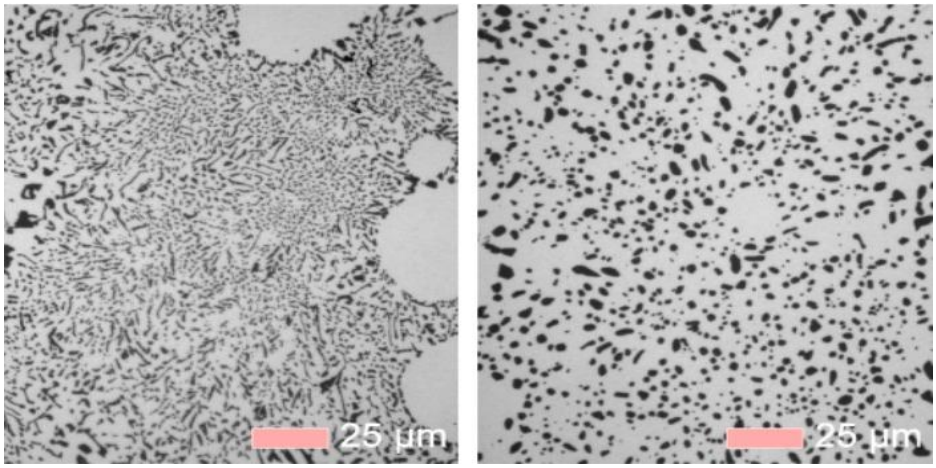

Figure 1.5: Cast eutectic A356 before T6 treatment (left) and eutectic A356 post T6 treatment (right)[8].

The last phase of precipitation hardening for Al alloys is artificial aging, which constitutes the actual precipitation hardening process. The artificial aging temperature is set at a quarter of the solution temperature. The ideal strength properties are achieved when precipitates are finely dispersed within the matrix. If cooling were to occur slowly, precipitates could grow and settle at the grain boundaries, reducing their strength. Therefore, rapid cooling is necessary after artificial aging.

The precipitation process begins with the creation of GP zones. Along with these zones, metastable precipitates may be either consistent with the matrix or semi-consistent. Metastable precipitates can form homogeneously in GP zones or within the matrix when they reach a critical size, or they can heterogeneously distribute along dislocations or other lattice defects. During further aging, semi-stable precipitates expand as atoms diffuse from the supersaturated solid solution to the precipitates. As supersaturation decreases, precipitates keep growing through Ostwald ripening. This phenomenon is driven by a decrease in surface energy, causing larger precipitates to become coarser while smaller ones dissolve. As precipitates enlarge, strain increases until it surpasses the bond strength between interfaces, making the precipitates coherent.

The final shape that emerges in the precipitation sequence is the incoherent equilibrium phase. This phase may not necessarily follow the sequence during the precipitation process but can initiate at an intermediate stage, depending on the material's thermal history (natural aging, artificial aging temperature, heating rate, etc.).

1.1.2 Wrought Aluminum Alloys

Pure or alloyed ingots undergo various mechanical procedures such as extrusion, hot and cold rolling, seamless deep drawing, and drawing. These methods are selected based on the desired cross-section, resulting in products like sheets, plates, foils, rods, and bars. Mechanical properties may be improved by heat treatment, depending on the alloy type. Wrought aluminum alloys are categorized as follows:

1xxx: Containing a minimum of 99 wt. % aluminum, these alloys are primarily utilized in chemical and electrical applications. They demonstrate perfect resistance of corrosion, great workability and high electrical and thermal conductivity but possess reduced tensile values. The main impurities are iron and silicon.

2xxx: With copper as the main alloying element and magnesium frequently present as a secondary element, these alloys have lower corrosion resistance than other aluminum alloys. These materials, under certain scenarios, tend to have less than satisfactory resistance to intergranular corrosion, which leads to their sheet versions usually being coated with high-purity aluminum. These alloys, due to their superior mechanical

characteristics, are commonly employed in the construction of structural elements like fuselages of aircraft, components of automobiles, and suspensions of trucks.

3xxx: Manganese, the primary alloying element, offers a 20% strength increase in comparison to 1xxx alloys. These alloys are commonly employed for applications that require moderate strength and good workability.

4xxx: Silicon is the primary alloying element, providing a reduced melting range without causing brittleness when present in sufficient quantities (up to 12 wt. %). Owing to their lower melting points, these alloys are utilized in welding applications for joining aluminum alloys. They also exhibit a low coefficient of thermal expansion and high wear resistance.

5xxx: The primary element used for alloying is magnesium, although manganese is occasionally employed to achieve a range of moderate to high strength attributes. Magnesium's efficacy in enhancing mechanical properties outperforms that of manganese significantly. These alloys not only exhibit excellent resistance to welding but also demonstrate good resistance to corrosion in marine settings.

6xxx: The primary alloying elements are silicon and magnesium, offering lower mechanical properties compared to 2xxx and 7xxx alloys. They provide excellent formability, weldability, machinability, and corrosion resistance.

7xxx: Zinc, the major alloying element, ranges from 1 to 8 wt. % and is sometimes combined with magnesium. These alloys have moderate to high strength and are employed in highly stressed components like airframe structures. However, their resistance to stress corrosion decreases as their strength increases. Therefore, most of these alloys are used in overaged conditions.

8xxx: This alloy group covers a wide range of chemical compositions, such as Al-Fe-Ce (e.g., 8019) and Al-Fe-V-Si (e.g., 8009), leading to various microstructures and applications. Lithium-containing aluminum alloys (e.g., 8090) also belong to the 8xxx group and offer higher specific strength and stiffness, making them suitable for aerospace applications.

Chemical compositions determine the classification of wrought alloys, which, in turn, determine microstructure differences, such as the type of second phases. Second-phase formation is related to heat treatment. Certain alloy types are classified as heat-treatable if they form precipitations in response to heat treatment, while others are considered non-heat treatable. Among aluminum wrought alloys, 2xxx, 6xxx, 7xxx, and some 8xxx alloys are heat treatable, while others obtain enhanced mechanical properties via strain hardening.

Table 1.3: Summary table of Aluminum Alloy Designation System [3].

Alloy Code	**Dominant Alloying Element**
1xx.x	99.000% minimum Aluminum
2xx.x	Copper
3xx.x	Silicon Plus Copper and/or Magnesium
4xx.x	Silicon
5xx.x	Magnesium
6xx.x	Silicon and Magnesium
7xx.x	Zinc
8xx.x	Tin
9xx.x	Other Elements

1.2 Effect of Alloying Elements on the Properties of Al-Si-Mg Alloys

Due to their remarkable castability, corrosion resistance, and high specific strengths, Al-Si-Mg alloys are extensively used in the automotive and aerospace industries. These alloys, with a silicon density of 2.3 g/cm3, are lighter than other alternatives. In automotive airframe structures, they often replace heavier alloys, resulting in lower fuel consumption and decreased CO2 emissions. The addition of silicon to aluminum enhances fluidity, reducing shrinkage and decreasing the likelihood of hot cracking defects. Through heat treatment, these alloys can attain improved mechanical properties.

Magnesium is incorporated at concentrations ranging from 0.3 to 0.7 wt. % to create intermetallic compounds with silicon. The Mg2Si precipitates in aluminum matrix contribute to increased yield strength. In addition to Mg2Si compounds, detrimental iron-based impurities such as α (Fe2SiAl8), β (FeSiAl5), and π (FeMg3Si6Al8) may also develop. Nonetheless, having an excessive amount of magnesium in the alloy is not ideal, as it forms brittle precipitates with iron. Consequently, iron-containing Al-Si-Mg alloys have limitations regarding magnesium concentration.

1.2.1 Effect of Silicon

Silicon, being one of the most economical materials across the globe, is an appealing choice for incorporation in alloys. Along with its financial benefits, silicon boosts castability, specific strength, and resistance to corrosion, while simultaneously lowering the coefficient of thermal expansion. Due to the potent atomic bonding forces of silicon, the wear resistance of the alloy is increased. [9]

An invariant eutectic reaction occurs between aluminum and silicon at approximately 577 °C, as illustrated in Figure 1.5. Primary aluminum dendrites form initially during solidification, followed by eutectic transformation. Microstructural examination shows the presence of primary aluminum dendrites and eutectic silicon particles. For a low iron content Al-Si alloy, Figure 1.6 reveals large flake-like eutectic silicon particles in the as-cast state [10]. Such a large flake structure adversely impacts

mechanical properties, resulting in abrupt fractures. To achieve finely dispersed eutectic phases, modification with elements like Na, Sr, and Be is carried out.

Figure 1.6: Large flake of eutectic Si phase

1.2.2 Effect of Iron

Iron can be derived from various sources, with a notable portion stemming from primary aluminum production [11], introducing 0.03 - 0.15 wt.% of Fe during this process. Additional sources encompass tools and furnace equipment employed in later casting processes. The iron content in aluminum is influenced by the duration and temperature maintained during casting, due to the interaction between the molten aluminum and the ferrous tools. Each additional cycle of melting is disadvantageous due to contact with unprotected ferrous equipment and tools. Iron may also be introduced to aluminum by alloying elements that are not pure. Despite its high solubility in liquid aluminum, the solubility of iron in solid state is limited, which leads to the creation of intermetallic compounds with aluminum and other alloying elements. Although these intermetallic precipitates can pose problems in the process of sand casting, they are crucial in high-pressure die casting procedures to avert die soldering. However, for sand casting, the control over the weight percentage, form, size, and chemical makeup of the intermetallic phases is essential, adjustments for which can be made considering the chemical compositions of the raw materials. Reducing the iron content in the aluminum melt results in higher processing costs and improved mechanical properties. Dominant phases in the presence of silicon include α

(Fe2SiAl8) and β (FeSiAl5). When Mn is present, Al15(Fe,Mn)3Si2 can form, confusingly known as the α phase. These can be distinguished using an optical microscope and exhibit different shapes and colors. Both α phases display a script-like morphology during microstructural examination. However, the Mn-included phase appears more block-like and compact, as reported by [11]. The β phase shows a platelet morphology in three dimensions but looks needle-like in two dimensions. The π (FeMg3Si6Al8) phase can form when Mg is present alongside Si. This phase has a script-like morphology and is generally, though not always, closely associated with the β phase [11]. Figure 1.7 demonstrates the morphological differences among iron-rich intermetallic phases, which is crucial since mechanical properties and alloy castability utilities are influenced [11].

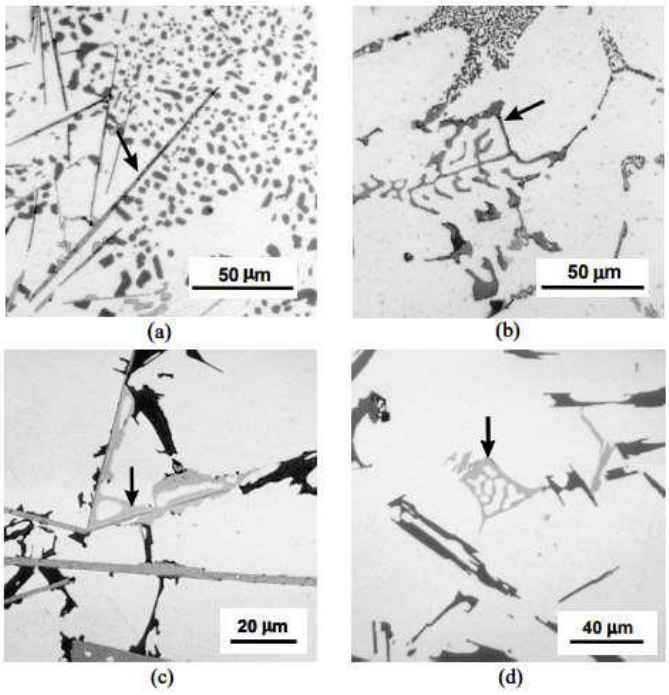

Figure 1.7: Various Fe-rich precipitates shown in microstructures on a) β platelets b) script-like α c) π phase emerging from β d) script-like π phase[11].

In addition to the melt's chemical composition, the cooling rate serves as a crucial factor in the formation of intermetallic phases. Lower cooling rates and a higher number of iron atoms in the melt encourage the growth of larger particles by extending the intermetallic phases' growth time. As concentrations of Fe and Mn increase, larger β platelets and α script-like phases emerge in the microstructure, owing to elevated nucleation temperatures that allow for more uninhibited growth. Taylor contends that ductility is reduced due to micro-crack initiations caused by iron intermetallics and

fractures within them, while porosity increases with higher iron content, forming crack initiation sites. The β phase is considered more harmful than the α phase, which is why research on neutralization with other chemical elements such as Cr, Co, Ni, Be, Mn and others is conducted to decrease the amount of the β phase.

1.2.3 Effect of Magnesium

The yield strength of Al-Si alloys is enhanced by magnesium through heat treatment, with solutionizing and aging processes resulting in the formation of Mg2Si particles. Magnesium content directly related with the yield strength. However, an excess of magnesium can cause the formation of detrimental iron-rich intermetallics, such as the π phase (FeMg3Si5Al9), which becomes more significant when the eutectic modification element, Sr, is employed. Caceres et al. observe that while yield strength increases with rising Mg content, there is a slight decline in ductility. They also note that the influence of Mg on ductility is more evident in modified alloys due to the creation of larger π phases.[12].

1.2.4 Solidification Sequence of Al-Si-Mg Alloys

In the initial step depicted in Table 1.4, nucleation and growth of the primary aluminum dendritic phase occur. During the second stage, the primary Al-Si binary eutectic reaction (reaction 2) takes place. As the liquid fraction diminishes, Fe significantly partitions to the liquid phase, enriching it until the ternary eutectic is attained, solidifying Al, Si, and β-AlFeSi. Subsequently, a quasi-peritectic reaction partially transforms the β-phase into the π-phase. The extent of this peritectic transformation likely hinges on the cooling rate during solidification. The following stages involve the ternary eutectic generating Al, Si, and Mg2Si (reaction 4), and finally a quaternary reaction producing π-AlFeMgSi along with the previous three phases. Moreover, α-Al(Fe, Mn)Si has been reported in the final stages of higher Mg alloys.[13].

Table 1.4: Solidification reactions of Al-Si-Mg Alloys [13]

Reaction	Suggested start Temperature (°C)
Liq. Al dendrites	611-615
Liq. Al + Si	577
Liq. Al + Si + Al5FeSi	575
Liq. + Al5FeSi Al+ Si + AlgFeMg3Si6	567
Liq. Al + Si + Mg2Si	555
Liq. Al + Si + Mg2Si + AlgFeMg3Si6	550-554

1.2.5 Grain Refinement Mechanisms on Al-Si Alloys

Considered one of the most vital and prevalent melt treatment techniques for Al-Si casting alloys, grain refinement plays a crucial role. Enhancing the grain structure of aluminum alloys leads to reduced ingot cracking, increased microstructure uniformity, and superior mechanical properties. The mechanism of grain refinement aids in minimizing the size of α-Al dendrite grains in the casting. Numerous advantages are offered by a fine equiaxed grain structure, including uniform distribution of secondary phases, diminished microshrinkage and microporosity, improved feeding characteristics, heightened toughness, increased yield strength, and superior machinability.[14].

Various grain formation mechanisms occur during casting solidification. Generally, two factors contribute to initiating grain formation. Firstly, suitable compounds must be present in sufficient amounts to serve as heterogeneous nucleation sites. Secondly, enough undercooling is needed for the formation and growth of nucleation particles to proceed. The undercooling can be achieved either through rapid cooling or solute partitioning.

Decrement on grain refining has a dominant effect on yield strength. This phenomenon was explained well by Hall-Petch equation[15]. The underlying principles of grain refinement are based on nucleation and growth processes.

1.2.5.1 Nucleation Theory

In the process of a liquid alloy solidifying, there is a particular temperature at which the formation and expansion of nucleation particles occur. These particles are comprised of solid atoms that are generated during solidification. The term "nucleus count" is used to refer to the quantity of nuclei. The production of grains is a result of the nucleus's growth, and there is a direct connection between the quantity of grains and nuclei. The size of the nucleus when it initially forms is a vital factor for the growth mechanism to take place. There are two distinct types of nucleation mechanisms: homogeneous and heterogeneous nucleation.

1.2.5.1.1 Homogeneous Nucleation

In the absence of any defects or alternative nucleation sites, homogeneous nucleation takes place. The formation of nuclei starts at a temperature, T, lower than the equilibrium melting temperature, Tm. This event is referred to as undercooling, which serves as a driving force for nucleation. Nucleation requires a specific level of undercooling. The degree of undercooling for homogeneous nucleation is extremely high, typically not attainable in the majority of engineering applications. The notion of undercooling is depicted diagrammatically in Figure 1.8.

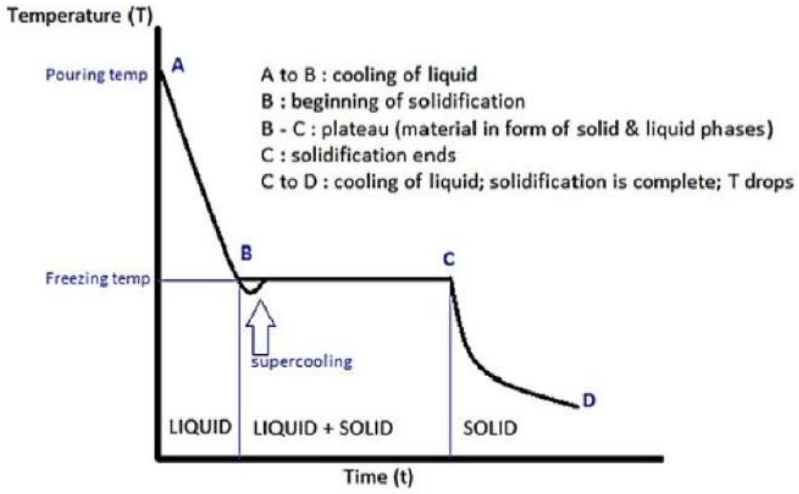

Figure 1.8: Diagram for pure petals on undercooling situation.[16]

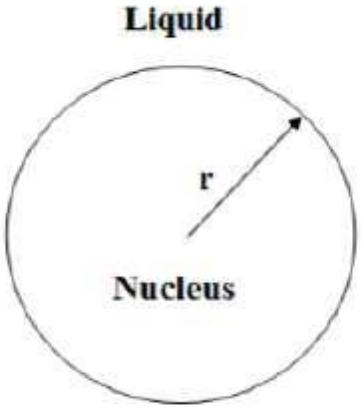

Figure 1.9: Schematic visualization of nucleus[17].

The formation of nuclei requires a shift in free energy. A specific extent of free energy change must exist for the nucleus formation to take place. The energy necessary for the phase transition is called ΔGv, representing the net free energy needed for transforming from the liquid to the solid phase, and ɣsl, the interfacial tension between the solid and liquid interface. [17].

$$\Delta Gv = \Delta H - T\Delta S \quad (1)$$

Where,

ΔH: The enthalpy change = Latent heat of fusion per unit volume, Lv

ΔS: The entropy change = $\frac{Lv}{Tm}$

Tm: Melting point of liquid

The following equation can be derived from Equation (1):

$$\Delta Gv = Lv - T\frac{Lv}{Tm} \quad (2)$$

The transformation from liquid to solid can spontaneously occur when the value of equation (2) is negative. Nucleation is evident when the temperature, T, falls below the melting temperature, Tm. Additionally, taking into account the total volume of the sphere, the net free energy needed for the entire sphere can be calculated as:

$$\Delta G = \Delta T \frac{Lv}{Tm} \frac{4}{3} \pi r^3 \quad (3)$$

Sphere radius indicated by r was shown in Figure 1.9.

$$\Delta T = \frac{Tm - T}{Tm} \quad (4)$$

Expressing the net free energy per volume, considering a specific undercooling, can be done using equation (4) in the following manner:

$$\Delta Gv = \Delta T \frac{Lv}{Tm} \quad (5)$$

The energy necessary for nucleus formation is represented by equation (5). However, there is an additional term, surface energy (ΔGs), which is shown in equation (6). This term has a positive value and represents the energy required to create new surfaces during nucleus formation.

$$\Delta Gs = 4\pi r^2 * \gamma sl \quad (6)$$

Accounting for both the surface energy term and the net free energy term per volume, equation (7) can represent the total energy required to form a spherical particle.

$$\Delta Gr = \Delta Gv * \frac{4}{3} \pi r^3 + 4\pi r^2 * \gamma sl \quad (7)$$

In nucleation theory, a key parameter is the critical nucleus radius, often referred to as r*. At the point of necessary undercooling, certain atoms begin to solidify near Tm. The commencement of nucleus formation and growth requires that the net change in free energy for a sphere be negative. As depicted in Figure 1.10, the total free energy components include the total free energy per volume and the surface energy. In the early stages of nucleus formation, the overall free energy is positive due to the new surface creation outweighing the free energy per volume term. To put it more simply, the equation is dominated by the term related to surface energy until r < r*, with r* signifying the critical radius for sphere particle formation. As a result, nucleus formation is thermodynamically improbable because the reaction is nonspontaneous, causing the solidifying atoms to dissolve back into the melt. However, once r exceeds r*, the net change in free energy becomes negative, which is thermodynamically stable

and facilitates the creation of new solid atoms. At this point, the free energy per volume term takes control over the equation for total free energy.

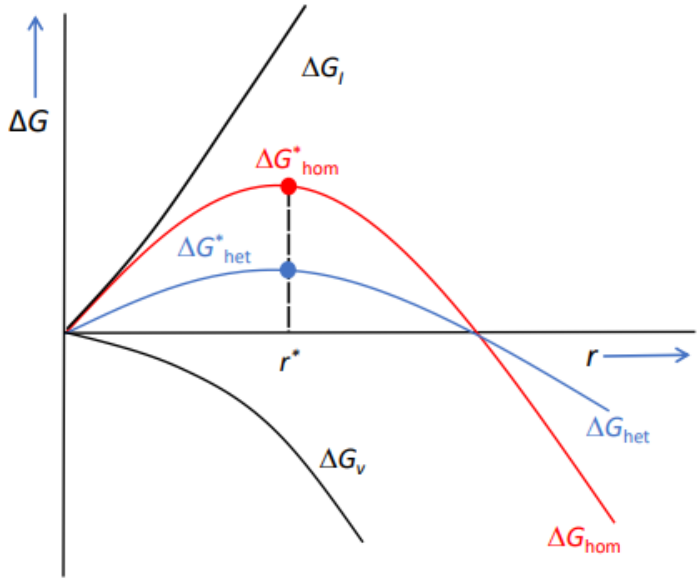

Figure 1.10: The free energy change (ΔG) in relation to cluster size (r) illustrates the formation of nuclei (r*) in both homogeneous and heterogeneous nucleation processes by overcoming the energy barriers (ΔG_{hom}, ΔG_{het}). [17]

Determining the critical radius can be achieved by identifying the slope when the energy corresponds to the maximum energy illustrated in Figure 1.10.

$$r^* = \frac{2\gamma sl}{\Delta Gv} \tag{8}$$

By substituting equations (5) to (7) into equation (8), expression can be obtained in equation (9).

$$r^* = \frac{2\gamma sl * Tm}{Lv} * \frac{1}{\Delta T} \tag{9}$$

Equation (9) indicates that an increase in undercooling leads to a decrease in critical radius and ΔG*, or a reduction in interfacial surface tension produces the same outcome. By substituting equation (9) into equation (7), we can derive the expression found in equation (10).

$$\Delta G^* homogeneous = \frac{16\pi\gamma sl^3}{3\Delta Gv^2} \tag{10}$$

1.2.5.1.2 Heterogenous Nucleation

In heterogeneous nucleation, impurities, mold walls, oxides, grain refiners, or other nucleation sites act as sources. Heterogeneous nucleation is more common in solidification processes because the undercooling required for homogeneous nucleation is typically quite high, making it a rare event. The mechanism behind heterogeneous nucleation is the reduction of interfacial surface energy, resulting in decreased free energy, as shown in equation (7). The formation of nuclei in heterogeneous nucleation is distinct from that in homogeneous nucleation. In heterogeneous nucleation, fewer atoms are needed for nucleus formation, and as the interfacial surface energy decreases, the critical radius size also decreases, as illustrated in equation (9). The interfacial energy between the solid and mold can be expressed as;[17]

$$\gamma ml = \gamma sm + \gamma sl * \cos(\theta) \quad (11)$$

Where,

γ_{ml} : Interfacial surface energy between mold and liquid

γ_{sm} : Interfacial surface energy between solid and mold

γ_{sl} : Interfacial surface energy between solid and liquid

θ: Wetting Angle

$$\Delta G*heteregeneous = \Delta G*homogeneous * f(\theta) \quad (12)$$

1.2.5.2 Grain Refinement by Chemical Inoculation

Grain refinement is achieved using suitable inoculants, with the most common compounds being Al-Ti-B-based alloys, typically Al-5 wt.% Ti-1 wt.% B. These are added to molten Al-Si alloys in concentrations ranging from 100 to 1000 ppm, particularly in foundries. Titanium is the most commonly used grain refiner element

for Al casting alloys, although other inoculants such as V, Nb, Ta, Zr, Mo, Ce and W can also be employed [14]. According to this theory, dispersed nuclei act as reactive nucleation sites during solidification. However, the inoculation mechanism is inefficient, as only less than 1% of the TiB_2 particles nucleate as solid grains. This inefficient solidification leads to recalescence, which inhibits other nucleation systems.

A better comprehension of the Al-Ti-B system's phases and their influence on grain refinement can be achieved by analyzing the individual additions of Al-Ti and Al-B master alloys. Cibula revealed that introducing minor quantities of titanium into the melt could lead to a substantial decrease in grain size, with effects noticeable at levels as low as 1000 ppm. A peritectic reaction, presented in equation (13), takes place within the aluminum-titanium system at 665°C, as shown in Figure 1.11.[18].

$$\text{Liquid} + \text{Al3Ti} \rightarrow \alpha\text{-Al (solid solution)} \quad (13)$$

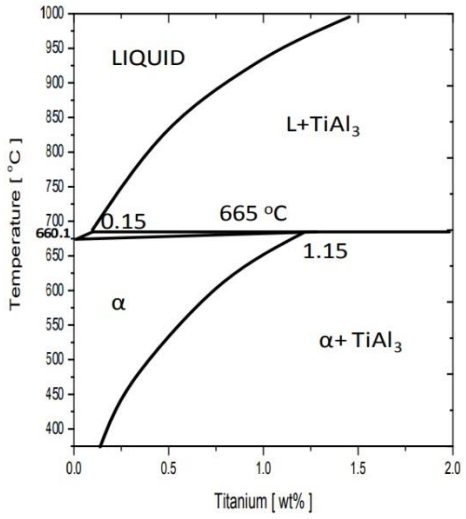

Figure 1.11: Al-Ti Phase Diagram.

Al3Ti, which contains more than ~1500 ppm titanium, exhibits a tetragonal structure [19], [20]. Upon introducing an Al-Ti master alloy into the aluminum melt, α-Al dissolves with a minuscule quantity of titanium, resulting in the suspension of Al3Ti particles in the melt. These Al3Ti particles have the potential to act as heterogeneous nucleation sites. While Al-B master alloys have been proposed to refine Al-Si casting

alloys through AlB2, as depicted in Figure 1.12, the molten metal undergoes eutectic nucleation at 660°C and 220 ppm B. [21]:

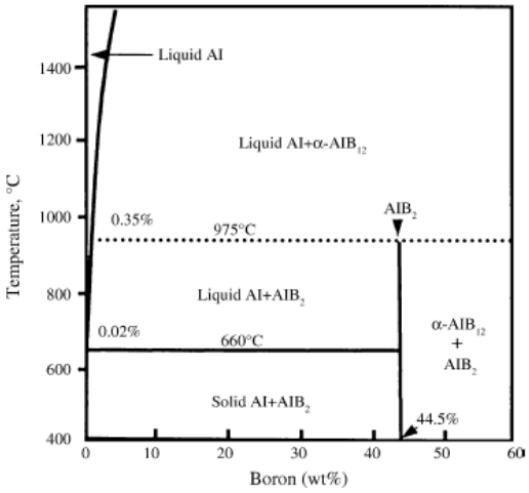

Figure 1.12: Al-rich side of Al-B Phase Diagram [22].

$$\text{Liquid} \rightarrow \text{AlB2} + \alpha\text{-Al (solid solution)} \qquad (14)$$

1.2.5.2.1 The Nucleant Paradigm

The development of the nucleant paradigm is rooted in two concepts: the theory of nucleant-particle and the theory of phase diagram. Both theories pertain to the two types of particles in the Al-Ti-B master alloy. The first theory proposes that nucleation is initiated on the existing borides (TiB_2, AlB_2, and (Ti, Al) B_2) in the master alloy, whereas the second theory attributes grain refining to nucleation on the hypo-peritectic phase, Al_3Ti. The hypothesis that nucleation happens on boride or carbide particles was suggested by Cibula after an examination of nucleant-particle theories [18]. With only slight changes in the lattice parameters, TiB_2 and AlB_2 phases have a hexagonal lattice, a = 0.30311 nm and c = 0.32 nm, and a = 0.00029 nm and c = 0.33 nm [20]. Boride particles are located at the grain center, where α-Al nucleates. Mohanty et al. suggested that boride phases precipitate on grain boundaries and that grain refinement is not achieved without dissolved titanium [23]. It was observed that borides are not as efficient as Al_3Ti for nucleating dendrites. As a result, phase diagram studies were enhanced to show how Al_3Ti particles can actively nucleate in the hypo-peritectic composition[24].

Phase diagram theories posit that grain refinement is due to the peritectic reaction on primary particles (Al_3Ti). Marcantonio and Mondolfo suggested a triple eutectic reaction, Liquid → (Al, Ti) B_2 + $TiAl_3$ + solid, at approximately 500 ppm Ti, 100 ppm B, and 659°C, but this hasn't been directly confirmed by data of experiment [25]. The main issue with phase diagram theories is that Al_3Ti doesn't exist as nucleation sites at hypo-peritectic concentrations for anything but very short holding times, so these theories unable to expose grain size reduction mechanisms at hypo-peritectic Ti amounts. Moreover, these theories couldn't establish why adding B to the Al-Ti system significantly enhances the grain refinement mechanism.

Backerud et al. studied the peritectic hulk theory, which suggests that borides form a shell around Al_3Ti, reducing its dissolution rate since diffusion must pass through the boride shell [26]. Jones' hyper nucleation study shows that small amounts of titanium and boron can refine grains [27]. The duplex nucleation theory is the most recent concept in this paradigm. Mohanty et al. proposed that a layer of Al_3Ti forms at the boride-Al-Si melt interface, initiating α-Al nucleation [23].

1.2.5.2.2 The Solute Paradigm Theory

Johnson suggested that the growth restriction factor (GRF) has a substantial impact on the grain refinement mechanism [26]. This theory states that the solute's impact on dendrite growth and the constitutional undercooling zone ahead of the interface are as important as nucleation. As demonstrated in Figure 1.13, Maxwell and Hellewell provided evidence that the grain count per unit volume (N_vG) rises with the number of particles per unit volume (N_vP) only until it reaches a pivotal value, after which saturation is attained. Beyond this critical N_vP value, not all particles serve as potential nucleation sites.[28]. Only about 1% of the total particles partake in the heterogeneous nucleation reaction, owing to the broad size distribution and clusters of Al_3Ti and TiB_2 [29].

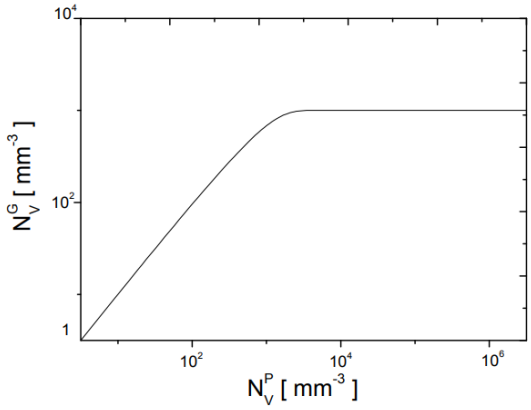

Figure 1.13: Graph of number of grains and number of particles [28].

Inversely connected to the constitutional undercooling parameter, $_{m}Co(k-1)$, is the dendrite growth rate, where 'm' indicates the liquidus slope, 'Co' corresponds to the solute concentration in the melt, and 'k' refers to the equilibrium partitioning coefficient. As undercooling increases and growth rate decreases, there is a rise in the number of nucleation sites. An asymptotic reduction in the grain size of a solidified alloy in relation to the GRF is suggested by Schumacher and Greer [30].

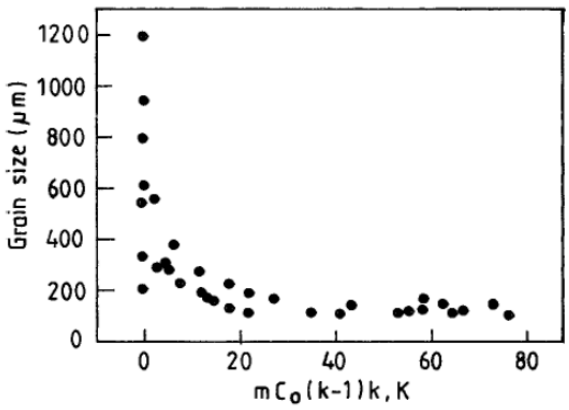

Figure 1.14: Graph of relationship between grain size and GRF [30].

The GRF is calculated by summing up the constitutional undercooling parameters of all individual elements, $_{m}Co(k0-1)$. TiB_2 particles exhibit effective nucleation performance. This guarantees an adequate degree of undercooling for TiB_2 to be a suitable nucleant particle choice for aluminum.

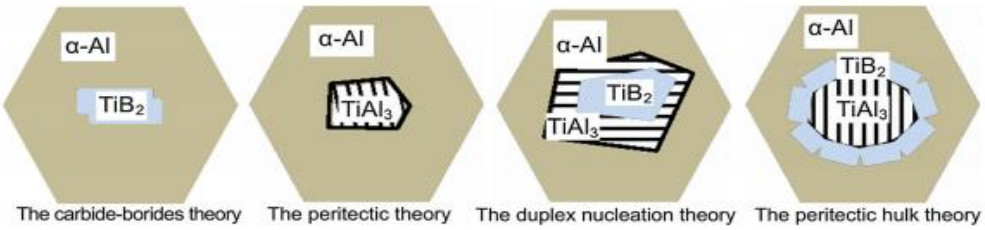

Figure 1.15: Representation of nucleation theories [31].

Table 1.5: Positive and negative aspects of each grain refinement theory[31].

Theory	Positive viewpoints	Negative viewpoints
The carbide-borides theory	The effectiveness of grain refinement in the Al-Ti-B master alloy is superior to that of the Al-Ti alloy, with TiB_2 being present within the Al grain	The Al-TiB_2 master alloy does not exhibit grain refinement in high-purity Al, while the Al-Ti alloy does show grain refinement effectiveness in high-purity Al. In the absence of solute Ti, carbides (or borides) do not contribute to grain refinement
The peritectic theory	The explanation of refinement behaviors in Al-Ti series alloys is provided, and this theory makes sense in the context of Al alloy melts containing $TiAl_3$. $TiAl_3$ is found at the center of Al grains	The theory fails to clarify the enhancing impact of the B element on grain refinement, as the available free Ti is significantly lower than the required Ti level for the peritectic reaction. Furthermore, the $TiAl_3$ phase is

		thermodynamically unstable for the peritectic reaction to occur.
The peritectic hulk theory	In the presence of B addition, the $TiAl_3$ phase remains stable even at lower concentrations. The grain refinement behavior of Al–Ti–B (with a Ti/B ratio of 2.22) can be explained using the duplex nucleation theory.	Boron does not influence the Al–Ti phase diagram or the stability of $TiAl_3$. While the grain refinement effectiveness of Al–Ti–B refiners diminishes over extended holding periods, this effect vanishes after stirring the mixture.
The duplex nucleation theory (the hyper nucleation theory)	The presence of a Ti-rich layer on the TiB_2 surface exists.	It is challenging to theoretically identify the thin phase between TiB_2 and amorphous Al, as pure Al, a mixture of Al and Al_3Ti, or an intermediate Al-Ti structure could all potentially nucleate on the surface of a TiB_2 particle.
The solute theory	The presence of solute elements impacts grain growth restriction. Higher solute concentrations lead to an increase in nucleation.	The influence of the solute element's restrictive effect on nucleation behavior and final grain size is insignificant.

1.2.5.3 Grain Refinement by Rapid Cooling

The microstructure of castings is significantly influenced by cooling rate. Smaller grain sizes and reduced solidification time are achieved with higher cooling rates, leading to an increase in grain density. Improved nucleation energy and rate are also observed as the cooling rate increases, resulting in a decrease in nucleation energy, which underlies the rapid solidification process for grain refinement.

Rapid solidification can be used to create alloys that tend to segregate or coarsen, as initially explored by Duwez in his research [32]. He discovered that non-equilibrium crystals could be formed when the liquid metal was cooled at an adequate rate [33]. Since then, rapid solidification has been employed to create various fine-grained metal castings. Large-scale castings, often made in sand molds, typically have cooling rates less than 0.1 K/s, whereas metal mold castings generally exhibit cooling rates between 1 and 1000 K/s.

To attain a high cooling rate, it is necessary for at least one dimension of the material being processed to be small enough to achieve a suitable thermal modulus in the cast part. Several techniques have been developed to accomplish rapid solidification rates for the production of metallic glass (MG) or fine-grained materials [34]. Melt spinning, copper mold casting, liquid forging, and high-pressure die casting are among the methods extensively researched in recent studies for the production of metallic glass.

1.2.6 Poisoning and Fading Effect of Ti-B a Cast Aluminum Alloys

During the grain refinement of cast alloys, holding the molten metal for an extended period after adding the refiner can result in a coarse grain structure instead of the desired fine-grained structure. This is referred to as the fading phenomenon. Fading is caused by the dissolution or precipitation/floatation of nucleating particles during long holding times of molten metal in crucibles. Furthermore, some alloys containing elements such as Cr, Zr, and Si can negatively impact the Al-Ti-B master alloy's grain refinement effectiveness, a phenomenon often called the poisoning effect [35]–[38]. It is commonly thought that poisoning elements interact with Al-Ti-B master alloy's grain-refining components ($TiAl_3$ and TiB_2), making them less effective or ineffective over time.

In the grain refinement process of Al-Si alloys, Si is anticipated to decrease grain size through the constitutional undercooling mechanism or growth restriction effects when present in low concentrations in the Al melt. However, grain coarsening occurs when the Si concentration exceeds 3% by weight.

1.2.6.1 Poisoning Effect of Al-Si Casting Alloys

The surface interface of TiB_2 particles offers a more energetically favorable location for Si atoms compared to the matrix grain boundaries. The solubility of Ti in solidified Al decreases in the presence of Si. Titanium silicide forms a coating on the $TiAl_3$ surface, reducing the efficacy of the nuclei found in the Al-Ti master alloy during the grain refinement stage of Al-Si alloys, as observed by Sigworth and Guzowaski [21]. However, they later discovered that the AlB_2 phase serves as a nucleation catalyst on the lattice, with the presence of Si enhancing its nucleation potential [29], [39].

According to the literature, Fan et al. examined a layer of $TiAl_3$-like structure on the Ti-containing TiB2 substrate, which was later identified as a single-layer of $TiAl_3$, a two-dimensional material tightly adhering to the (0001) TiB_2 surface [40]. The intermediate $TiAl_3$ effectively lowers the lattice misfit between TiB_2 and α-Al (from 4.22% to 0.09%), thus increasing the nucleation potential on TiB_2 particles [41]–[43]. The origin of the Si poisoning effect on the Al-5Ti-B grain refiner remains elusive despite various techniques being investigated.

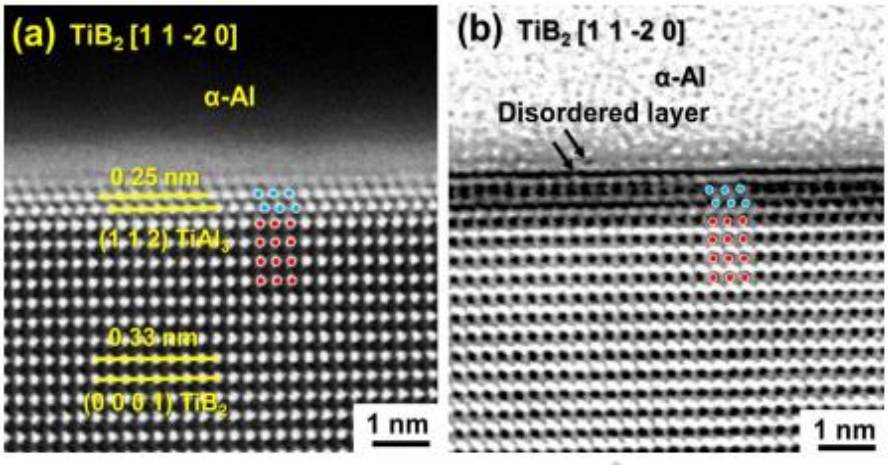

Figure 1.16: HAADF-STEM image of $TiAl_3$ layer on TiB_2 (b) ABF image [44].

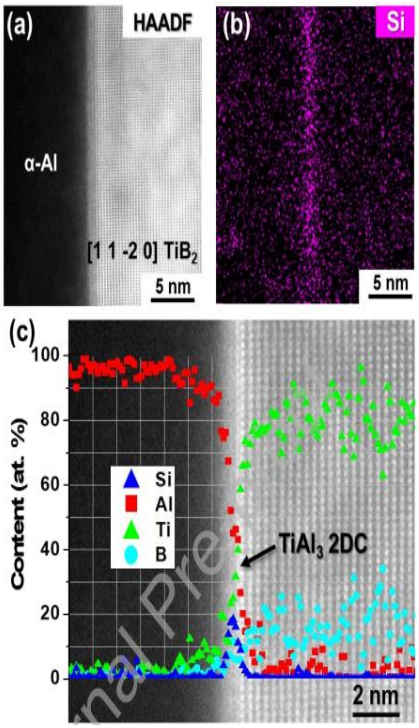

Figure 1.17: (a) HAADF-STEM image across the TiB_2/α-Al interface in the Al-9 Si-4Ti-1B ingot; (b) EDS scanning of Si; (c) composition graph on the interface [44].

1.2.6.2 Fading Effect of Casting Alloys

Different methods have been implemented to incorporate grain refiner particles into the molten material. The most common technique employs commercial Al-Ti-B master alloys, which are added to the molten metal in rod or bar form. The time period for which the master alloy interacts with the melt is of critical importance for achieving optimal results. A reaction fails to occur if the interaction time is too short, whereas an overly extended interaction period prevents grain size refinement. This decline in performance due to an overly long interaction period is termed as fading. Limmaneevichitr et. al. suggest that fading transpires due to the higher density of TiB2 and Al3Ti compared to molten aluminum [35]. This leads to the particles settling at the bottom of the crucible or furnace due to an extended interaction period between Ti-bearing phases and molten Al [45]. The settling is also linked to the molecular weight disparity between melt Al (2.7 g/cm3) and TiB_2 (4.52 g/cm3) and $TiAl_3$ (3.36 g/cm3) nucleants. Wang et al. noted that both Ti and B compositions tend to decrease from the crucible's bottom to the top as a function of contact time. Grain size is also directly proportional to the compositional change [46].

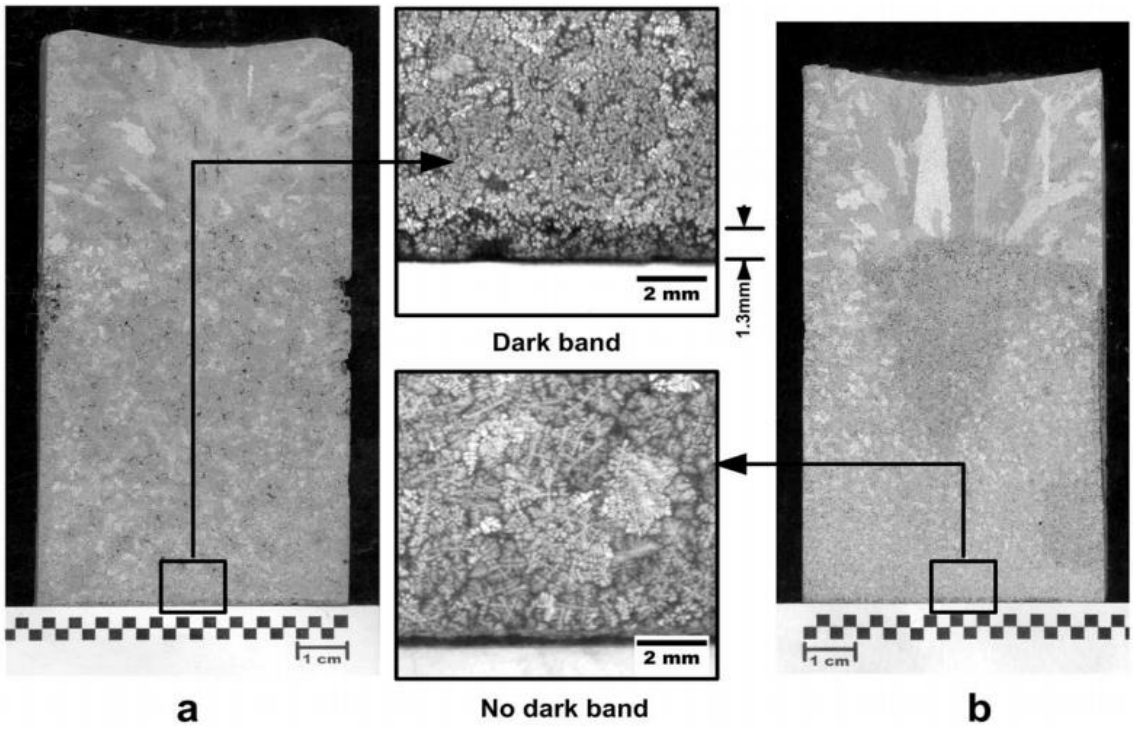

Figure 1.18: A 120-minute contact time of 4 wt.% Ti-B master alloy in A356 Al alloy: (a) without stirring, and (b) stirred immediately before the start of solidification [46].

1.2.7 Eutectic Si Modification

The process of modifying eutectic Silicon in aluminum-silicon alloys was initiated in the 1920s, with Pacz being credited with the discovery of the first modification phenomenon. The evolution of technology, particularly in the field of electron microscopy, has enabled the exploration of modification mechanisms at a microscopic level [47].

In Al-Si casting alloys, reducing the size of the eutectic phase by modification mechanisms, similar to grain refinement in aluminum, is a standard process for foundry applications that meet industrial needs. Modification occurs naturally in rapid solidification, but in slow solidification, modifying elements are necessary. Group I and IIA rare earth elements in the periodic table, such as europium, lanthanum, cerium, and praseodymium, are used for modification. Only sodium and strontium exhibit strong modifying effects at low concentrations. Both elements transform needle-like eutectic silicon into fibrous silicon, resulting in improved mechanical properties of the alloy by reducing stress points caused by needle-like Si. Rapid cooling can achieve this modified structure, a process commonly known as cooling modification. Melt heat

treatment helps provide a refined solidification microstructure in Al-Si alloys [48]. As silicon is a nonmetal that directs covalent bonding in Al-Si alloys, the silicon phase tends to grow anisotropically, forming directional crystals. The silicon phase requires more cooling than the isotropic aluminum phase for nucleation. Figure 1.19 indicates the modification level of eutectic Si phase on Al matrix.

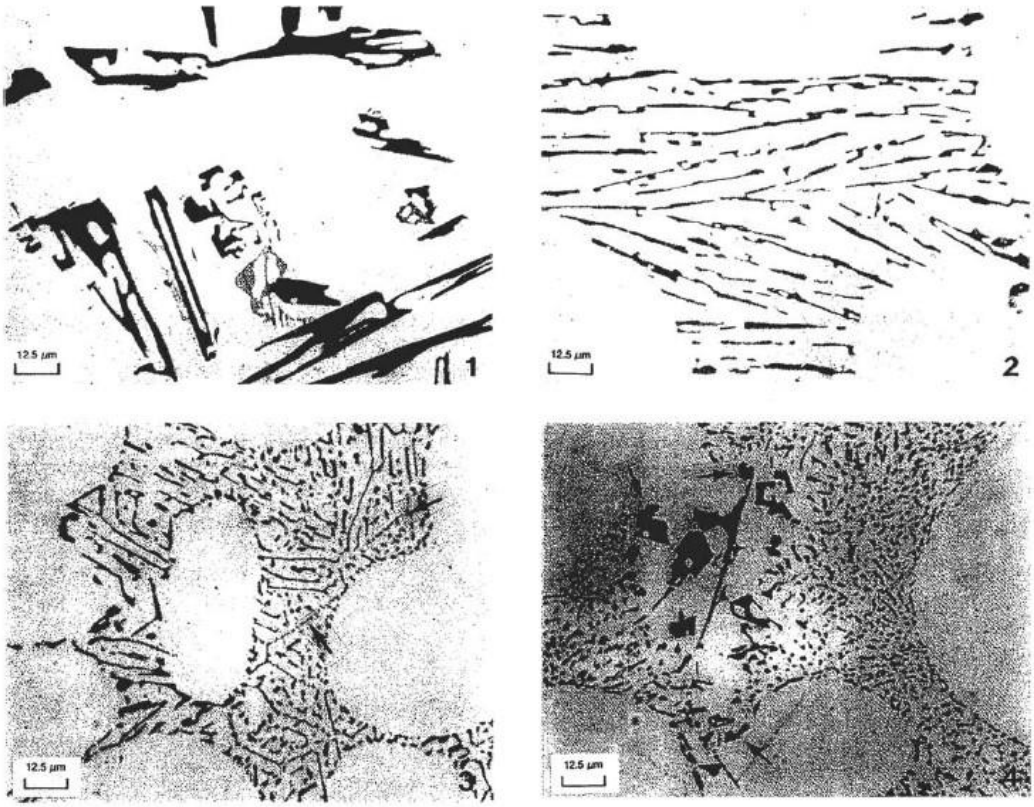

Figure 1.19: Eutectic structure morphologies. (a) Acicular; b) Lamellar; c) Transitional Lamellar; d) Mostly modified structure) [49].

1.2.7.1 Eutectic Si Modification Modifying Agents

The process of chemical modification involves certain elements, and for modification to take place, the ratio of the modifying element's atomic radius to that of silicon should be around 1.64. Figure 1.20 presents a graph displaying the ratio of common modifying agents to the atomic radius of silicon. When an element's atomic radius ratio to silicon is greater than 1.65, growth twins form at the interface. Chemical modifiers are more effective at higher cooling rates, increasing the matching frequency and branching angle alongside the modifying agent and cooling rate. Some common chemical modifiers include K, Ba, Rb, Na, Ca, Sr, La and Ce. Elements such as arsenic,

antimony, selenium, and cadmium create a layered structure when used as modifiers. More modifying agents might be required than the alloy's silicon ratio.

Iwahori et al. discovered that Sr melt treatment raises the H concentration in the melt [49-50]. They observed that the addition of Sr to the melt impacts porosity formation in Al-7%Si alloys and suggested a link between the oxide number and porosity for Sr-modified A356 alloy. In addition to Sr's modification benefits, it is believed that Sr lowers the molten alloy's surface tension, potentially causing porosity formation with increased wt.% content [51]. However, this property may enhance the molten metal's feedability into the mold.

Upon conducting thermal analysis and derivative analysis initially on both hypo-eutectic and eutectic alloys in both altered and unaltered states, it was observed that the variety and composition of strontium intermetallic phases were unaffected, regardless of the change in alloy content [52]. The eutectic modification in aluminum-silicon alloys can be attributed to the impact of TiB_2. The change in the Aluminum-Silicon eutectic is brought on by TiB_2 within these alloys. This interaction is a consequence of TiB_2 particles' engagement with eutectic aluminum-silicon and their sequestration into the eutectic phase boundaries [53].

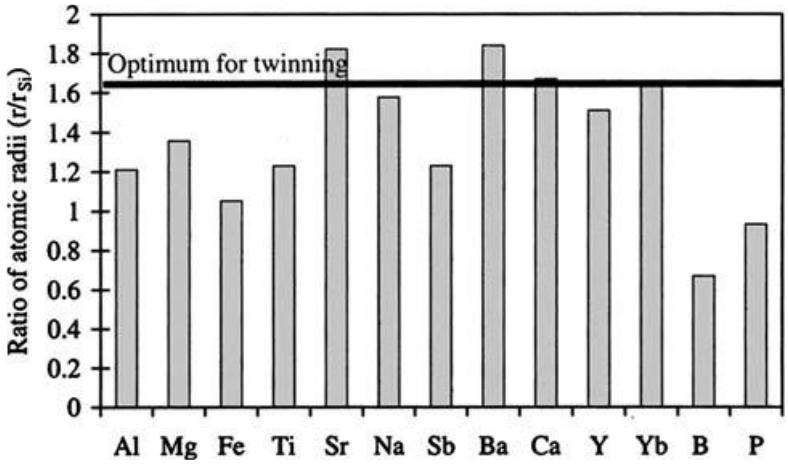

Figure 1.20: Graph depicting the ratio of silicon's atomic radius for various alloy elements and modifiers [52].

1.2.7.2 Eutectic Si Modification Mechanism

Thanks to Nogita and Dahle, the differing behaviors of eutectic Al phase in unmodified and Sr-modified alloys can be understood. The nucleation modes can be seen in Figure 1.21. When the eutectic cores are positioned at or near the dendrite-liquid interface, as shown in the figure, the Aluminum phase is likely to have the same orientation as the dendrites found in unmodified hypoeutectic alloys.

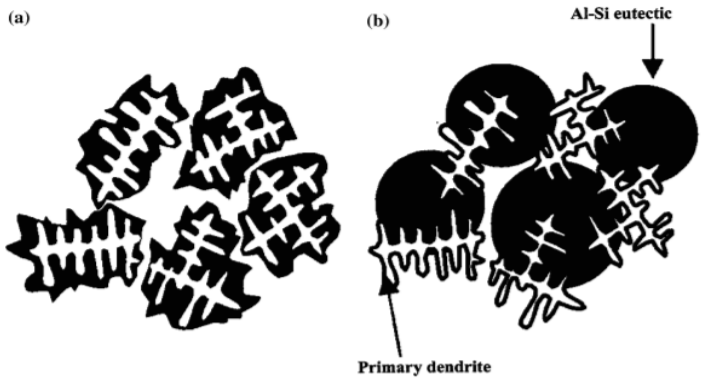

Figure 1.21: Hypoeutectic Aluminum-silicon alloy eutectic solidification patterns: (a) nucleation and growth on primary aluminum dendrites; (b) separate heterogeneous nucleation within the interdendritic liquid. [52].

As depicted in Figure 1.21, the process of heterogeneous nucleation occurs on impurities found in the interdendritic fluid. Here, it's not possible for eutectic aluminum to align in the same direction as the surrounding dendrites. Furthermore, the eutectic solidification process can be broken down into three distinct categories: Mode I, where nucleation happens close to the tips of dendrites; Mode II, involving nucleation and growth within the gaps of interdendritic spaces; and finally, by adding modifier elements to the commercially pure alloy, the process of solidification can switch to Mode III, or a mixture of these modes. This mechanism is speculated to include the deactivation of AlP particles [52]–[54].

Eutectic solidification mode can influence the diffusion entrance of the semi-solid zone on the process of the crucial stage of solidification, as well as pore occurance in Aluminum-Silicon alloys [52]. Grain size in strontium-modified alloys is larger compared to other modified alloys. In the presence of AlP or Na, Sr in the molten metal becomes interacted with Si, resulting in a larger grain size in Na- or Sr-modified alloys. The solidification of grains is related to interface velocity [54]. Recent findings suggest

that only strontium, among unmodified elements, is uniformly distributed in the eutectic silicon phase [55]. Three parameters constitute thermal conditions during solidification: thermal gradient, cooling rate, and interface speed. It is known that higher cooling rates yield refined structures. Eutectic particles modified with Sr formation on the surface of dendrite and fill the dendrite envelope, rather than growing from the ends of the dendrite [56].

In unmodified alloys, the pattern of nuclei spread in the melt signifies the total quantity of potential active particles, where the AlP particles are considered the strongest nuclei. When all AlP particles are eradicated or deactivated, there will be a reduction in the number of nuclei, resulting in the need for increased supercooling. The concept of eutectic Si phase modification through sodium or strontium poisoning, known as the TPRE mechanism, was suggested by Hellawell [57]. The impurity (Na or Sr) adsorbs to the re-entrant edge regions, preventing or delaying the attachment of Si atoms. This results in Si atom overcooling, causing more frequent overgrowth and increased twinning in the aluminum phase. The increased supercooling here stems from the loss of the TPRE mechanism, where there is a simple increase in kinetic supercooling, as seen in quenching modification. The alteration in silicon structure is primarily attributed to the modification growth, rather than the nucleation process [58]. The formation of the Si phase is significantly influenced by the phosphorus level.

1.2.8 Al-Nb-B Grain Refiners

Numerous research on aluminum alloy grain refinement have found that Al-Ti-B master alloys are effective when silicon concentrations are less than 3 wt.%. This is due to the formation of titanium silicide as silicon content in the aluminum alloy increases, resulting in a reduction of TiB_2 particles. Various grain refiners have been studied, including Al matrix master alloys containing Ti, Ti-B, Ti-C, and B. Since most of these master alloys contain Ti, the potential for poisoning negatively impacts the grain refinement of Al-Si-Mg cast alloys. In the absence of titanium, Al-B is highly effective as a grain refiner. However, even with titanium concentrations as low as 0.1 wt.%, grain refinement effectiveness is reduced. When the cast material is free of titanium, Al-B functions as an efficient grain refiner. Nonetheless, poisoning occurs when titanium content surpasses 0.4 wt.%[59].

Recent studies have revealed that niobium master alloys can serve as grain refining agents for Al-Si-Mg cast alloys [60]–[63]. Nowak conducted comprehensive experimental research on Nb-B master alloys in both pure aluminum and Al-Si eutectic alloys, comparing their performance to other commercial grain refiners [64]. He observed that Al_3Nb and NbB_2 have lattice parameters similar to those of Al_3Ti and TiB_2. There are several reasons why niobium-boron master alloys are viewed as potential substitutes for Al5TiB, including their similarity in lattice parameters to titanium boride and titanium aluminide for acting as nucleants for α-Al dendrites, as shown in Table 1.6. Additionally, niobium has greater thermal stability than titanium and a lower chemical affinity to bond with Si to form silicide compounds in the casting temperature range of Al-Si alloys, as illustrated in Figure 1.22. However, the growth restriction factor (Q) is significantly lower for niobium than for titanium, with Q (m(k-1)) values of Ti=220 and Nb=6.6 [65].

Table 1.6: Lattice Mismatch Table of Ti and Nb Included Nucleants for Aluminum Matrix [60]

Element	Phase	Melting point (°C)	Density	Lattice structure	f(%)
Aluminum	Al	660	2.7	FCC	-
Titanium	Ti	1668	4.51	Hexagonal	37.3
	Al3Ti	1350	3.36	Tetragonal	4.2
	TiB2	3230	4.52	Hexagonal	34
	TiC	3160	4.93	FCC	-6.5
Niobium	Nb	2468	8.57	BCC	22.7
	Al3Nb	1680	4.54	Tetragonal	4.2
	NbB2	3036	6.98	Hexagonal	30.6
	NbC	3490	7.82	FCC	-8.6

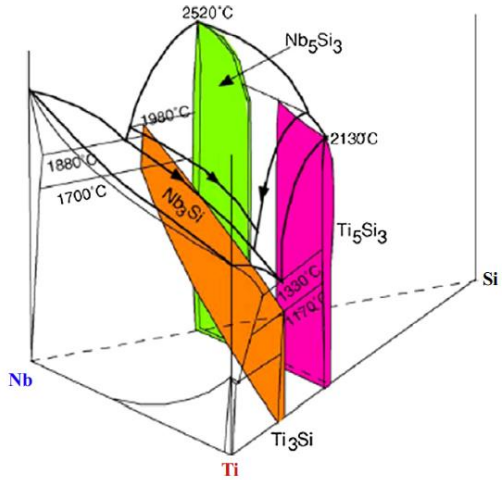

Figure 1.22: The Nb-Ti-Si ternary system demonstrates that Ti-Si compounds form and maintain stability at lower temperatures in comparison to Nb-Si compounds. [60].

To compensate the Q value disadvantage of Nb on grain refining of Al-Si alloys, novel attempts have done by Li et. al. by using Ti addition into Al-Nb-B system [66]. They observed that TiB_2 thin layer shell that forms on the surface of NbB_2 nucleant can refine Al-7-10Si melts mixing hindering effect of Ti such as poisoning by forming titanium silicide formation and positive effects of Nb such as having low lattice mismatch on aluminum matrix, lower intrinsic susceptibility to form silicides inside melt on casting temperatures of Al-Si alloys [67]–[69]. In conclusion, an efficient Al-Ti-Nb-B grain refining agent with a Ti:Nb proportion of 1:4 and an M(Nb+Ti): B proportion of 8:1 has been devised and applied, effectively shrinking the average grain size of Al-10Si alloy to a range of 109-125 μm when 500-1000 ppm M is added. Unlike Al-Si-Ti-B and Al-Si-Nb-B systems, the collaborative impact of Ti/Nb in the Al-Si-Ti-Nb-B system encourages the generation of powerful MAl_3 during the solidification process and produces a TiB_2-NbB_2 core-shell configuration in MB_2. Both aspects contribute to the heterogeneous nucleation of α-Al as solidification occurs, resulting in a substantial decrease in grain size.

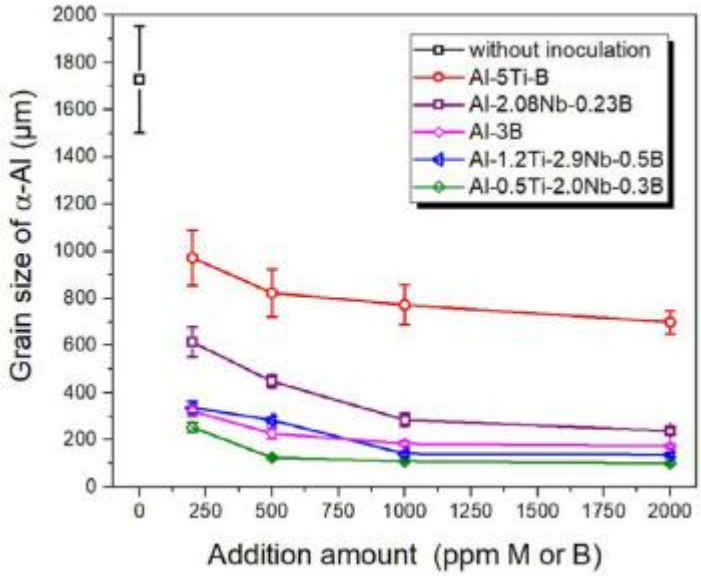

Figure 1.23: Grain size comparison table of Al-Si ingots inoculated with B, Ti-B, Nb-B and Nb-Ti-B master alloys [66].

1.3 Fundamental Optimization Methods on Engineering

In the field of engineering, optimization methods play a vital role in improving the performance, efficiency, and overall quality of various processes and systems. These

techniques enable engineers to find the best possible solutions, considering numerous input parameters, constraints, and objectives. Three widely employed optimization methods in engineering include Design of Experiments (DoE), Artificial Neural Networks (ANN), and neuro-regression methods. DoE serves as a powerful statistical tool for discovering new processes, enhancing existing ones, and optimizing them for better performance [70]. By conducting a set of planned experiments, engineers can systematically investigate the effects of multiple factors on the system's output, allowing them to make informed decisions on process improvements. DoE techniques facilitate effective data analysis, reducing experimental errors and minimizing the impact of noise on the results. ANN represent a subfield of artificial intelligence inspired by the human brain's structure and function. ANN models consist of interconnected nodes, or neurons, organized into input, hidden, and output layers. These networks are capable of learning complex relationships between input and output variables through training on large datasets. In engineering, ANN has found widespread application in various optimization problems, such as predicting material properties, system modeling, and fault detection [71]–[73]. Neuro-regression methods combine the power of neural networks with traditional regression techniques to create robust models capable of tackling complex, non-linear problems. By integrating the flexibility and learning capabilities of neural networks with the mathematical rigor of regression models, neuro-regression methods offer a potent solution to many optimization challenges in engineering [70].

In conclusion, optimization methods such as DoE, ANN, and neuro-regression have become indispensable tools in engineering, enabling practitioners to explore, understand, and enhance various processes and systems. A comprehensive understanding of these techniques can lead to innovative solutions on investigating the unknown phenomenon of composition engineering of Al-Si alloys, which is the main target of this study.

1.3.1 Regression with Design of Experiment

DOE serves as a valuable instrument for discovering new processes, deepening the understanding of existing processes, and optimizing them for top-notch performance. Choosing appropriate statistical tools for data analysis is essential, as outcomes can be significantly influenced by noise. The foundation of statistical techniques in DOE is

built upon duplication, randomization, and compartmentalization. Duplication involves repeating an experiment to improve accuracy and minimize errors. Randomization determines the arbitrary order of experimental runs. Compartmentalization seeks to separate known systematic biases and avoid the masking of primary effects [74].

In manufacturing processes, experiments are conducted to enhance knowledge and comprehension of the processes. Consequently, the connection between key input factors and output behaviors can be examined [74]. One widely adopted strategy in engineering firms, promoted by numerous engineers, is One-Variable-At-a-Time (OVAT). In this approach, one parameter is altered at a time while all other factors remain constant throughout the experiment. However, the results can be unreliable, inefficient, and may yield misleading conclusions regarding the processes. If a specific characteristic of a component is influenced by multiple factors, then DOE is the better choice [75].

Engineers often make systematic changes to input parameters and determine how output performance varies. It is well-known that not all parameters have the same impact on results. Thus, the purpose of a well-planned design is to identify which process parameters have a more significant effect on the output and then pinpoint the optimal levels for these factors [75]. This approach delivers high process efficiency, more consistent results, reduced manufacturing costs, and time savings for researchers.

1.3.2 Artificial Neural Network

AI involves the comprehension, imitation, and execution of human intellect through artificial devices and systems. Aspects of human intelligence include learning, logical thinking, and self-adjustment. Various methods seek to represent the transformation of data into knowledge by simulating human intelligence and its problem-solving capabilities. These methods encompass ANN, genetic algorithms, fuzzy logic systems, machine learning, and probabilistic thinking. ANNs depict a computational framework adept at tackling complicated issues using a "synthetic reasoning mechanism" inspired by the human brain's organization. These networks excel at examining complex situations when the associations between input and output data remain undefined. They

offer an intelligent data processing system with adaptive learning traits. system with adaptive learning characteristics.

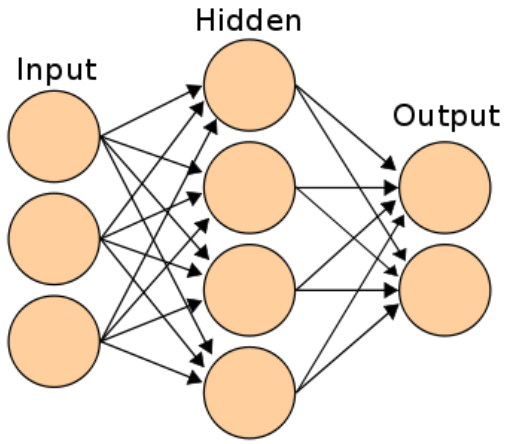

Figure 1.24: Schematic diagram of an ANN Model.

1.3.2.1 Neural Network Model

An ANN structure consists of key elements such as numerous inputs and outputs, concealed layers, connected weight values, and neuron threshold levels. Fig. 1.27 demonstrates the multi-layer perceptron-based ANN configuration, which consists of multiple nodes and layers. MLP connects perceptrons in a specific direction, enabling the flow of data and calculations from input to output. The number of layers in an ANN corresponds to the quantity of perceptron layers. A multi-input multi-output (MIMO) system offers a framework for concurrently linking and modeling inputs and outputs. This neural modeling necessitates only one integrated data file for a single run, in contrast to multi-input single-output (MISO) systems, which require several simulation runs and individual input data files for each output. Additionally, the MISO system fails to capture the interconnected behavior of operational variables. By applying a transfer function to the weighted sum of its inputs, the output from a specific neuron is derived [71]. These outputs then serve as inputs for other neurons. This can be mathematically represented in equation (15) as:

$$a_{jk} = f_k\left(\sum_{i=1}^{N_{k-1}} w_{i_{jk}}\alpha_1 \cdot (k-1) + \beta_{jk}\right) \tag{15}$$

In this equation, α_{jk} signifies the outputs of neuron j in layer k, while β_{jk} denotes the bias weight for neuron j within layer k. The model fitting parameters, w_{ijk}, represent the connection weights, and f_k's correspond to the activation functions.

1.3.2.2 Understanding the Network Training Error

The deviation between the predicted values by the network and the actual target values is termed the network training error. One of the most prevalent error functions in ANN models is the sum-of-squared error (or a proportionate version). The sum-of-squared error is determined by squaring the disparity between the network's predictions for each training pattern and the respective target value (actual measurement) for that specific pattern, which can be formulated as:

$$E = \frac{1}{2} \sum_{i=1}^{N} \sum_{j=1}^{c} \left(t_{ij} - \hat{t}_{ij}\right)^2 \tag{16}$$

In this equation, N denotes the total count of training instances, while C signifies the quantity of network outputs. Equation (16) defines t_{ij} as the intended (measured) output for the i'th training instance and the j'th network, and $\hat{t}_{ij}$ as the network's prediction for that particular instance. Utilizing the root-mean-square (RMS) error is frequently more feasible than the unscaled sum-of-squared errors, as the latter escalates with the increase in the number of training patterns [72].

1.3.3 Neuro-Regression Approach

In the modeling phase, a hybrid method developed and enhanced by Aydin et al. merges the benefits of regression analysis and ANN to improve prediction accuracy [70]. With this strategy, data is divided into two portions, assigning 80% and 20% to each set. The initial segment of data is utilized for training, while the latter portion serves for testing. During training, the objective is to minimize the error between experimental and predicted values by fine-tuning the regression models and their coefficients. Following this, the testing phase is executed to acquire the prediction outcomes while reducing regression model discrepancies, offering insights into the

potential model's predictive capabilities. Subsequently, it is essential to verify the candidate model's limits for specified values to evaluate its realism. After obtaining suitable models in terms of R2 for training and testing, the maximum and minimum values of the models within the given range for each design variable are computed to achieve this. As a result, the selected models fulfill various criteria required for realism.

Aydin et al. illustrated the optimal data processing flow for attaining ideal solutions in Figure 1.25 as follows:

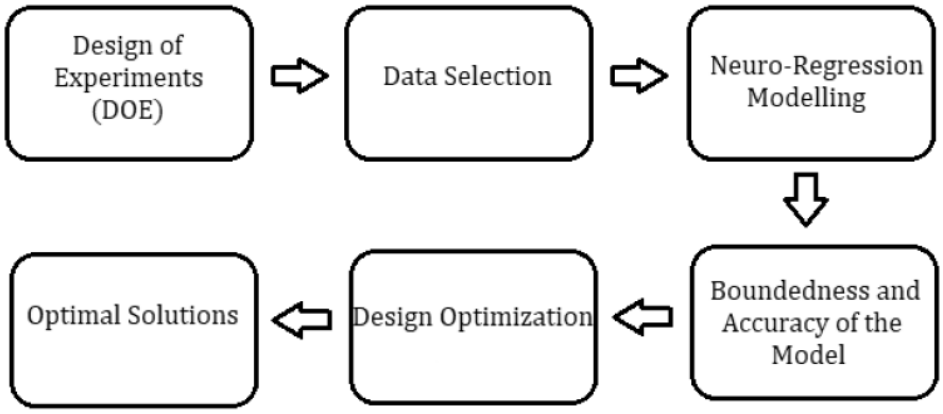

Figure 1.25: Flow schematic of an optimal design process[70].

Chapter 2

Material & Method

2.1 Materials

2.1.1 Matrix Material

On this study, A356 with low graded Ti (20-40 ppm; contains 3% of Ti amount compared to commercial A356 Ti amount.) used that obtained from Dubal in ingot form. The reason of the selection of low graded Ti as base material is to avoid multiple inputs of Ti amount. Addition raito of Ti was only controlled by Ti-included master alloy.

Table 2.1: OES Analysis of A356 Alloy (low graded Ti) from Dubal.

Alloy	*Si*	*Fe*	*Cu*	*Mn*	*Mg*	*Zn*	*Ti*	*B*
A356	***7.08***	***0.1665***	***0.0042***	***0.0191***	***0.3640***	***0.0104***	***0.0042***	***0.0002***

2.1.2 Master Alloys

3 different master alloy was integrated to study to inoculate A356 alloy with different ratios of Niobium (Nb), Titanium (Ti) and Boron (B) element and its intermetallic compounds with different stoichiometric compositions.

2.1.2.1 Al-10Nb Master Alloy

Al-10Nb master alloy was obtained from KBM Affilips Holland, in the form of waffle ingot. Inductively coupled plasma mass spectrometry (ICP-MS) results is given in table 2.2. With foundry's commercial elemental analysis Optical Emission Spectroscopy (OES), it is not able to determine Nb amount in alloy due to lack of reference tube of Nb which is not used in Al casting foundries.

Table 2.2: ICP-MS Results of Al-10Nb Master Alloy.

Master Alloy	*Nb (%)*	*Fe (%)*	*Si (%)*	*Cu (%)*	*Mg (%)*	*Al*
Al-10Nb	***10.7***	***0.24***	***0.15***	***0.04***	***0.001***	***Remainder***

2.1.2.2 Al-10Ti Master Alloy

Al-10Ti master alloy was obtained from Marmara Metal Turkey, in the form of waffle ingot. OES results is given in table 2.3.

Table 2.3: OES Results of Al-10Ti Master Alloy.

Master Alloy	*Ti (%)*	*Fe (%)*	*V (%)*	*Si (%)*	*Others (%)*	*Al*
Al-10Ti	***9.41***	***0.16***	***0.315***	***0.07***	***<0.03***	***Remainder***

2.1.2.3 Al-4B Master Alloy

Al-4B master alloy was gathered from STNM China in the form of waffle ingot. Due to low atomic weight, emission wavelength, matrix effect and excitation energy problematics of boron, ICP-MS test was done to analyze master alloy's composition which was indicated test results on table 2.4.

Table 2.4: OES Results of Al-4B Master Alloy.

Master Alloy	*B (%)*	*Si (%)*	*Mg (%)*	*Fe (%)*	*Al*
Al-4B	***3.6***	***0.19***	***0.11***	***0.02***	***Remainder***

2.1.2.4 Al-15Sr Master Alloy

As mentioned in 1.2.7.1 on previous chapter, eutectic modification is a must for Al-Si casting alloys for refined eutectic Si phase distribution, length, thickness, and size. In this study, commercial eutectic modificator Sr element was used in the form of Al-15 Sr master alloy, extruded rod shaped. Chemical composition is shown in Table 2.5.

Table 2.5: OES Results of Al-15Sr Master Alloy.

Master Alloy	*Sr (%)*	*Others (%)*	*Al*
Al-15Sr	***14.8***	***<0.03***	***Remainder***

2.2 Casting Mold

Specially designed 5-spoke mold was used for obtaining casting specimens. In order to obtain different cooling rates that was typically converged to low pressure die casted aluminum wheel's cooling regime (inner flange, spoke and hub, respectively), inlet of casting is location that was shown in figure 2.1. Spoke 1 and 5 which give 1.5-2 C°/s , spoke 2 and 4 propose 1-1.5 C°/s, and lastly spoke 3 ensures 0.5-1 C°/s cooling rate range from dendrite phase nucleation point to eutectic phase solidification of A356 alloy. AISI H13(X40CrMoV51) tool steel was used as mold material. Pyrotek Dycote 39 casting coating was applied on mold surface for avoiding any casting defects like pinning and mold erosion. Mold temperature was controlled strictly on 350 C° (±5 C°) for proper analysis of outputs of tensile test results, which directly affects cooling rate of melt alloy.

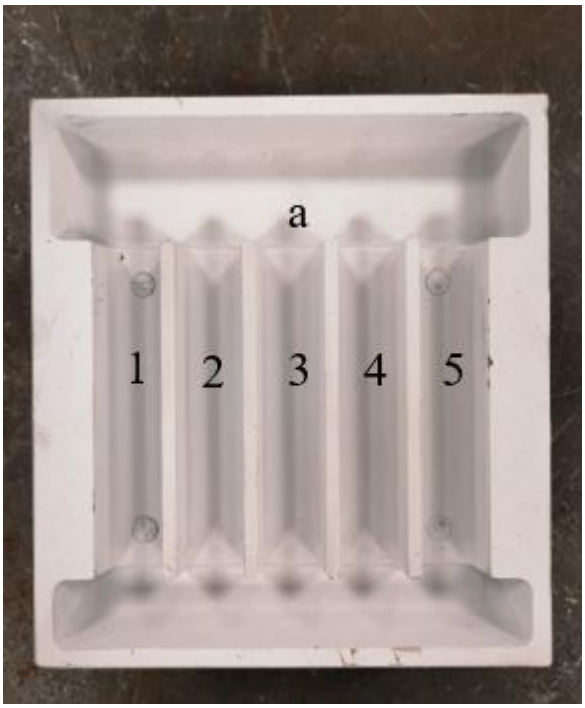

Figure 2.1: Permanent mold which indicated a) as inlet section 1) as spoke 1, 2) as spoke 2, 3) as spoke 3, 4) as spoke 4, and 5) as spoke 5.

2.3 Design of Experiment

As the main approach of this study is to optimize the inoculation process in terms of addition ratios of Nb, Ti and B elements on A356 alloy, General Factorial Regression and Neuro-Regression methods were selected. In order to step into optimization path, detailed experiments had to be done in a proper way to observe effects of inputs to output parameters. Therefore, DoE methodology were used for specimen's casting. DoE structure was determined as 3 inputs with 3 equi-distanced level, with 2 replicate specimen production. Full factorial set was selected for optimum resolution of experiments. Design summary list and whole experimental table is given in Table 2.6 and Table 2.7.

Table 2.6: Design Summary of the Full Factorial DoE set.

Name	Type	Levels	Level Values		
Nb	Numeric	3	200	1100	2000
Ti	Numeric	3	200	1100	2000
B	Numeric	3	200	1100	2000

Table 2.7: Experimental list of this study with aimed composition in terms of "ppm".

RunOrder	Nb ppm	Ti ppm	B ppm
1	200	200	200
2	200	200	1100
3	200	200	2000
4	200	1100	200
5	200	1100	1100
6	200	1100	2000
7	200	2000	200
8	200	2000	1100
9	200	2000	2000
10	1100	200	200
11	1100	200	1100
12	1100	200	2000
13	1100	1100	200
14	1100	1100	1100
15	1100	1100	2000
16	1100	2000	200
17	1100	2000	1100

18	1100	2000	2000
19	2000	200	200
20	2000	200	1100
21	2000	200	2000
22	2000	1100	200
23	2000	1100	1100
24	2000	1100	2000
25	2000	2000	200
26	2000	2000	1100
27	2000	2000	2000

2.4 Casting Process

For each DoE input set, composition was adjusted on desired level. Before that, 4 kg of A356 with less Ti was melted on A15 SiC crucible on Protherm Electrical Resistance Furnace at 850 C° that can be seen on Figure 2.2.

Figure 2.2: Protherm Electrical Resistance Furnace.

On the inoculation step, desired amount of Al-10Nb, Al-10Ti and Al-4B master alloys were weighed on precision scale in terms of g. All addition calculations were done based on ICP-MS results of each master alloy. Results will be mentioned on chapter 3. Weighed master alloys inoculated into crucible with mechanical stirring right after dross removal from top of the melt, as can be seen at Figure 2.3.

Figure 2.3: Master alloy inoculation with manual stirring process for A356 melt.

Right after stirring, crucibles were put electrical resistance furnace again at 850 C° for homogenization of intermetallic particles within melt for 30 minutes. Afterwards, homogenized melt placed onto refractory plate of continuous heating furnace by Protherm, that prevents heat loss during degassing. Whole degassing system can be seen in Figure 2.4 and Figure 2.5. Plate was descended to ensure capture graphite rotor inside crucible when degassing operation starts. Right after that, second dross removal was done to avoid bi-film and inclusion entrapment into melt with rotor's radial rotation movement. Degassing operation was done with Dogus Metal's special designed degassing machine for A15-A16 SiC crucible. Degassing parameters were, 60 seconds of mixing (The gas output was fixed at 2 L/min Argon gas to prevent melt from entering the rotor gas outlet duct.), 60 seconds of washing for hydrogen gas and bi-film removal with 7 L/min Argon gas. Rotary degassing application can be seen on Figure 2.5. Whenever degassing operation was finished, melt temperature stabilized inside the continuous melting furnace at 750 C°. On the other hand, mold temperatures

were set to 350 C°. For every DoE set, these steps were repeated with same parameters but different master alloy addition combinations.

Figure 2.4: a) Rotary Degassing Machine and b) continuous heating furnace that designed to work as pair.

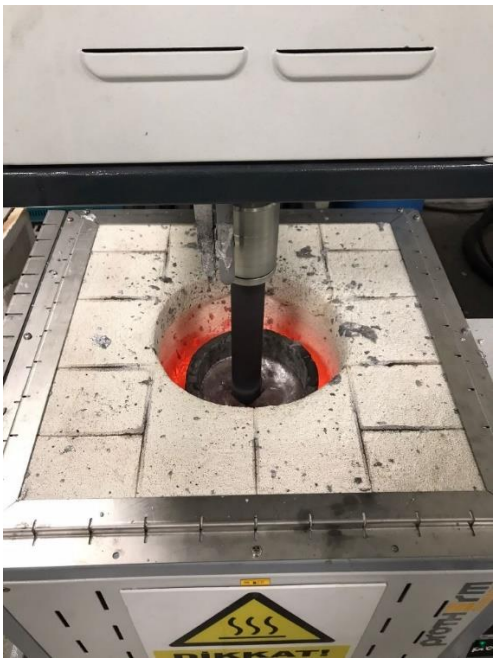

Figure 2.5: Rotary degassing process that proceeds inside continuous heating furnace to sustain temperature stability of melt.

Whenever degassing operation was finished, melt temperature stabilized inside the continuous melting furnace at 750 C°. On the other hand, mold temperatures were set to 350 C°. For every DoE set, these steps were repeated with same parameters but different master alloy addition combinations.

In order to examine whether degassing operation is perfectly done or not, Reduced Pressure Test (RPT) were used before and after degassing operation as it can be seen on Figure 2.6.a. RPT device has a capability to solidify 2 sample in a steel mold (Figure 2.6.c) in a same time while one of them has been solidified under vacuum medium at 80 mbar pressure, other one has been solidified on atmospheric pressure. Density of samples (Figure 2.6.b) were determined by Archimedes principle. With the ratio of these sample's densities that only related with sample's volume difference, Density Index (DI) value was found. Lower DI means clean melt within oxide and H gas, vice versa.

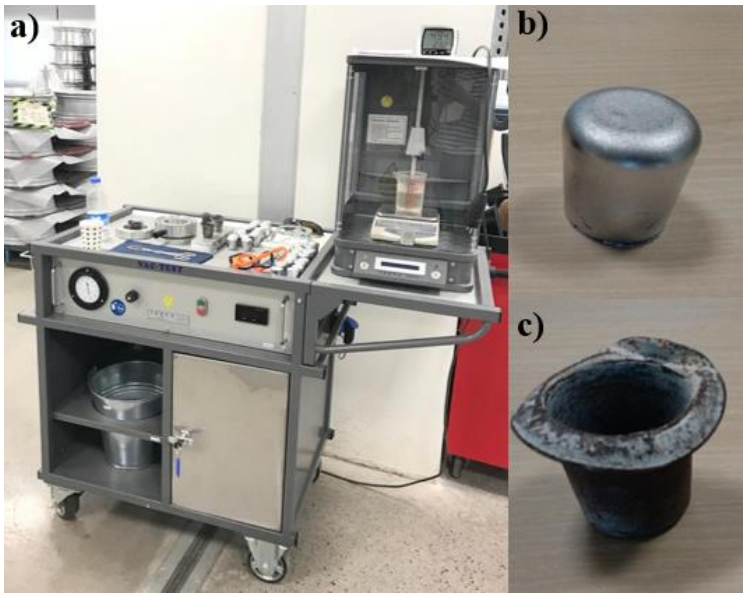

Figure 2.6: a) IDECO Reduced Pressure Test Device, b) RPT cast sample and c) RPT steel mould.

2.5 Heat Treatment

54 of cast specimens were heat treated by T6 standard on CMS Wheels' specialized T6 heat treatment facility for aluminum casting wheels. Specimens were exposed to

540 °C for 4 hours for dissolving of Mg_2Si compound into the α-Al matrix. Right after that, specimens were water quenched on water chamber at narrow temperature range. Then, specimens were artificially aged at 160 °C for 3 hours to enhancement of diffusion flux of metastable Mg2Si particulates to increase toughness of alloy. All heat treatment procedure of each cast specimen was handled in one batch to reduce the heat treatment furnace's effect on tensile test results.

2.6 Tensile Test

Tensile test bars are machined from cast part with DIN EN ISO 6892-1 standard as it can be seen on figure 2.7. 5 bars were obtained from 1 heat treated cast part, totally 270 tensile test bars for this study.

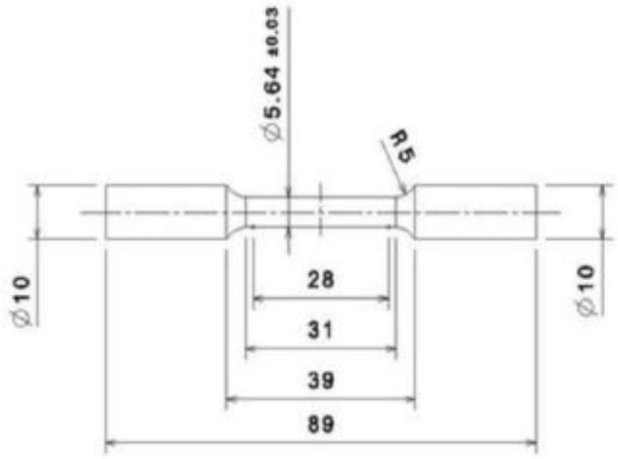

Figure 2.7: Schematic of DIN EN ISO 6892-1 tensile test bar standard.

Tensile test was proceeded on Zwick Roell Z100 Tensile Test Device with the parameters of $5N/mm^2$ tensile test speed and 100kN force.

2.7 X-Ray Diffraction (XRD) Measurement

X-Ray diffraction analysis was performed for determination of phases with their 2θ values that comes from crystal structure orientation of exact phase. Intensity-2θ values were graphed with MS Excel. Cast specimens were cut on inlet section (a) that can be seen on Figure 2.1. Then, cast part of inlet grinding with aluminum file for obtaining XRD specimen on particulate form. XRD measurements was done on Panalytical

Empyrean XRD Device which is given in Figure 2.8. Cu-Kα radiation used as a radiating element. Analysis was done on 0.5°/min between 0-90° [76]

Figure 2.8: Panalytical Empyrean XRD Device.

2.8 Chemical Analysis

2.8.1 %Ti and %B Elemental Analysis

For commercial aluminum alloy wheel production, optical emission spectroscopy (OES) has been used since it has fast and precise response capacity for elemental analysis of production line. Since Ti and B element has been found on A356 alloy, OES was selected for % element analysis. RPT samples that solidified on atmospheric pressure was used as OES sample. Thermo-scientific Thermo ARL3460 Metal Analyser Device was used for % control of Ti and B inside cast specimens of DoE set as can be seen on Figure 2.9.

Figure 2.9: a) Thermo-scientific Thermo ARL3460 Metal Analyser Device and b) OES specimen example of DoE set.

2.8.2 %Nb Elemental Analysis

Nb element has not used on commercial aluminum alloy production so that OES uncapable to analyze the % content of Nb inside A356 alloy. Due to that, addition ratio of Nb had to be verified with ICP-MS results of Al-10Nb master alloy that mentioned on 2.1.2.1 section. Known reference specimen that analyzed with ICP-MS method was checked with Aczet Portable X-Ray Florescence (XRF) Device can be seen on Figure 2.10, then device database was adjusted through ICP-MS results of reference specimen by changing Nb element's mass factor on result calculation. Verification table of ICP-MS and XRF results is given on Table 2.8. Thus, all % Nb results was performed with XRF device for each DoE set.

Table 2.8: Verification of XRF Results with ICP-MS output for %Nb content inside A356 alloy.

Master Alloy	**Desired ppm level**	**ICP-MS Result (ppm)**	**XRF Result (ppm)**
Al-10Nb *on A356*	*100*	*112,8*	*122,4*
Al-10Nb *on A356*	500	447,4	478,8
Al-10Nb *on A356*	1000	941,9	935,7
Al-10Nb *on A356*	2000	1810,2	1914,1

Figure 2.10: Aczet Portable XRF Device measurement visualization.

2.9 Optical Microscopy

For conducting metallographic examinations, the specimens were initially cut from inlet section, followed by grinding with SiC paper, then polished using diamond paste. The etching solutions used for metallographic evaluation included 0.5% HF for micro-examinations and $FeCl_3$ for macro-examinations. On Figure 2.11, Metco Bainpol VT Grinding and Polishing Device and its products can be seen.

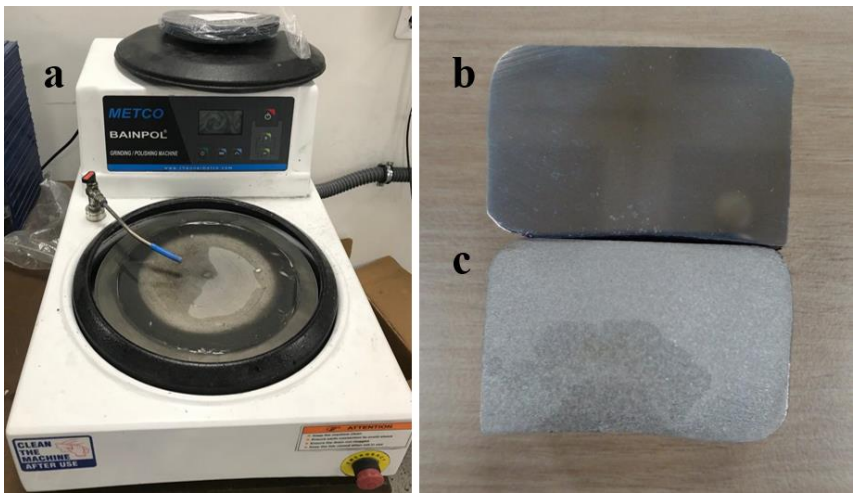

Figure 2.11: a) Metco Bainpol VT Grinding and Polishing Device, b) microstructure and c) macrostructure samples for examination and characterization step.

The equipment utilized for microstructural and macrostructural analyses were Nikon Epiphot 200 (depicted in Figure 2.12 a) and Clemex S2.0C (shown in Figure 2.12 b), respectively.

Figure 2.12: a) Nikon Epiphot 200 Metallography Microscope and b) Clemex S2.0C Macro Camera.

2.10 Scanning Electron Microscope

T6 heat treated tensile test samples' fracture surfaces were grinded and polished for revealing Nb-Ti-B included intermetallics-compounds under SEM secondary electron (SE) detector on various magnifications. On the other hand, EDS detector were performed for point scan and mapping for detecting %element concentration of observed phases on the surface of specimen. None of coatings were used due to no bakelite application as specimen holder for A356 samples. Zeiss Gemini 500 SEM were used for detailed surface and phase examination which located in Izmir Celal Bayar University Applied Science Research Center which is given in Figure 2.13.

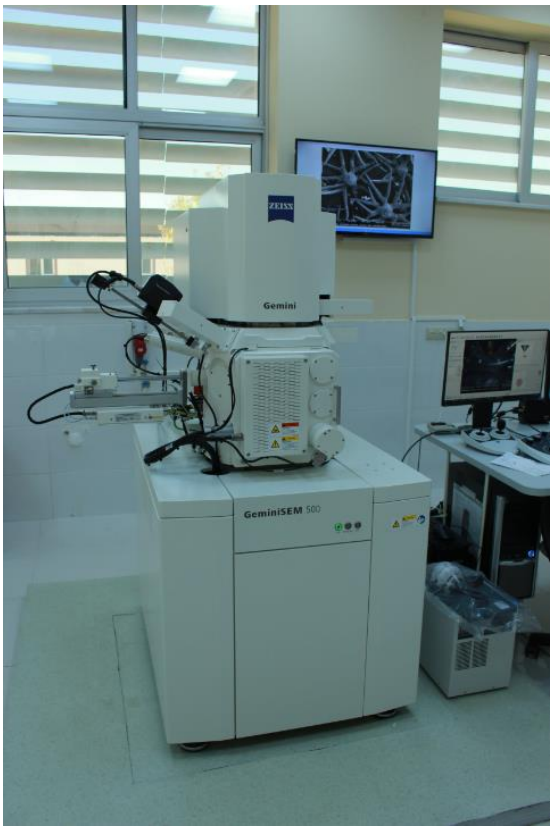

Figure 2.13: Zeiss Gemini 500 Scanning Electron Microscope.

Chapter 3

Experimental Results and Discussion

3.1 Chemical Analysis Results of Samples

With the help of ICP-MS results that was mentioned on Chapter 2. “ppm” calculations were seen to be consistent when OES results (XRF results was added to table for Nb element) DoE set was examined as it can be seen on Table 3.1. As each element was inoculated into melt with different master alloy sources. Controllable final composition with negligible deviations was achieved for 3 OES measurements for each 27 RPT sample that solidified under atmospheric pressure condition as mentioned 2.8.1 section. Deviations from aim concentration were occurred due to oxidation of inoculants during degassing operation and non-homogenous composition distribution of related elements such as Ti. Nb and B on their master alloy sources.

Table 3.1: Chemical Composition of A356 based DoE Samples.

Sample No.	***Si(%)***	***Mg(%)***	***Fe(%)***	***Sr(%)***	***Ti(%)***	***Nb(%)***	***B(%)***
1	7.0906	0.2690	0.0627	0.0163	0.0133	0.0190	0.0240
2	7.1151	0.2671	0.0855	0.0091	0.0122	0.0240	0.1392
3	7.2098	0.2839	0.0786	0.0197	0.0224	0.0190	0.1743
4	7.3185	0.2736	0.0656	0.0191	0.0892	0.0210	0.0202
5	7.0460	0.3023	0.0968	0.0043	0.1460	0.0180	0.1414
6	6.7759	0.2777	0.1007	0.0023	0.1050	0.0390	0.1824
7	6.9758	0.3245	0.1014	0.0213	0.1626	0.0210	0.0143
8	7.2863	0.2822	0.0920	0.0334	0.1885	0.0120	0.0936

9	6.8524	0.2686	0.0953	0.0081	0.1657	0.0140	0.2147
10	6.9760	0.2853	0.0843	0.0195	0.0249	0.0970	0.0271
11	6.9726	0.2875	0.0999	0.0059	0.0014	0.0880	0.1448
12	6.7267	0.2638	0.0908	0.0010	0.0213	0.1170	0.1732
13	7.1447	0.3001	0.0969	0.0216	0.0911	0.1120	0.0191
14	6.8105	0.2889	0.0972	0.0117	0.1348	0.0700	0.1149
15	6.7030	0.2728	0.1035	0.0109	0.1412	0.1140	0.1911
16	7.2177	0.2850	0.0966	0.0194	0.1912	0.1110	0.0272
17	6.7363	0.2715	0.0910	0.0191	0.1983	0.1410	0.1276
18	6.7130	0.2624	0.1046	0.0085	0.1513	0.0113	0.1778
19	6.9661	0.3022	0.0927	0.0192	0.0228	0.1700	0.0307
20	6.8200	0.2701	0.0890	0.0023	0.0337	0.1850	0.1339
21	6.5062	0.2625	0.0942	0.0015	0.0222	0.1510	0.2303
22	6.9313	0.2907	0.0982	0.0190	0.1147	0.1580	0.0261
23	6.7105	0.2792	0.1007	0.0109	0.1465	0.1680	0.0853
24	7.5224	0.2859	0.1039	0.0061	0.1256	0.2100	0.1873
25	6.5423	0.2629	0.0867	0.0196	0.1748	0.1880	0.0346
26	6.4987	0.2812	0.0996	0.0148	0.2258	0.2020	0.1208
27	6.4185	0.2531	0.0968	0.0089	0.1898	0.1710	0.1777

As it can be seen from Table 3.1, Si, Mg, Fe and Sr composition distribute on acceptable limits and it can be inferenced that these compositions are not directly affect heat treatment outputs so the effect of main alloying elements on A356 alloy is assumed as negligible for tensile test results.

When the table 3.1 was examined with a basic statistical approach, aimed composition, and obtained one could be compared in a box-plot graph that created on Minitab 20 as it can be seen on Figure 3.1 to 3.3.

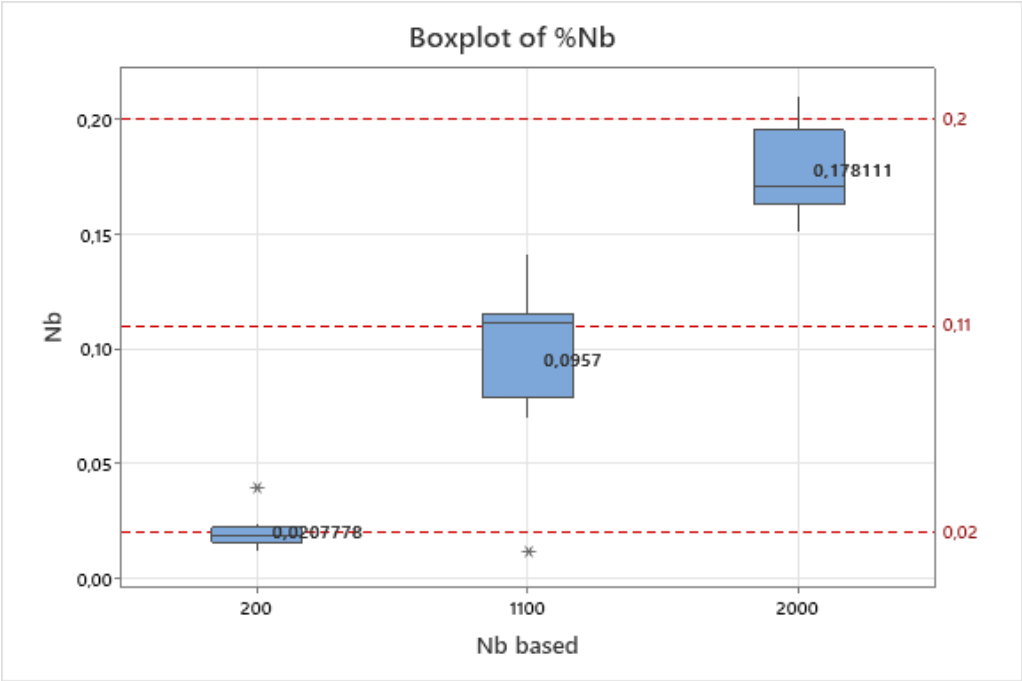

Figure 3.1 Obtained composition distribution of %Nb for each aimed “ppm” level.

Figure 3.1 is shows that aimed ppm level and realized ppm distributions that belong each level in a form of box plot. It can be seen that 200 ppm Nb distribution has almost achieved with narrow interquartile range and one of outlier data., with a mean of 208 ppm. 1100 and 2000 ppm distributions were not reached clearly even if distribution of XRF results for Nb have a tangency with exact composition aims of 1100 and 2000 ppm. 957 ppm and 1781 ppm means were obtained for 1100 and 2000 ppm categories, respectively. It may have concluded in such a way that reduction reaction Al-10Nb master alloy increased with increased master alloy amount and/or non-homogenized composition distribution of Al-10Nb waffle ingots.

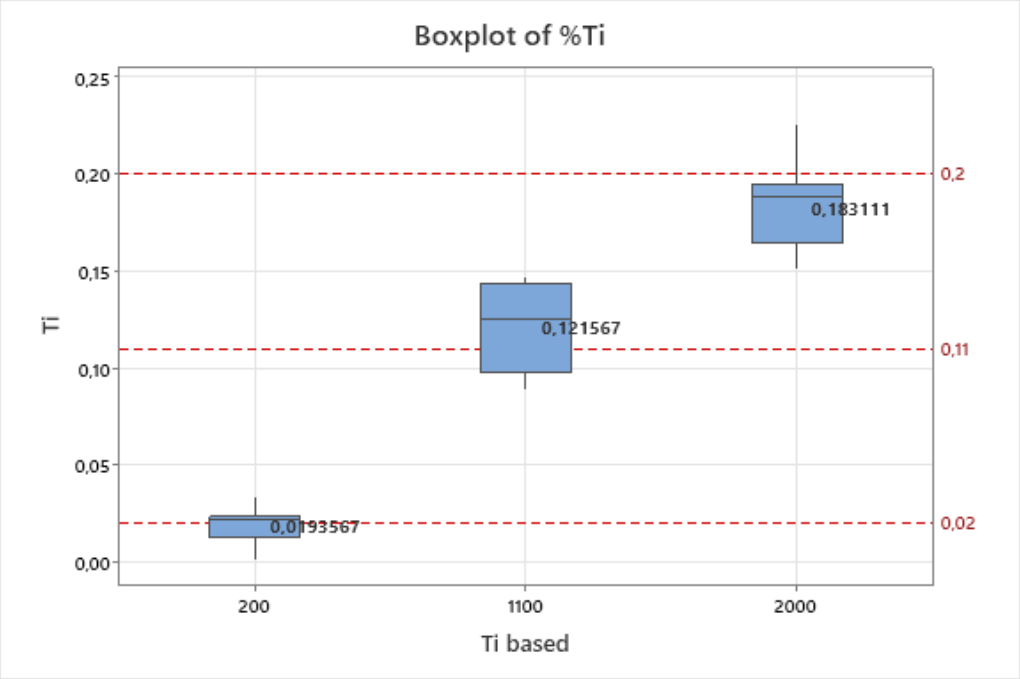

Figure 3.2 Obtained composition distribution of %Ti for each aimed “ppm” level.

As it is indicated on Figure 3.2, %Ti distribution based on each level behave as same %Nb content; relatively lower deviation on low addition levels and rose deviation on higher inoculation amounts. Same concerns are considered on the distribution range behavior of %Ti content. At the very least, low Ti grade A356 usage from Dubal was seen to be logical in terms of avoiding bias of mean concentration of %Ti on each level, as commercial A356 alloy has 0.08%-0.12% of Ti. As summary, 194 ppm, 1216 ppm and 1831 ppm mean values were achieved, respectively for the group the data belongs.

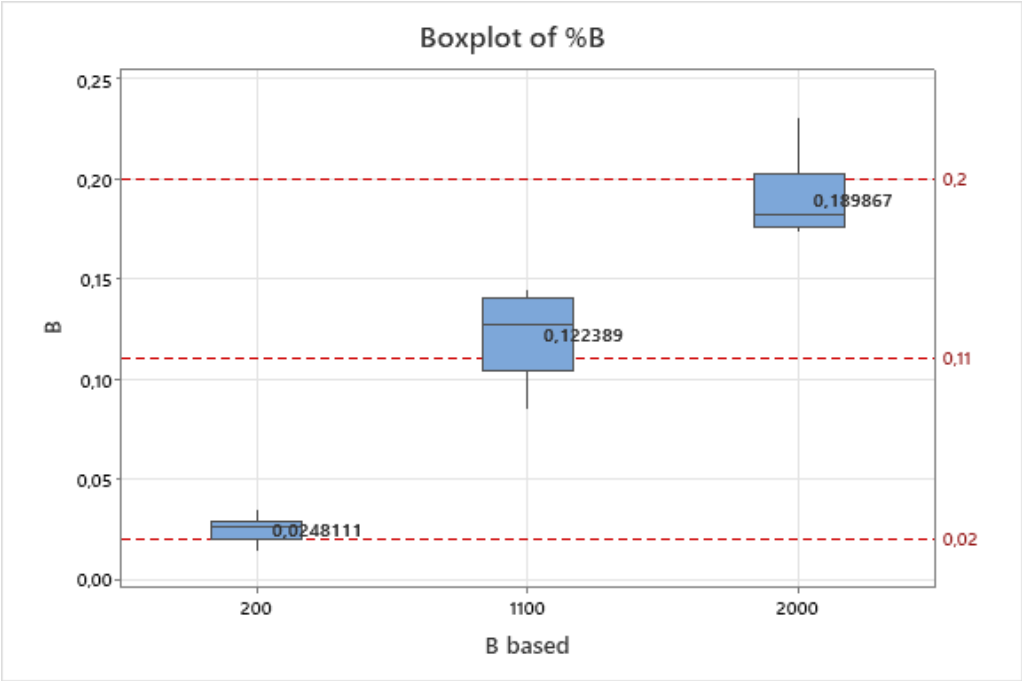

Figure 3.3: Obtained composition distribution of %B for each aimed “ppm” level.

Boron element needs high excitation energy to reveal inside matrix with its low atomic weight. With OES method, B can be excited at needed level thus, thanks to verified ICP-MS results; addition amount for desired level was optimized on inoculation step on degassing. Same trend was observed on 200 ppm addition level target with relatively low composition deviation with the mean of 248 ppm. Other two level’s target have reached with relatively higher deviation with the mean of 1224 ppm and 1899 ppm.

3.2 X-Ray Diffraction Results

RPT samples that solidified under atmospheric pressure were set aside for characterization of phase distribution by XRD method. Selected samples were grinded by aluminum file with the mentioned method on section 2.7. For this analysis, R25 and R27 DoE set were selected due to mechanical performance examination on General Factorial Regression model that constructed on Minitab 20. Minimum and maximum mechanically performed specimens were selected, respectively. More detailed explanation will be given on Tensile Test section. On Figure 3.4 and Figure 3.5, Intensity (Count) – 2θ° graph of R25 and R27 can be seen.

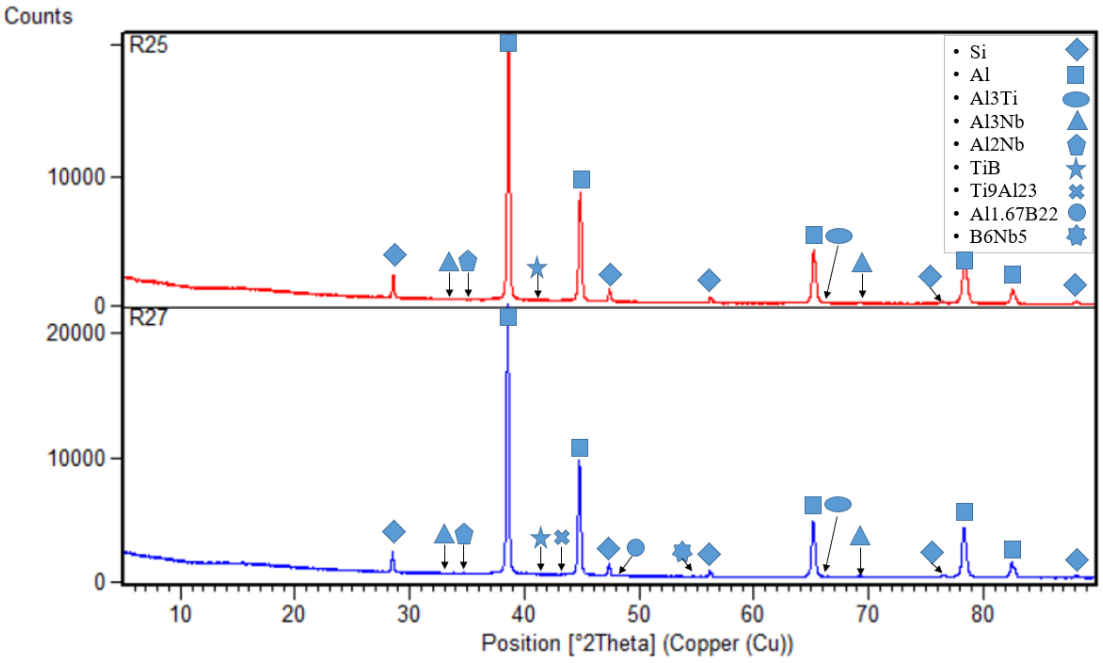

Figure 3.4: XRD analysis that phases present on R25 and R27 sample.

XRD analysis that taken from R25 and R27 showed that in-situ inoculation of grain refiner elements had occurred inside the melt. Besides Al and Si which are main alloying element of A356 alloy, niobium aluminides, titanium aluminides, aluminum boride, niobium boride and titanium boride was found on the detailed database search of XRD analysis on Panalytical X'pert Highscore software. Additionally, due to higher addition ratio of B inside R27 than R25, niobium boride and aluminum boride was formed. Ti_9Al_{23} compound have found in a different stochiometric composition instead Al_3Ti as titanium aluminide.

As depicted on Figure 3.5, section of between 30-38° of XRD Intensity-2θ° graph was zoomed-in for clarifying the peaks of niobium aluminides which are Al_3Nb and Al_2Nb. It was declared by the work of Bolzoni and Babu that peak that was obtained from related section belongs to niobium aluminides [77]. As an exclusion, no aluminum boride and niobium boride was observed on zoomed-in section of analysis.

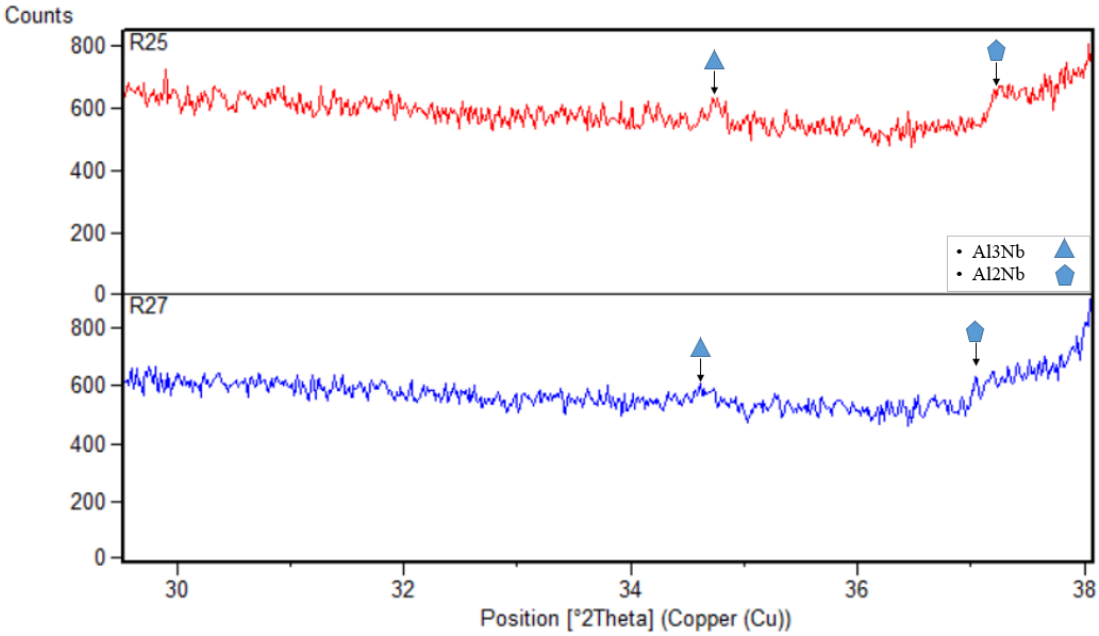

Figure 3.5: Zoom-in section of XRD analysis that was coincided to Niobium Aluminides.

3.3 Tensile Test Results

Main focus of this study is to understand the effect of alloying element's inoculation performance on A356 on the data of tensile test outputs by using both factorial regression and a novel approach, neuro-regression. Each approach needs to get fed by sufficient quantity of data therefore the tensile test data which are Yield Strength (YS), Ultimate Tensile Strength (TS), Elongation (%E) and Quality Index (QI) collected by the help of full factorial DoE with 3 input and 3 level. By the help of boxplot, without excessively long rows and columns, data can be summarized. It is helpful to indicate that each "Run Order" data contains 10 tensile test specimens with different cooling rates as mentioned in section 2.2.

Figure 3.6 shows that the YS outputs of tensile tests of DoE list. As Figure A proposes, maximum data variation with the relatively moderate mean was observed on R21; 2000 ppm Nb, 200 ppm Ti and 2000 ppm B composition target. On the other hand, the highest mean was obtained from R5 with 200 ppm Nb 1100 ppm Ti and 1100 ppm B, which have 203 MPa yield strength with lower deviation.

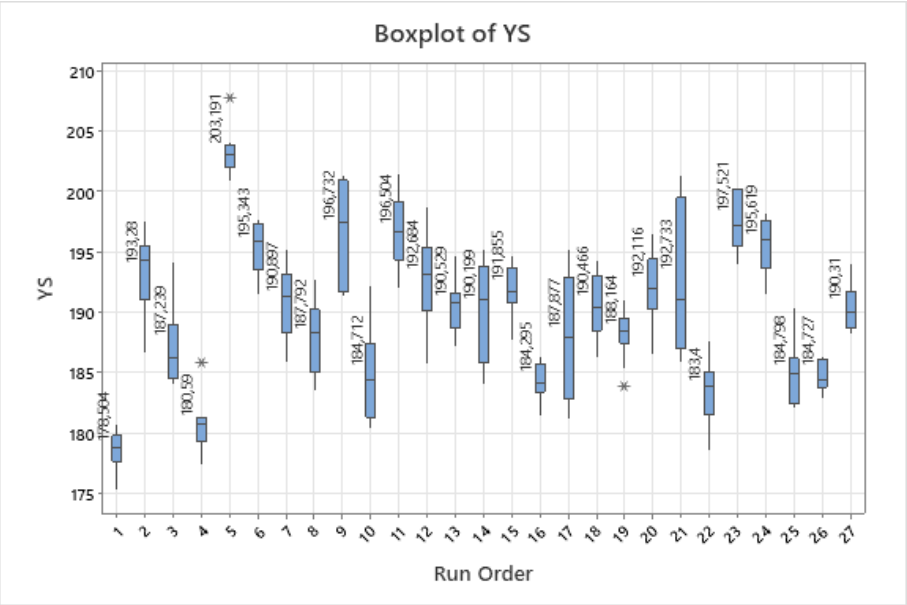

Figure 3.6: Yield Strength Results of DoE Data.

Figure 3.7 indicates the ultimate tensile test results in a boxplot graph. Without considering the deviations, dramatical mean change was not observed. Maximum deviation was seen on R10 set. Smallest data variation again obtained on R5 as YS results of same DoE set. Even if the cooling rate effect is the same for all DoE set as melt temperature and mold temperature were set a narrow range, there are significant deviation differences on data for couple of DoE sets.

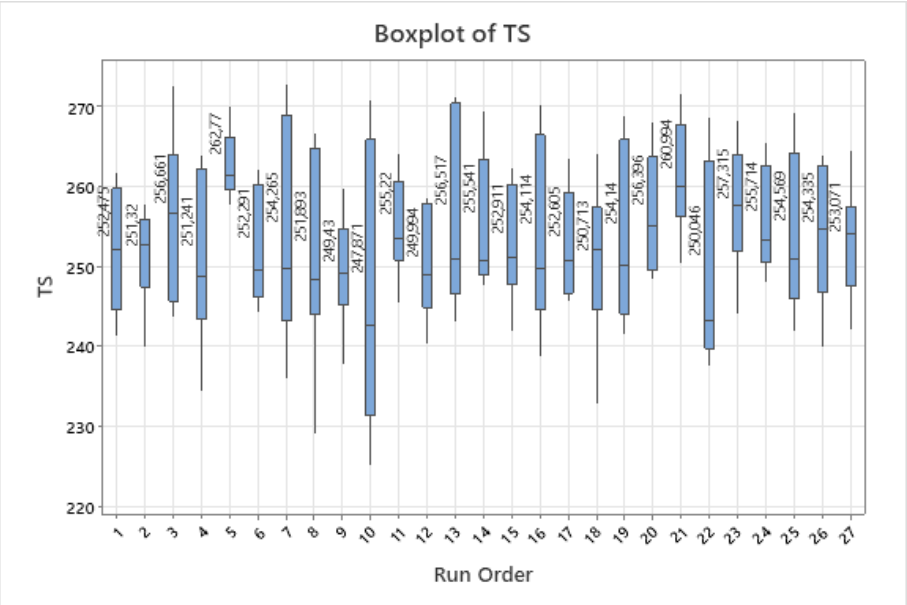

Figure 3.7: Ultimate Tensile Strength Results of DoE Data.

Elongation % value is the most critical term on defining energy damping capacity on material which make sense on designing the composition of Al-Si casting alloys have been used especially for automotive industry. As it can be seen on Figure 3.8, different number of variations on data was observed just only chemical composition difference of Nb-Ti-B system thanks to different grain size and lattice slip resistance mechanism by chemical inoculation by intermetallic nucleants inside melt during solidification. Overall, without considering the composition difference, it can be proposed that 2% elongation value is the minimum limit of the DoE set, which data belongs to tensile bars solidified on low cooling rate condition. Highest deviation in interquartile range was found in R4 composition with 200 ppm Nb, 1100 ppm Ti and 200 ppm B. On the other hand, narrow variation was observed on R5 in interquartile range with the composition of 200 ppm Nb 1100 ppm Ti and 1100 ppm B targets, also with have the highest YS mean DoE set. R1 and R9 sets have the maximum and minimum mean for %E value with 8.4% and 2.8%, respectively. Additionally, R9 and R27 sets have outlier data which are not fit inside their DoE set's data distribution.

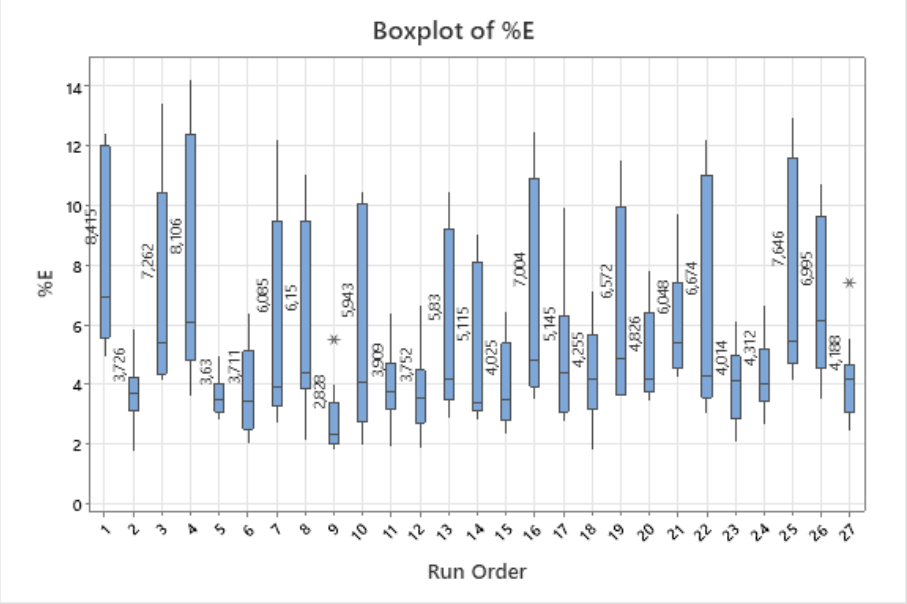

Figure 3.8: % Elongation Results of DoE Data.

QI is the term that exposes overall quality of material by considering the data with a specific determined weight of tensile test outputs such as TS and %E. Although different approaches have been studied and proposed by several researchers for Al-Si casting alloys, in this study QI from Drouzy et al. was selected as it is an Index formula

with a scientifically proven background, which only uses tensile test results as input to the function [78].

$$QI = \sigma_{UTS} + k * \log(\%E) \quad (17)$$

In this formula, Q symbolizes the quality index measured in MPa, σ denotes the maximum tensile strength (UTS) quantified in MPa, and %E signifies the ratio of elongation until the point of fracture. For Al 7Si-Mg alloys, a material constant, represented by k, is fixed at 150 MPa [78].

QI values are summarized on Figure 3.9. As it is interfered that, R1 has the highest mean with 387 MPa, otherwise the lowest one obtained on R9 with 313 MPa.

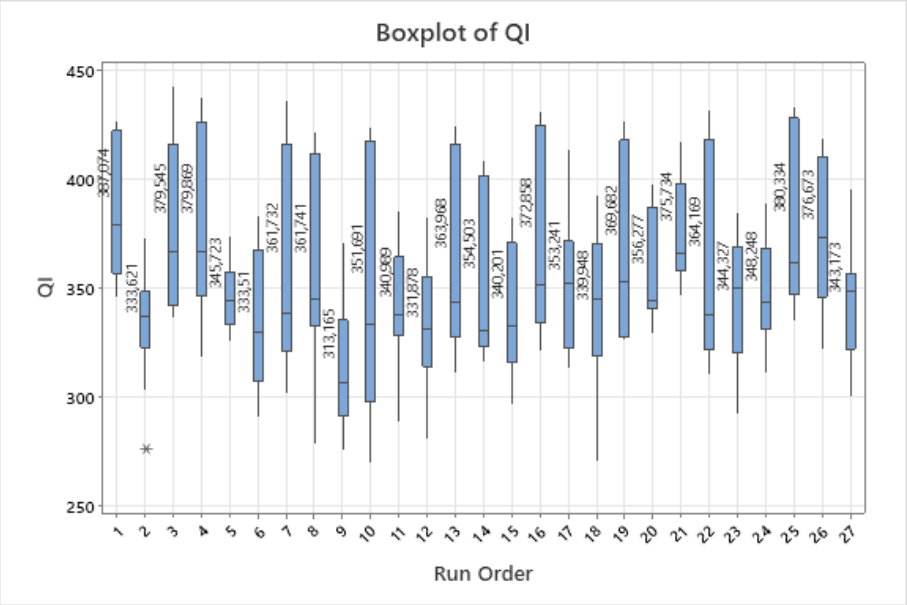

Figure 3.9: Quality Index Results of DoE Data.

In the next step, data was examined with two different statistical approach for inspection of the effect of inputs which are %Nb, %Ti and %B, general factorial regression and neuro-regression, which is the combination of machine learning and general linear model in a specialized way as mentioned in section 1.3.3.

3.4 Preliminary Modeling Studies

It has been a target of this study to construct a formulization for explanation of the phenomena of the mechanical outputs of inoculation element such as Nb, Ti and B on

A356 alloy. To achieve this, general factorial regression approach was used by the DoE outputs, which are each sample's tensile test result on Minitab 20 platform. For general linear model, fundamental model that is given on Formula (18) was processed on Minitab 20 [79].

$$Y=X\beta+\varepsilon \quad (18)$$

Which Y term is called vector of responses, X as design matrix, β as vector of parameters and ε as vector of independent normal random variables.

General linear model was constructed on YS, TS, %E and QI individually, to make a relevant model of phenomena. Mean value of 2 cast specimen's tensile test results was used for preparing a model, which is 10 tensile test results for individual composition with different cooling rates, just like has been observed on aluminum wheel production range. Totally, 270 tensile test results were processed.

General linear model calculations are given in Figure 3.10 to Figure 3.13 with Analysis of Variance and R^2 values. The model was run considering single, double and triple interactions of Nb, Ti and B input data. Backward elimination method was used to simplify the model by removing statistically insignificant inputs from the regression equation. The α value was taken as 0.1, for backward elimination.

Analysis of Variance

Source	DF	Adj SS	Adj MS	F-Value	P-Value
Nb ppm	1	85,80	85,803	3,52	0,067
Ti ppm	1	73,14	73,136	3,00	0,090
B ppm	1	500,34	500,342	20,53	0,000
Nb ppm*Ti ppm	1	145,78	145,780	5,98	0,018
Error	49	1194,48	24,377		
Lack-of-Fit	22	971,10	44,141	5,34	0,000
Pure Error	27	223,38	8,273		
Total	53	1849,73			

Model Summary

S	R-sq	R-sq(adj)	R-sq(pred)
4,93732	35,42%	30,15%	23,39%

Figure 3.10: ANOVA and R^2 values of YS data.

As it can be seen from Figure 3.10, R^2 adjusted (adj) value was obtained as 30,15%, which is not proper value for model's consistency. P-value table indicated that B and Nb*Ti interaction inputs were only significantly affect the YS result with the value

lower than 0.05% which is model's confidence interval. On formula (19), regression equation for YS model is given.

$$YS = 182{,}67 + 0{,}00309\ Nb\ ppm + 0{,}00285\ Ti\ ppm + 0{,}004142\ B\ ppm - 0{,}000003\ Nb\ ppm*Ti\ ppm \quad (19)$$

Analysis of Variance

Source	DF	Adj SS	Adj MS	F-Value	P-Value
Ti ppm	1	34,88	34,88	2,19	0,146
B ppm	1	80,68	80,68	5,05	0,029
Ti ppm*B ppm	1	87,36	87,36	5,47	0,023
Error	50	798,06	15,96		
Lack-of-Fit	23	480,94	20,91	1,78	0,076
Pure Error	27	317,12	11,75		
Total	53	901,46			

Model Summary

S	R-sq	R-sq(adj)	R-sq(pred)
3,99515	11,47%	6,16%	0,00%

Figure 3.11: ANOVA and R2 values of TS data.

Based on Figure 3.11, it can be observed that adjusted R^2 value of 11,47%, which does not demonstrate adequate consistency for the TS model, just like YS model. The p-value table suggests that the significant impacts on the TS outcome are solely from B and the interaction between Ti and B. Nb was not added to model due to non-significancy. The regression equation for the YS model is provided in formula (20).

$$TS = 251{,}26 + 0{,}00197\ Ti\ ppm + 0{,}00299\ B\ ppm - 0{,}000002\ Ti\ ppm*B\ ppm \quad (20)$$

Analysis of Variance

Source	DF	Adj SS	Adj MS	F-Value	P-Value
Nb ppm	1	2,856	2,85586	1,70	0,198
Ti ppm	1	0,003	0,00293	0,00	0,967
B ppm	1	4,626	4,62582	2,76	0,103
Nb ppm*Ti ppm	1	5,453	5,45307	3,25	0,078
Ti ppm*B ppm	1	5,229	5,22853	3,12	0,084
Error	48	80,555	1,67823		
Lack-of-Fit	21	63,014	3,00065	4,62	0,000
Pure Error	27	17,541	0,64967		
Total	53	144,657			

Model Summary

S	R-sq	R-sq(adj)	R-sq(pred)
1,29546	44,31%	38,51%	27,55%

Figure 3.12: ANOVA and R2 values of %E data.

Figure 3.12 reveals an adjusted R^2 value of 44,31%, which, like the TS and YS model, does not provide satisfactory consistency for the %E model although the higher R^2 value. Formula (20) presents the regression equation for the YS model.

$$\%E = 6{,}833 - 0{,}000563\ \text{Nb ppm} - 0{,}000023\ \text{Ti ppm} - 0{,}000717\ \text{B ppm} + 0{,}000001\ \text{Nb ppm*Ti ppm} - 0{,}000001\ \text{Ti ppm*B ppm} \quad (21)$$

Analysis of Variance

Source	DF	Adj SS	Adj MS	F-Value	P-Value
Ti ppm	1	825,2	825,17	2,63	0,111
B ppm	1	76,7	76,69	0,24	0,623
Ti ppm*B ppm	1	1583,1	1583,08	5,04	0,029
Error	50	15699,0	313,98		
Lack-of-Fit	23	10317,8	448,60	2,25	0,022
Pure Error	27	5381,2	199,30		
Total	53	23017,2			

Model Summary

S	R-sq	R-sq(adj)	R-sq(pred)
17,7195	31,79%	27,70%	17,84%

Figure 3.13: ANOVA and R2 values of QI data.

As depicted in Figure 3.13, the QI model, much like the previous models, displays an unsatisfactory consistency with an adjusted R^2 value of 11.47%. The p-value table suggests that only Ti*B interaction significantly impact the QI outcome. Due to its non-significance, Nb has been omitted from the model. The regression equation for the YS model is presented in formula (21).

$$QI = 360{,}51 + 0{,}00958\ \text{Ti ppm} - 0{,}00292\ \text{B ppm} - 0{,}000010\ \text{Ti ppm*B ppm} \quad (22)$$

3.4.1 Response Optimization

Even though the model consistency is enormously low with low R^2 values, response optimization tool was used on Minitab 20 to visualize the model's selection as proper composition for desired scenario for outputs which is given on Table 3.2. These selected compositions were used for metallurgical analysis, even if there is no statistically correct optimization data. At least, metal quality of these two compositions which are belonged to "all maximized" and "all minimized" scenarios are statistically different from each other, by applying Tukey Comparison, it was revealed. It will be given on this section at Figure 3.16.

Table 3.2: Optimization Table of General Factorial Regression Model of Study.

Optimization Name	**YS**	**TS**	**%E**	**QI** *(TS+150*log(%E))*
All maximized	Maximize	Maximize	Maximize	Maximize
All minimized	Minimize	Minimize	Minimize	Minimize

As it depicted on Figure 3.14, maximized scenario was found as 2000 ppm Nb, 2000 ppm Ti and 200 ppm B as a result of general factorial regression. R25 was selected. Overall desirability value indicates that subgroup's target value can be achieved with a probability of 35.31%. Therefore, final target of each output with a desirability value of; YS = 183.20 MPa, 21.42%, TS = 254 MPa, 55.31%, %E = 7.64%, %16.28 and QI = 375 MPa, 80.60, respectively. This overall desirability value gave us a thought about the reliability of model, which is poor enough to describe the whole grain refining phenomena.

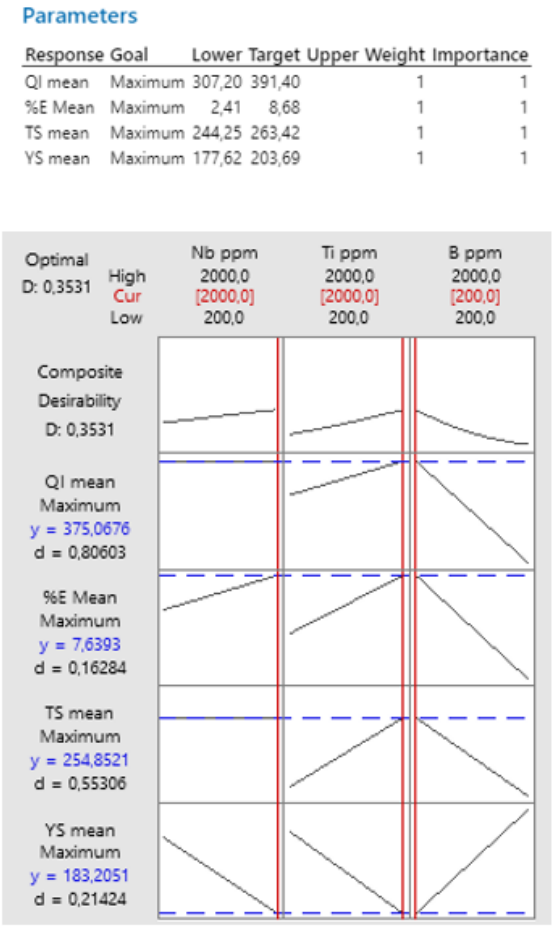

Figure 3.14: Response optimization of maximized outputs of YS, TS, %E and QI.

Figure 3.15 showcases the maximized scenario derived from the general factorial regression, which is represented by 2000 ppm Nb, 2000 ppm Ti, and 2000 ppm B. R27 was selected. The overall desirability value signifies a 61.85% probability of achieving the target value for each subgroup, which is a higher probability value than "all maximized" scenario. Thus, the final target for each output, with their corresponding desirability values, is as follows: YS = 190.66 MPa with 49.97%, TS = 251.76 MPa with 60.81%, %E = 4.27% with 70.26%, and QI = 333.71 MPa at 68.50%. Even though higher desirability value of this scenario, due to low R^2 values final model is not reliable at all with same concerns just like previous one.

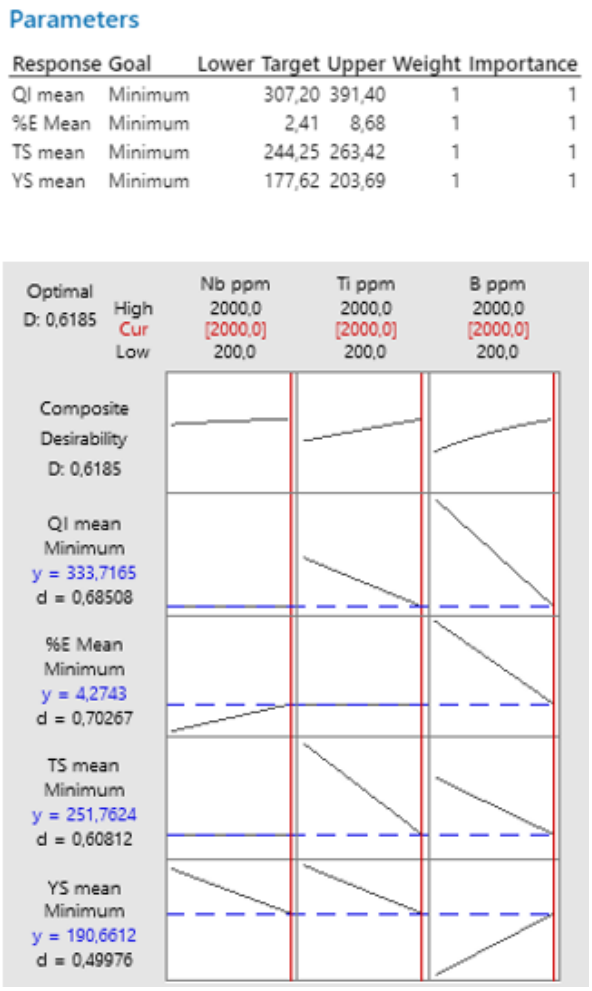

Figure 3.15: Response optimization of minimized outputs of YS, TS, %E and QI.

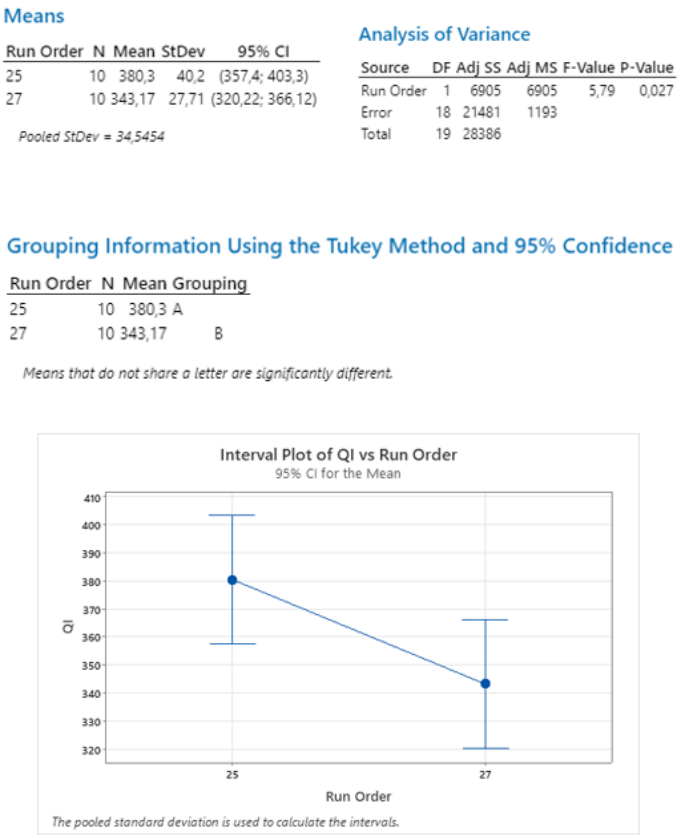

Figure 3.16: Tukey Comparison table of R25 (minimized scenario) and R27 (maximized scenario).

3.5 Modified Modeling Approaches

As it was proposed on previous section, general factorial regression was not capable to explain curtain phenomena about grain refinement effect of different Nb-Ti-B ratios which was given as standard DoE inspection tool on Minitab 20. Therefore, it was seen that unreliable optimization equations are far away from the use due to low R^2 values. So that, new approach for determining a new optimization function was needed, which was mentioned in section 1.3.3, neuro-regression approach.

During the model development phase, a hybrid method that merges the strengths of ANN and multiple nonlinear regression analysis is deployed to boost the capacity for precise fitting. Initially, the experimental data is randomly divided into two parts: 80% is used for training and the remaining 20% for testing. The primary goal in the training phase is to lessen the difference between the experimental and forecasted values by tweaking the regression models. Following that, the testing phase is executed, aiming to enhance precision by diminishing the impact of deviations in the regression models.

3.5.1 Optimization Algorithms

From a mathematical standpoint, optimization can be defined as the process of finding the best possible solution by minimizing or maximizing the objective function(s), subject to equality or inequality constraints. While considering traditional and non-traditional optimization methods, stochastic optimization algorithms, which rely on probabilistic elements and do not require derivative information to discover the global optimum, are better suited to handle complex engineering problems. Moreover, stochastic optimization algorithms can generate superior solutions in relatively short computation times. In this study, the stochastic search algorithms were employed like DE, NM, RS, and SA to identify the optimal parameters of the machining process[70].

3.5.1.1 Differential evolution algorithm

The Differential Evolution (DE) algorithm, a component of stochastic optimization algorithms, employs a population-based strategy to address nonlinear optimization issues in continuous domains. Currently, DE is acknowledged as a highly effective algorithm for handling real-parameter optimization problems. Similar to the genetic algorithm, the DE algorithm functions via four fundamental stages: selection, crossover, mutation, and initialization. Three precise control parameters guide the algorithm's operation: (a) the mutation/differentiation constant, (b) the crossover constant, and (c) the population size. Fundamentally, the DE algorithm utilizes the principle of manipulating target vectors and difference vectors to generate a trial vector, which is subsequently compared with the target vector. Additional control parameters crucial to the algorithm include (a) the problem dimension, which determines the complexity of the optimization scenario, (b) the maximum number of generations, which acts as a termination criterion, and (c) boundary constraints.[70].

3.5.1.2 Nelder-Mead algorithm

The Nelder-Mead (NM) algorithm is a method free from derivatives and typically applied to solve unconstrained optimization problems. It is often leveraged to tackle statistical issues and perform parameter estimations. This algorithm operates on the basis of comparing functions. The search process begins by establishing an initial simplex, a geometric form in n-dimensions possessing non-zero volume. This shape is

a convex hull comprising n+1 vertices of a polytope in an n-dimensional space. The central procedures of the NM algorithm consist of ordering, reflecting, expanding, contracting, and shrinking. Within the NM algorithm, a polytope is formed by n+1 points as x1, x2, . . . , x_{n+1}. Following this, these points are arranged in a specific order.

$$f(x_1) \leq f(x_2) < \ldots < f(x_{n+1}), \tag{23}$$

In this scenario, f (x1), f (x2), …, f (xn+1) are the functional output values. The newly generated points replace the previous worst ones if they prove to be superior. At this point, a trial point, denoted as x_t, is formed by reflecting the worst point through the centroid, labeled as c, of the polytope, $\frac{1}{n}\sum_{i=1}^{n} x_i$

$$x_t = c + a(c - x_{n+1}) \tag{24}$$

In this instance, a is greater than 0. If the new trial point x_t becomes a new worst point or a new best point, such that f (x_1) ≤ f (x_t) ≤ f (x_n), x_t takes the place of x_{n+1}. However, if the newly generated point surpasses the current best point, the reflection is deemed successful, and the process can be expanded further, as shown:

$$x_e = c + \beta(x_1 - r) \tag{25}$$

Where β is the expansion factor, implying that a β > 1 will expand the polytope. If the expansion is successful, i.e., f (x_e) < f (x_t), x_e replaces x_{n+1}. However, if the expansion fails, x_t takes the place of x_{n+1}. If the newly generated point x_t is worst than x_n, i.e., f (x_t) ≥ f (x_n), then it's assumed that the polytope is too large and requires contraction. In this instance, a new trial point is calculated as follows:

$$\Delta Gv = \Delta H - T\Delta S \tag{26}$$

$$x_c = \begin{cases} c + \gamma(x_{n+1} + c) iff(x_1) \geq f(x_{n+1}) \\ c + \gamma(x_t - c) iff(x_t) < f(x_{n+1}) \end{cases}$$

In this case, γ is a parameter that falls within the range of 0 and 1. If f (x_c) is less than the minimum of f (x_{n+1}) and f (x_t), the contraction is considered successful, and x_c replaces x_{n+1}. If not, further contraction is carried out. Convergence is determined

when the difference between the best functional values at the new and old points falls below the established tolerances[70].

3.5.1.3 Simulated annealing algorithm.

The Simulated Annealing (SA) algorithm, a renowned and widely used optimization algorithm, derives its principles from the annealing process, a metallurgical heat-treatment method. The annealing process involves heating a material and controlling its cooling to enhance its crystal size and reduce defect, resulting in lower energy states. This process has significant influence over temperature and Gibbs energy, the thermodynamic free energy.

In the realm of optimization, the SA algorithm employs a random search as per the Markov chain, permitting value shifts to enhance the objective function solution while retaining some suboptimal modifications. With every iteration, a fresh point is randomly established, and the algorithm halts when any of the method's stopping criteria are met. The discrepancy between the new and current points is computed via the Boltzmann probability distribution, which is scaled relative to the temperature. The Boltzmann probability distribution can be articulated as follows:

$$P(E) = e^{-\frac{E}{kT}} \tag{27}$$

In this expression, P€ signifies the likelihood of reaching energy level €, while 'k' represents the Boltzmann constant, and 'T' corresponds to the temperature.

3.5.1.4 Random search algorithm

The Random Search (RS) algorithm is a widely recognized direct search method known for its easy adaptability to complex problems. The success of this method largely depends on the number of iterations performed. Starting from an initial point or a set of points, the RS algorithm conducts iterative searches of random points, moving to superior positions within the search space until it locates the global optimum or optima. This method is capable of finding the optimum solution for large-scale problems, including those with non-differentiable, nonconvex objective functions in discrete, continuous, or mixed domains. A thorough discussion on the solution capability of the RS algorithm can be found in the existing literature [70].

3.5.2 Problem Definition

By using same data obtained from DoE set, Nb, Ti and B addition values in terms of "ppm" was selected as input parameters. 10 tensile test data mean for each 27 DoE set was used with 4 sub-groups which are YS, TS, %E and QI, called output data. Investigation of data were processed on Mathematica. Initially, an exhaustive examination was carried out on several nonlinear neuro-regression analyses. These included linear, trigonometric, logarithmic, quadratic forms, and their rational equivalents, all applied to %Nb, %Ti and %B content. Secondly, the performance indicators for every potential model are assessed individually to determine their suitability for inclusion in the optimization stage. However, obtaining a practical mathematical function that bypasses stability isn't often beneficial. Therefore, to overcome this challenge, the optimization process is conducted with functions that yield values strictly within the engineering constraints, ensuring the stability of each potential model. Lastly, employing the adjusted versions of four unique techniques – differential evaluation (DE), Nelder-Mead (NM), random search (RS), and simulated annealing (SA) algorithms, effect of Nb, Ti and B on grain refining performance in terms of mechanical test performance and their corresponding optimum values for given scenarios in Table 3.4 was given.

On Table 3.3, first two scenarios were processed for observing max. and min. mechanical potentials of system. Last one was belong to required mechanical performance limits for commercial aluminum alloy wheel production, to indicate optimum addition limits of Nb, Ti and B for high-quality OEM car manufacturer.

Table 3.3: Optimization Scenario List For Neuro-Regression Approach

Opt. Scenario Process No.	**YS**	**TS**	**%E**	**QI** *(TS+150*log(%E))*
1	Maximize	Maximize	Maximize	Maximize
2	Minimize	Minimize	Minimize	Minimize
3	≥180 MPa	≥240 MPa	≥4%	≥330 MPa

Table 3.4: Overview of output parameter's performed mathematical models.

Outputs	Mathematical Model
YS	Abs[-5.35016 – 25.9473 Cos[x1] – 19.7813 Cos[x1]^2 -1.02406 Cos[x1]^3 – 9.93509 Cos[x2] – 20.1166 Cos[x1] Cos[x2] – 6.28785 Cos[x1]^2 Cos[x2] – 24.6627 Cos[x2]^2 – 7.6177 Cos[x1] Cos[x2]^2 – 1.48838 Cos[x2]^3 – 7.67809 Cos[x3] – 32.9984 Cos[x1] Cos[x3] – 8.59409 Cos[x1]^2 Cos[x3] – 14.5027 Cos[x2] Cos[x3] + 37.2902 Cos[x1] Cos[x2] Cos[x3] – 2.8435 Cos[x2]^2 Cos[x3] – 17.4973 Cos[x3]^2 -11.5595 Cos[x1] Cos[x3]^2 – 6.65254 Cos[x2] Cos[x3]^2 – 1.99983 Cos[x3]^3 + 15.6287 Sin[x1] + 26.9635 Cos[x1] Sin[x1] + 1.77642 Cos[x1]^2 Sin[x1] + 2.68889 Cos[x2] Sin[x1] + 8.90536 Cos[x1] Cos[x2] Sin[x1] – 7.45892 Cos[x2]^2 Sin[x1] + 5.52471 Cos[x3] Sin[x1] – 7.88002 Cos[x1] Cos[x3] Sin[x1] + 21.0348 Cos[x2] Cos[x3] Sin[x1] + 4.53358 Cos[x3]^2 Sin[x1] – 25.7853 Sin[x1]^2 – 12.1323 Cos[x1] Sin[x1]^2 – 8.44619 Cos[x2] Sin[x1]^2 – 1.40171 Cos[x3] Sin[x1]^2 + 2.12617 Sin[x1]^3 – 38.6221 Sin[x2] + 5.29688 Cos[x1] Sin[x2] – 11.8904 Cos[x1]^2 Sin[x2] – 17.2922 Cos[x2] Sin[x2] + 29.4331 Cos[x1] Cos[x2] Sin[x2] – 15.4786 Cos[x2]^2 Sin[x2] – 33.3463 Cos[x3] Sin[x2] + 71.0943 Cos[x1] Cos[x3] Sin[x2] – 4.68841 Cos[x2] Cos[x3] Sin[x2] – 12.9026 Cos[x3]^2 Sin[x2] – 102.473 Sin[x1] Sin[x2] + 27.5587 Cos[x1] Sin[x1] Sin[x2] – 61.1449 Cos[x2] Sin[x1] Sin[x2] + 31.5953 Cos[x3] Sin[x1] Sin[x2] – 28.6416 Sin[x1]^2 Sin[x2] – 20.0688 Sin[x2]^2 – 18.2418 Cos[x1] Sin[x2]^2 + 5.79517 Cos[x2] Sin[x2]^2 – 5.14953 Cos[x3] Sin[x2]^2 + 14.5497 Sin[x1] Sin[x2]^2 – 2.8216 Sin[x2]^3 – 11.878 Sin[x3] – 83.8366 Cos[x1] Sin[x3] – 17.366 Cos[x1]^2 Sin[x3] – 16.6195 Cos[x2] Sin[x3] + 78.5786 Cos[x1] Cos[x2] Sin[x3] – 7.18371 Cos[x2]^2 Sin[x3] + 16.6553 Cos[x3] Sin[x3] – 14.8678 Cos[x1] Cos[x3] Sin[x3] + 3.81949 Cos[x2] Cos[x3] Sin[x3] – 4.00031 Cos[x3]^2 Sin[x3] – 25.9475 Sin[x1] Sin[x3] – 44.1181 Cos[x1] Sin[x1] Sin[x3] + 38.4158 Cos[x2] Sin[x1] Sin[x3] – 29.1808 Cos[x3] Sin[x1] Sin[x3] + 3.79309 Sin[x1]^2 Sin[x3] – 30.2967 Sin[x2] Sin[x3] + 174.95 Cos[x1] Sin[x2] Sin[x3] + 0.190601 Cos[x2] Sin[x2] Sin[x3] + 27.6462 Cos[x3] Sin[x2] Sin[x3] + 79.5059 Sin[x1] Sin[x2] Sin[x3] – 6.10233 Sin[x2]^2 Sin[x3] – 26.9218 Sin[x3]^2 – 8.16572 Cos[x1] Sin[x3]^2 – 6.56577 Cos[x2] Sin[x3]^2 – 2.63474 Cos[x3] Sin[x3]^2 + 11.9405 Sin[x1] Sin[x3]^2 – 27.6573 Sin[x2] Sin[x3]^2 – 1.09294 Sin[x3]^3]
TS	Abs[-6.96522 – 33.695 Cos[x1] – 25.5444 Cos[x1]^2 – 1.50263 Cos[x1]^3 – 13.5815 Cos[x2] – 26.1026 Cos[x1] Cos[x2] – 7.57218 Cos[x1]^2 Cos[x2] – 32.1061 Cos[x2]^2 – 9.57976 Cos[x1] Cos[x2]^2 – 2.12944 Cos[x2]^3 – 11.5717 Cos[x3] – 44.1504 Cos[x1] Cos[x3] – 10.9433 Cos[x1]^2 Cos[x3] – 15.6617 Cos[x2] Cos[x3] + 39.4039 Cos[x1] Cos[x2] Cos[x3] – 4.39713 Cos[x2]^2 Cos[x3] – 22.7332 Cos[x3]^2 – 15.8581 Cos[x1] Cos[x3]^2 – 7.48052 Cos[x2] Cos[x3]^2 – 2.36075 Cos[x3]^3 + 20.3916 Sin[x1] + 36.6459 Cos[x1] Sin[x1] + 1.84661 Cos[x1]^2 Sin[x1] + 6.71218 Cos[x2] Sin[x1] + 12.4198

	Cos[x1] Cos[x2] Sin[x1] – 8.56186 Cos[x2]^2 Sin[x1] + 6.14286 Cos[x3] Sin[x1] – 8.80814 Cos[x1] Cos[x3] Sin[x1] + 23.5098 Cos[x2] Cos[x3] Sin[x1] + 4.68988 Cos[x3]^2 Sin[x1] – 34.3084 Sin[x1]^2 - 15.6966 Cos[x1] Sin[x1]^2 – 10.965 Cos[x2] Sin[x1]^2 – 3.17301 Cos[x3] Sin[x1]^2 + 2.6147 Sin[x1]^3 – 51.4708 Sin[x2] + 6.16417 Cos[x1] Sin[x2] – 16.014 Cos[x1]^2 Sin[x2] – 23.0075 Cos[x2] Sin[x2] + 39.0651 Cos[x1] Cos[x2] Sin[x2] – 19.8343 Cos[x2]^2 Sin[x2] – 47.9536 Cos[x3] Sin[x2] + 92.9144 Cos[x1] Cos[x3] Sin[x2] – 4.12903 Cos[x2] Cos[x3] Sin[x2] – 17.4611 Cos[x3]^2 Sin[x2] – 143.771 Sin[x1] Sin[x2] + 34.8326 Cos[x1] Sin[x1] Sin[x2] – 82.4488 Cos[x2] Sin[x1] Sin[x2] + 48.4475 Cos[x3] Sin[x1] Sin[x2] – 37.3953 Sin[x1]^2 Sin[x2] – 26.8267 Sin[x2]^2 – 23.9856 Cos[x1] Sin[x2]^2 + 7.66348 Cos[x2] Sin[x2]^2 – 7.42861 Cos[x3] Sin[x2]^2 + 20.3739 Sin[x1] Sin[x2]^2 – 3.78606 Sin[x2]^3 – 15.0263 Sin[x3] – 108.614 Cos[x1] Sin[x3] – 22.2241 Cos[x1]^2 Sin[x3] – 17.975 Cos[x2] Sin[x3] + 94.9501 Cos[x1] Cos[x2] Sin[x3] – 8.33892 Cos[x2]^2 Sin[x3] + 25.2324 Cos[x3] Sin[x3] – 19.0204 Cos[x1] Cos[x3] Sin[x3] + 8.7627 Cos[x2] Cos[x3] Sin[x3] – 5.35917 Cos[x3]^2 Sin[x3] – 35.1431 Sin[x1] Sin[x3] – 59.981 Cos[x1] Sin[x1] Sin[x3] + 45.7222 Cos[x2] Sin[x1] Sin[x3] – 40.6997 Cos[x3] Sin[x1] Sin[x3] + 5.54903 Sin[x1]^2 Sin[x3] – 38.8132 Sin[x2] Sin[x3] + 229.754 Cos[x1] Sin[x2] Sin[x3] + 1.49325 Cos[x2] Sin[x2] Sin[x3] + 36.3503 Cos[x3] Sin[x2] Sin[x3] + 107.782 Sin[x1] Sin[x2] Sin[x3] – 8.15512 Sin[x2]^2 Sin[x3] – 35.938 Sin[x3]^2 – 11.6602 Cos[x1] Sin[x3]^2 – 9.51064 Cos[x2] Sin[x3]^2 – 3.18656 Cos[x3] Sin[x3]^2 + 16.5212 Sin[x1] Sin[x3]^2 – 35.881 Sin[x2] Sin[x3]^2 – 1.29246 Sin[x3]^3]
%E	Abs[-0.333993 + 0.149839 Cos[x1] + 0.360169 Cos[x1]^2 – 0.353419 Cos[x1]^3 + 0.632965 Cos[x2] + 0.158369 Cos[x1] Cos[x2] + 0.607323 Cos[x1]^2 Cos[x2] – 0.261003 Cos[x2]^2 + 0.656082 Cos[x1] Cos[x2]^2 + 0.407704 Cos[x2]^3 + 0.660279 Cos[x3] + 0.129399 Cos[x1] Cos[x3] – 0.520848 Cos[x1]^2 Cos[x3] – 3.53077 Cos[x2] Cos[x3] – 1.09748 Cos[x1] Cos[x2] Cos[x3] – 0.833871 Cos[x2]^2 Cos[x3] – 0.970899 Cos[x3]^2 + 0.308371 Cos[x1] Cos[x3]^2 – 0.892301 Cos[x2] Cos[x3]^2 + 0.0938719 Cos[x3]^3 – 0.362809 Sin[x1] + 1.22667 Cos[x1] Sin[x1] – 0.86649 Cos[x1]^2 Sin[x1] + 1.89838 Cos[x2] Sin[x1] + 0.499898 Cos[x1] Cos[x2] Sin[x1] + 1.05632 Cos[x2]^2 Sin[x1] – 1.14224 Cos[x3] Sin[x1] – 1.00076 Cos[x1] Cos[x3] Sin[x1] + 1.94168 Cos[x2] Cos[x3] Sin[x1] + 0.352518 Cos[x3]^2 Sin[x1] – 0.389672 Sin[x1]^2 + 0.400941 Cos[x1] Sin[x1]^2 + 0.270968 Cos[x2] Sin[x1]^2 + 0.460707 Cos[x3] Sin[x1]^2 + 0.211364 Sin[x1]^3 – 0.368524 Sin[x2] – 0.218658 Cos[x1] Sin[x2] + 0.871781 Cos[x1]^2 Sin[x2] + 2.164 Cos[x2] Sin[x2] – 0.379221 Cos[x1] Cos[x2] Sin[x2] – 0.331516 Cos[x2]^2 Sin[x2] – 1.65499 Cos[x3] Sin[x2] – 0.807103 Cos[x1] Cos[x3] Sin[x2] – 1.87838 Cos[x2] Cos[x3] Sin[x2] – 0.861159 Cos[x3]^2 Sin[x2] – 2.31157 Sin[x1] Sin[x2] – 2.24646 Cos[x1] Sin[x1] Sin[x2] – 2.41408 Cos[x2] Sin[x1] Sin[x2] – 1.01871 Cos[x3] Sin[x1] Sin[x2] – 0.940056 Sin[x1]^2 Sin[x2] – 1.27936 Sin[x2]^2 – 0.0224519 Cos[x1] Sin[x2]^2 – 0.609835 Cos[x2] Sin[x2]^2 + 0.862437 Cos[x3] Sin[x2]^2 – 0.361395 Sin[x1] Sin[x2]^2

	+ 0.0951617 Sin[x2]^3 + 0.879018 Sin[x3] + 1.19046 Cos[x1] Sin[x3] + 0.763987 Cos[x1]^2 Sin[x3] + 0.529333 Cos[x2] Sin[x3] – 0.435286 Cos[x1] Cos[x2] Sin[x3] + 0.57358 Cos[x2]^2 Sin[x3] – 0.0365567 Cos[x3] Sin[x3] + 0.311461 Cos[x1] Cos[x3] Sin[x3] – 0.653328 Cos[x2] Cos[x3] Sin[x3] + 0.849864 Cos[x3]^2 Sin[x3] + 1.24986 Sin[x1] Sin[x3] – 2.86194 Cos[x1] Sin[x1] Sin[x3] + 0.937084 Cos[x2] Sin[x1] Sin[x3] – 2.16312 Cos[x3] Sin[x1] Sin[x3] + 0.943458 Sin[x1]^2 Sin[x3] + 0.0752856 Sin[x2] Sin[x3] – 1.10009 Cos[x1] Sin[x2] Sin[x3] – 0.301485 Cos[x2] Sin[x2] Sin[x3] + 0.127414 Cos[x3] Sin[x2] Sin[x3] – 3.70528 Sin[x1] Sin[x2] Sin[x3] + 1.23583 Sin[x2]^2 Sin[x3] – 1.22483 Sin[x3]^2 – 1.20493 Cos[x1] Sin[x3]^2 – 0.821519 Cos[x2] Sin[x3]^2 – 1.40507 Cos[x3] Sin[x3]^2 – 0.791931 Sin[x1] Sin[x3]^2 + 0.525136 Sin[x2] Sin[x3]^2 – 0.25233 Sin[x3]^3]
QI	Abs[-11.1013 – 23.5401 Cos[x1] – 42.4091 Cos[x1]^2 – 3.60968 Cos[x1]^3 – 49.7714 Cos[x2] – 29.7279 Cos[x1] Cos[x2] – 11.0667 Cos[x1]^2 Cos[x2] – 44.5871 Cos[x2]^2 – 10.4113 Cos[x1] Cos[x2]^2 – 2.89641 Cos[x2]^3 – 23.1074 Cos[x3] – 38.3351 Cos[x1] Cos[x3] – 13.8027 Cos[x1]^2 Cos[x3] – 65.7319 Cos[x2] Cos[x3] + 29.6632 Cos[x1] Cos[x2] Cos[x3] – 13.2101 Cos[x2]^2 Cos[x3] – 28.917 Cos[x3]^2 – 9.92259 Cos[x1] Cos[x3]^2 – 24.8084 Cos[x2] Cos[x3]^2 – 1.14681 Cos[x3]^3 – 43.484 Sin[x1] + 42.8081 Cos[x1] Sin[x1] – 17.5424 Cos[x1]^2 Sin[x1] + 37.8814 Cos[x2] Sin[x1] + 70.2558 Cos[x1] Cos[x2] Sin[x1] – 5.71506 Cos[x2]^2 Sin[x1] – 69.1351 Cos[x3] Sin[x1] – 11.4236 Cos[x1] Cos[x3] Sin[x1] + 119.682 Cos[x2] Cos[x3] Sin[x1] – 27.2536 Cos[x3]^2 Sin[x1] – 62.0052 Sin[x1]^2 + 2.23241 Cos[x1] Sin[x1]^2 – 39.1693 Cos[x2] Sin[x1]^2 – 12.5897 Cos[x3] Sin[x1]^2 – 3.51404 Sin[x1]^3 + 4.51597 Sin[x2] – 0.0365167 Cos[x1] Sin[x2] – 4.74968 Cos[x1]^2 Sin[x2] + 45.1852 Cos[x2] Sin[x2] + 9.22884 Cos[x1] Cos[x2] Sin[x2] – 7.19238 Cos[x2]^2 Sin[x2] – 1.26713 Cos[x3] Sin[x2] + 1.92984 Cos[x1] Cos[x3] Sin[x2] – 13.6594 Cos[x2] Cos[x3] Sin[x2] + 4.09524 Cos[x3]^2 Sin[x2] – 73.618 Sin[x1] Sin[x2] – 47.9743 Cos[x1] Sin[x1] Sin[x2] + 68.4659 Cos[x2] Sin[x1] Sin[x2] – 17.2628 Cos[x3] Sin[x1] Sin[x2] + 10.3583 Sin[x1]^2 Sin[x2] – 60.0089 Sin[x2]^2 – 18.5424 Cos[x1] Sin[x2]^2 – 17.0434 Cos[x2] Sin[x2]^2 – 9.21384 Cos[x3] Sin[x2]^2 – 37.5726 Sin[x1] Sin[x2]^2 + 1.55518 Sin[x2]^3 + 4.21259 Sin[x3] – 4.57013 Cos[x1] Sin[x3] – 8.45983 Cos[x1]^2 Sin[x3] – 105.594 Cos[x2] Sin[x3] + 78.6118 Cos[x1] Cos[x2] Sin[x3] – 9.90469 Cos[x2]^2 Sin[x3] + 119.083 Cos[x3] Sin[x3] + 4.449 Cos[x1] Cos[x3] Sin[x3] – 6.26177 Cos[x2] Cos[x3] Sin[x3] + 3.47001 Cos[x3]^2 Sin[x3] – 130.863 Sin[x1] Sin[x3] – 64.4082 Cos[x1] Sin[x1] Sin[x3] + 216.359 Cos[x2] Sin[x1] Sin[x3] – 30.642 Cos[x3] Sin[x1] Sin[x3] + 18.0125 Sin[x1]^2 Sin[x3] + 81.0902 Sin[x2] Sin[x3] – 29.0911 Cos[x1] Sin[x2] Sin[x3] – 59.243 Cos[x2] Sin[x2] Sin[x3] + 13.5888 Cos[x3] Sin[x2] Sin[x3] – 67.6642 Sin[x1] Sin[x2] Sin[x3] + 17.9718 Sin[x2]^2 Sin[x3] – 72.8786 Sin[x3]^2 – 15.4979 Cos[x1] Sin[x3]^2 – 26.747 Cos[x2] Sin[x3]^2 – 8.39002 Cos[x3] Sin[x3]^2 – 16.7833 Sin[x1] Sin[x3]^2 + 1.85336 Sin[x2] Sin[x3]^2 + 1.20802 Sin[x3]^3]

Table 3.5: R^2 Results of mathematical models for each output.

Outputs	R^2 Training	R^2 Testing
YS	0,999	0,999
TS	0,999	0,999
%E	0,999	0,999
QI	0,999	0,999

The expectation for all the models is to achieve a coefficient of determination, R2, greater than 0.95. These mathematical models are chosen based on related parameters observed in a preliminary study, where it was found that these models yield the highest R^2 values and more accurately depict the relationship between response and actual data compared to other models. For neuro-regression, all the reference data is divided, with 80% designated for training and 20% for testing, and this division is done randomly. Afterward, the adjusted R^2 is computed to perform a meaningful test, and values for R^2 training and R^2 testing are calculated utilizing Wolfram Mathematica. It was seen that as it was indicated on Table 3.5, all mathematical models explain the exact grain refining phenomena based on given inputs. It was clearly demonstrated that neuro-regression approach has given better results beside general factorial regression for related phenomena.

3.5.3 Optimization

Optimization results that were performed on Mathematica based on the optimization formulas mentioned in Table 3.4 were given in Table 3.6. The optimization table demonstrates the effects of Nb, Ti, and B elements on the yield strength (YS), tensile strength (TS), elongation (%E), and quality index (QI) of a master alloy across three scenarios. In the first scenario, an attempt was made to maximize all the properties (YS, TS, %E, and QI). Nb was found to be optimally present at 1723.08 ppm, Ti at 836.885 ppm, and B at 1061.19 ppm. As a result, a yield strength of 270.482 MPa, a tensile strength of 369.356 MPa, elongation of 9.33396%, and a quality index of 436.49 MPa were achieved.

The second scenario involved minimizing all properties. The optimal presence of Nb was found to be at 1759.32 ppm, Ti at 989.568 ppm, and B at 788.532 ppm. The

properties were observed to be significantly lower in this scenario, with a yield strength of 3.31826 MPa, tensile strength of 0.00111 MPa, elongation of 5.48945%, and a quality index of 5.34881 MPa. These values are not that realistic, even though the model itself has an ability to forecast unseen data from dataset by using randomly selected train data. Additional iteration is needed for model to modify output boundary condition to converge realistic tensile test data of the castings. The third scenario required the output properties to meet or exceed certain levels (YS ≥180 MPa, TS ≥240 MPa, %E ≥4%, QI≥ 330 MPa). The concentrations that were determined to be optimal were Nb at 944 ppm, Ti at 975 ppm, and B at 458 ppm. This led to a yield strength of 272.642 MPa, tensile strength of 371.665 MPa, elongation of 9.16009%, and a quality index of 427.4 MPa being achieved.

At the end, for 3 optimization scenario, iteration studies are beneficial to apply to converge real time results of tensile test values. Since that step of the work may be called as preliminary study, there are plenty of rooms and opportunities for enhancement of the model with feedbacked tensile test data.

Table 3.6: Optimization Results of Neuro-Regression for Given Scenarios.

Opt. Scenario Process No.	**Output Targets**	**Optimum Input Parameters and Output Results**	
1	**YS**=Maximize, **TS**=Maximize, **%E**=Maximize, **QI**=Maximize	**Nb ppm** = 1723.08 **Ti ppm**= 836.885 **B ppm**= 1061.19	**YS**= 270.482 MPa **TS**= 369.356 MPa **%E**= 9.33396 **QI**= 436.49 MPa
2	**YS**=Minimize, **TS**= Minimize, **%E**= Minimize, **QI**= Minimize	**Nb ppm** = 1759.32 **Ti ppm**= 989.568 **B ppm**= 788.532	**YS**= 3.31826 MPa **TS**= 0.00111 MPa **%E**= 5.48945 **QI**= 5.34881 MPa
3	**YS**= ≥180 MPa, **TS**= ≥240 MPa,	**Nb ppm** = 944 **Ti ppm**= 975	**YS**= 272.642 MPa **TS**= 371.665 MPa

%E=≥4%,	**B ppm**= 458	**%E**= 9.16009
QI=≥330 MPa		**QI**= 427.4 MPa

3.6 Microstructure Examination

In this chapter, microstructure properties of selected samples R25 and R27 will be given.

3.6.1 Grain Size Examination

Macro grain size examination is a remarkable examination method for determining the grain refinement performance of related inoculants. In Figure 3.17, grain size measurement example was depicted. 5 horizontal and 5 vertical grid was drawn on image total length was divided to counted grain numbers based on color difference of grains thanks to etching method. Measurement ruler that placed on right hand side has 0.5 mm equidistance grids as reference. In table 3.7, macrostructure of DoE set will be given.

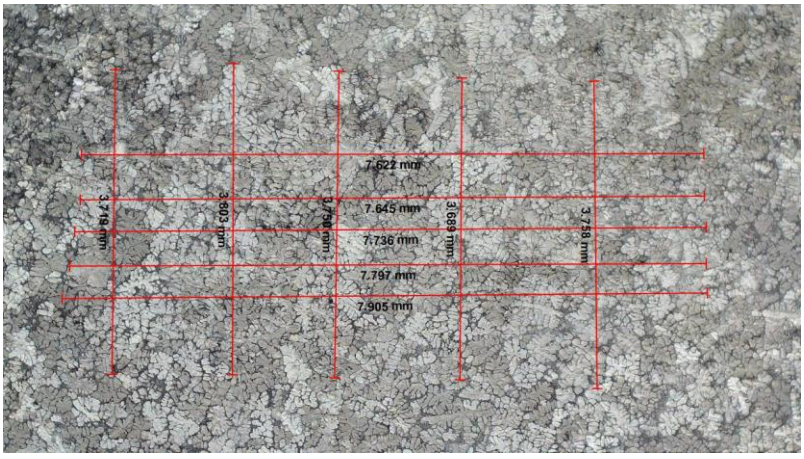

Figure 3.17: Grain size measurement example.

Table 3.7: Macrostructure Images of whole DoE set specimens.

1 	2 	3 
4 	5 	6 
7 	8 	9 
10 	11 	12 
13 	14 	15 
16 	17 	18 

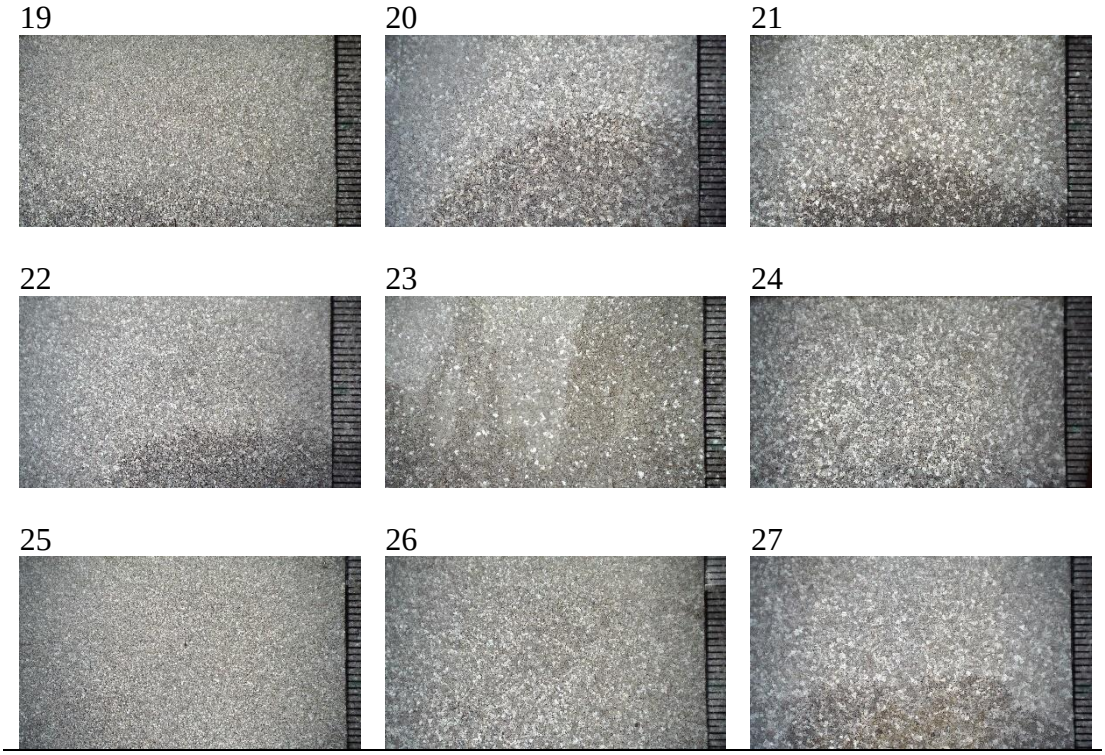

All grain size measurements are given in additionally on Table 3.8. According to data, minimum grain size was observed on R16. Maximum one was obtained from R10. These data reveals that overall grain refinement performance of whole DoE set was excellent. These data will be used on further studies to enhance optimization.

Table 3.8: Grain size measurement table of DoE set.

Run Order No.	**Grain Size Mean (µm)**	**Run Order No.**	**Grain Size Mean (µm)**
1	147,8471	**15**	139,6066
2	134,7896	**16**	120,1284
3	148,7658	**17**	173,7208
4	124,7173	**18**	172,6699
5	120,6076	**19**	127,6125

6	127,4437	**20**	161,3603
7	125,8420	**21**	163,2338
8	182,679	**22**	133,6533
9	155,9585	**23**	143,4864
10	215,6929	**24**	164,6294
11	163,9743	**25**	124,567
12	152,8955	**26**	144,6933
13	125,9147	**27**	151,5928
14	173,8025		

3.6.2 Optical Image Examination

In Figure 3.18, 3 different zoomed optical microscope images of R25 were given on 50x, 100x and 200x, respectively. On Figure 3.18a, equiaxed grains can be seen due to constitutional undercooling due to concentration difference between liquid zone and solidified zone with the contributions of inoculants that was observed on XRD analysis. Thanks to globular dendrite zone, slip resistance of matrix was enhanced with increased surface area of grain surfaces. Additionally, at the center of dendrites, inoculant intermetallic particles can be seen on Figure 3.18c. It was validated that solidification sequence was triggered with in-situ created intermetallic phases such as niobium borides, niobium aluminides, titanium aluminides, titanium borides and aluminum borides. On the other hand, eutectic modification was performed excellent, as expected on inoculation step by adding same amount of Sr to every DoE set to reduce the mechanical result deviation that caused by lack of eutectic modification.

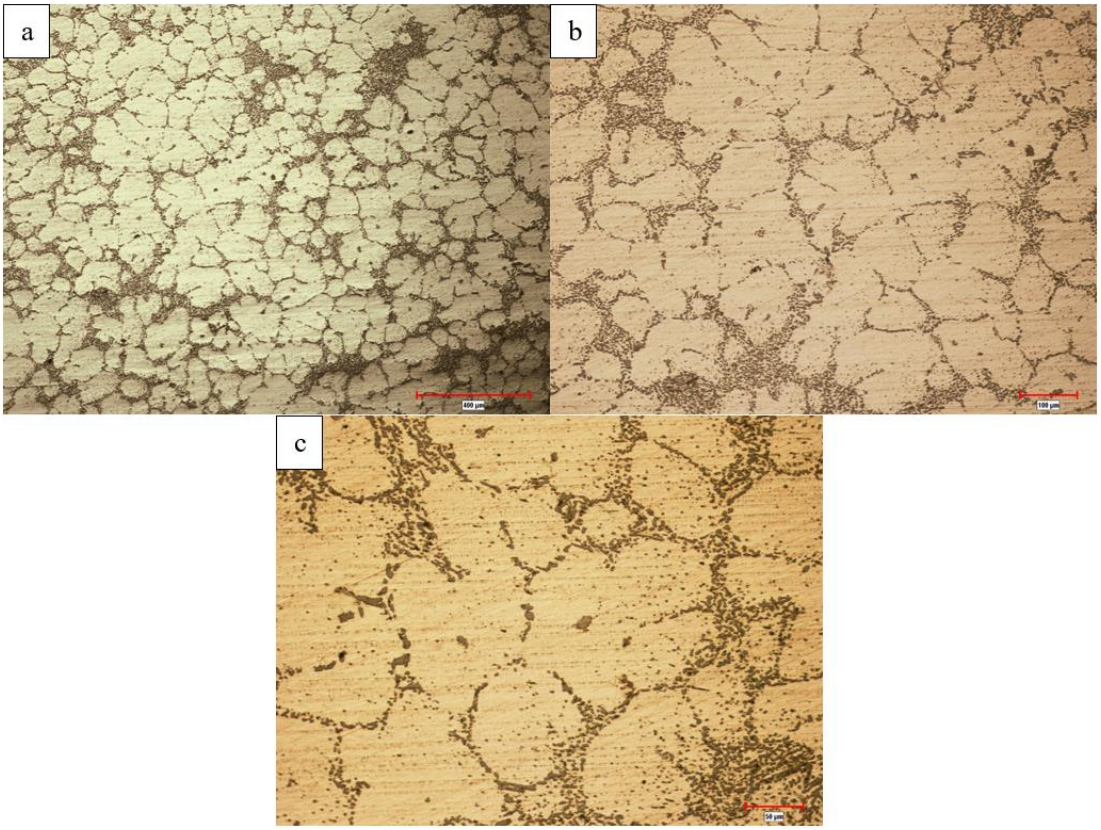

Figure 3.18: (a) 50x, (b) 100x and (c) 200x optical microscopy images of R25 sample.

In Figure 3.19, 3 different zoomed optical microscope images of R27 were given on 50x, 100x and 200x, respectively. On Figure 3.19a, global dendrite structure barely seen due to acicular unmodified eutectic Si phase. Eutectic modification performance was decreased since the only difference between R25 and R27 is 800 ppm more B addition to R27, B atoms may have interacted with Sr to form SrB_6 particulates. Thus, free-Sr density may be reduced that performs eutectic Si modification by interacting with Al on eutectic Si surface then stops the growth of Si by twinning mechanism on the lattice structure. On the other hand, “dispersed black dots” can be seen on polished surface clearly on Figure 3.19c. This may be caused by external inclusions that was contaminated from degassing rotor or crucible itself, Fe-Al intermetallics or Mg_2Si agglomeration which both of them may be caused mechanical performance reduction. Additionally, possible boride-aluminide formation was observed on microstructure as bulky shaped brown prisms and thin needles.

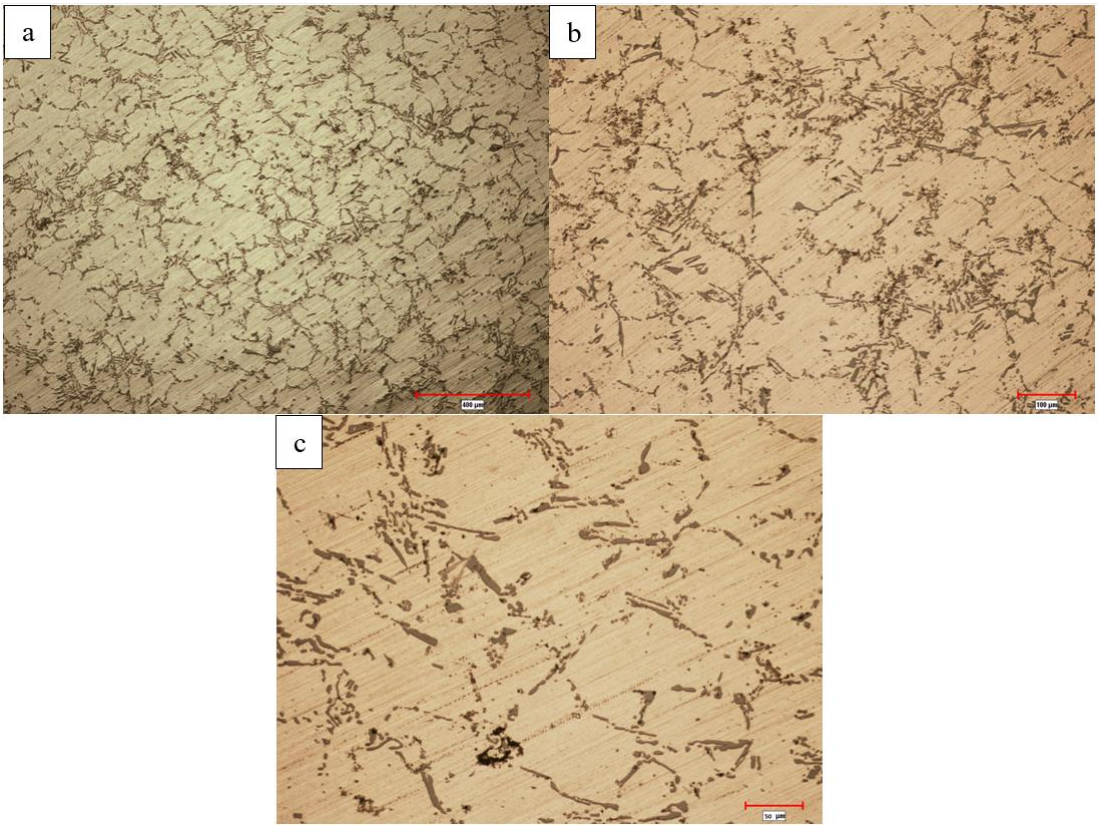

Figure 3.19: (a) 50x, (b) 100x and (c) 200x optical microscopy images of R27 sample.

3.6.3 SEM Examination

On the SEM method, main focus was the observation on in-situ created compounds, especially aluminides and borides that consists of Nb and Ti. Especially for surface scan of the process, Secondary Electron mode (SE) was used for the distinguishing of intermetallic nucleant particles from the Al-matrix. On the Figure 3.20, blocky hexagonal shaped structure can be seen on below of the image of R25 specimen. At the upper left hand-side, agglomerated particles were observed.

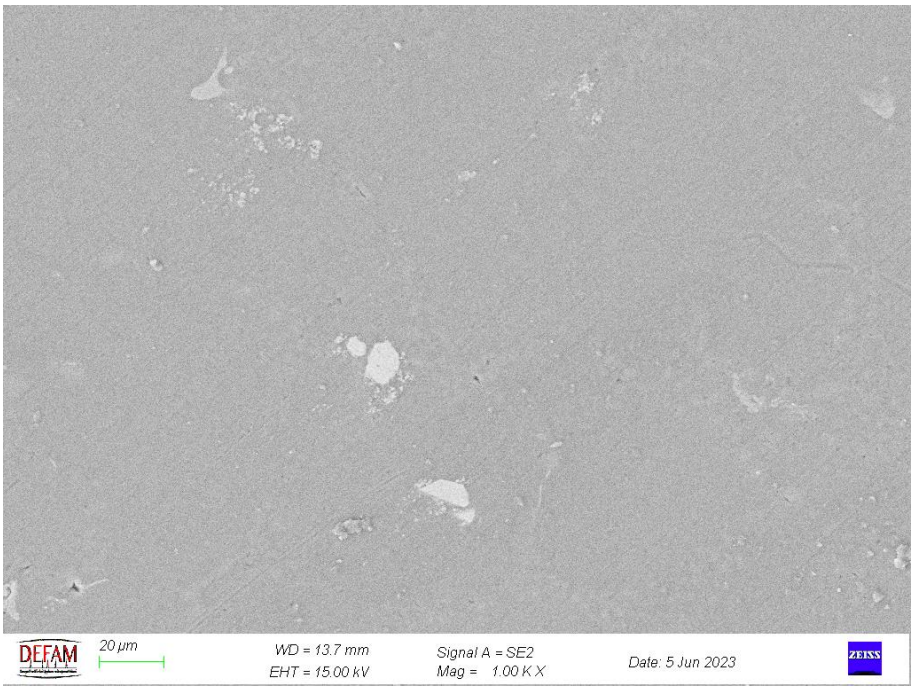

Figure 3.20: SEM Image of R25 on 1000X Magnification with SE mode.

In order to investigate the particles in more of detail in terms of chemical composition, EDS analysis was done as detailly described on Chapter 2. As 3 blocky shaped particles was investigated with EDS method, it was revealed that 3 different analyses almost exactly gave same results. $Al_3(Nb,Ti)$ system was observed, as it depicted in Figure 3.21. Since it has been knowing that the matrix is Al-Si alloy, EDS results of selected area on matrix was not indicated in Figure 3.21.

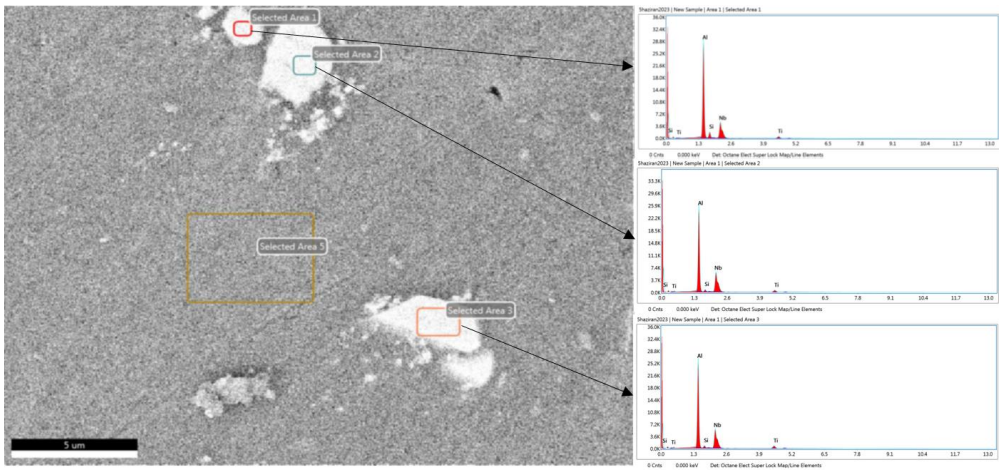

Figure 3.21: EDS Analysis of R25 Sample.

Besides relatively bigger particles that depicted in Figure 3.21, nano-sized particles was imaged on 3000X on SE mode on R25 specimen, where it should have containing

2000 ppm Nb, 2000 ppm Ti and 200 ppm B, based on target values. It was seen that nano-sized particles were agglomerated around the bulky shaped ones. Since Li et. al was proposed in his study, $Al_3(Nb,Ti)$ (<15µm) and $(Nb,Ti)B_2$ (<1µm) particles can be observed in the cluster form due to lack of shear force and convection that produced by mechanical stirring, which was applied on this study on rotary degassing application [66].

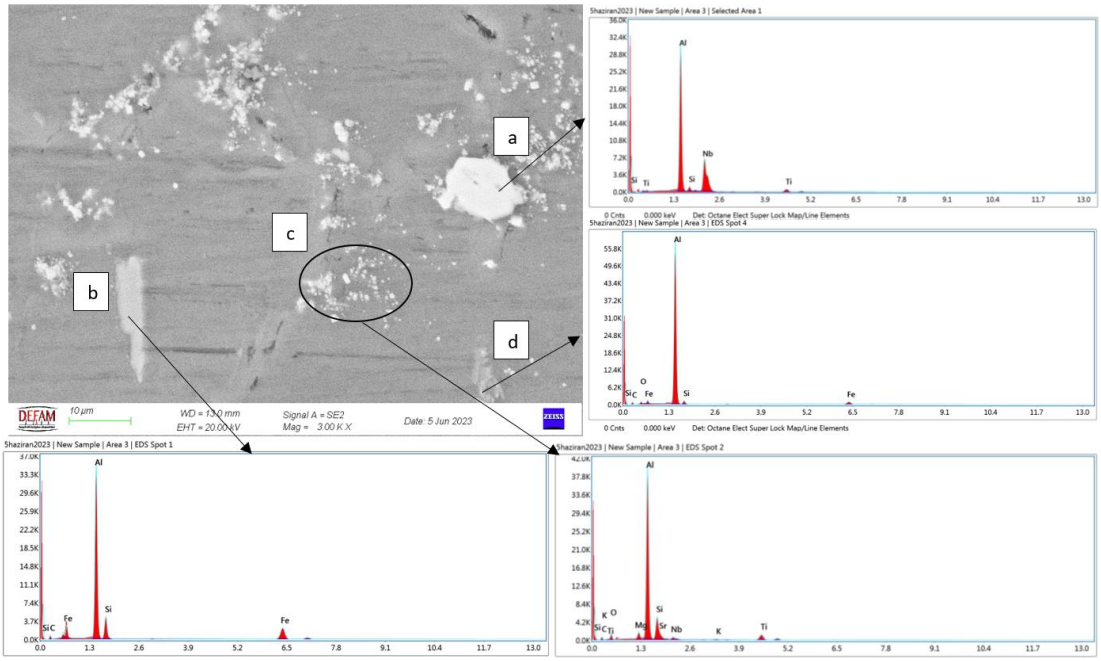

Figure 3.22: EDS Analysis of the R25 Sample, where (a) Al3(Nb,Ti), (b) acicular AlFeSi , (c) mixed particle cluster and (d) Eutectic Si.

On the Figure 3.22a, polygonal Al3(Nb,Ti) intermetallic particle was found again, at the center area of the dendrite, where nucleation sites occurs on the liquidus to solidus+liquidus zone around the surface of particle. Acicular, needle-like β-AlFeSi phase was observed on Figure 3.22b, which deteriorates mechanical proterties of material by creating high-stress zones on the small-radii tips of compound whenever alloy have got loaded with external force. On Figure 3.22c, some of additional peaks were observed such as Mg and Sr, which can be called as main alloying element of A356 alloy. Particles with relatively small radii may be clustered on the matrix with the help of the driving force of diffusion on the step of T6 heat treatment's solutionizing section. Figure 3.22d showed that FeO included eutectic Si was able to form on matrix.

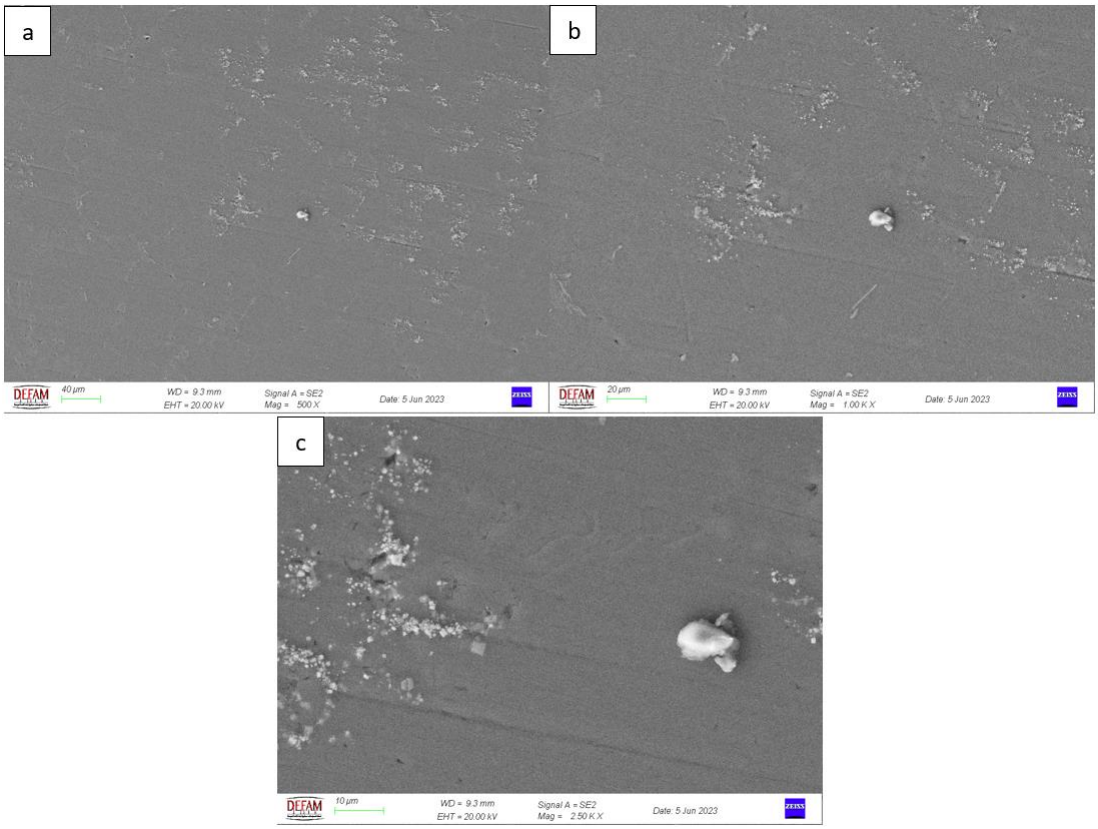

Figure 3.23: SEM Image of R27 on (a)500X, (b) 1000X and (c) 2500X Magnification with SE mode.

On the Figure 3.23, 3 different secondary electron microscope image was taken from R27 specimen, which was performed much worse on tensile test results than R25 specimen, on 500X,1000X and 2500X magnifications, respectively. As seen in Figure 3.23a, the in-situ formed phases agglomerated in the eutectic region as small particles. Focusing on Figure 3.23c, it is seen that the particle sizes are smaller than 1 micron and around the eutectic region. The large light-colored particle seen prominently over this area was not subjected to EDS analysis as it was observed that it did not belong to the matrix. It was classified as a foreign material retained on the surface during metallographic surface preparation and excluded from the analysis.

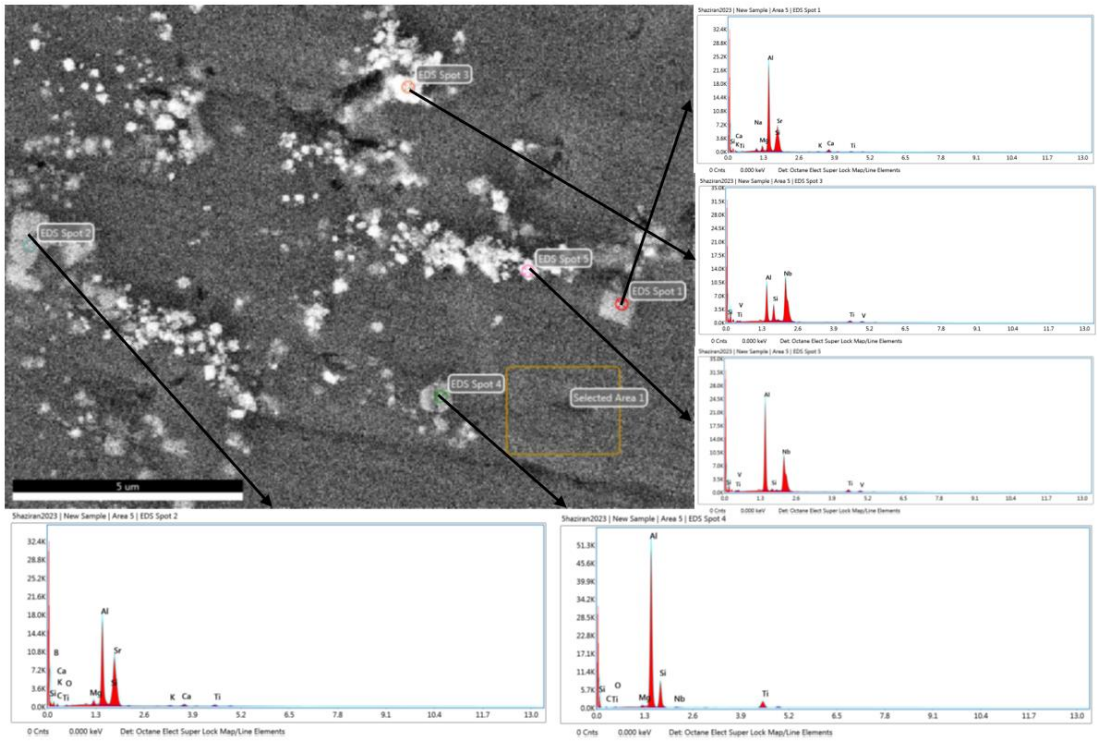

Figure 3.24: EDS Analysis of R27 Sample.

Focusing on the region seen in Figure 3.23c as seen in Figure 3.24, it is seen that the tetrahedral bulky particles seen in spot 1 and spot 2 are the AlSr intermetallic phase. It is also possible that the phase observed in spot 2 is SrB_6. The B element released by the increased B element in R27 may have interacted with Sr. In addition, alkaline elements such as Ca, K, Na and Mg are also present in the phase. Although the poor performance of the eutectic modification seen in Figure 3.19 is not fully explained by this analysis, it is possible that the growth of this phase formed by Al-Sr interaction and the twinning that should occur during the growth of eutectic Si did not occur and the eutectic phases could not be refined. In future studies, the relationship between this effect and the B element should be studied because the only specific difference between the R25 and R27 phases is a B element difference of 800 ppm, theoretically. In spot 3 and spot 5, the Al3Nb phase was predominantly observed. In contrast to R25, no Ti element was found in niobium aluminides. In spot 4, the Al3Ti intermetallic phase was observed and trace amounts of Nb and Mg were found to be present in solid solution in the phase.

In Figure 3.25, the EDS mapping maps of samples R25 (a) and R27 (b) are extracted elementwise. The most significant difference is in the eutectic modification

performance, even though the same amount of the eutectic modifier Sr was used, as mentioned earlier. Unlike R25, which has a refined eutectic structure, R27 exhibits coarse and needle-like eutectic Si. Regarding the B element, B is homogeneously distributed in the structure in (a); however, in (b), clustered B elements are observed. Increasing free B elements in R27 react with other intermetallics to form new phases. Titanium boride particles formed as a result of peritectic transformation around the surface of niobium boride as revealed by Li et al. are clearly observed in (a) [66]. In the R25 sample with high grain refinement performance, it was observed that the Ti element exhibited a homogeneous distribution in the solid solution. On the contrary, the presence of Ti intercalated and agglomerated with Nb and Ti in sample R27, which could not be taken into solid solution and was present as an intermetallic compound between the grain boundaries, reduced the mechanical strength of the alloy and thus the grain refinement efficiency. Since it was revealed by Xu et. al, only the largest nucleants on an agglomerated particle zone triggers the nucleation of Al-dendrites rather than small and distributed ones [80].

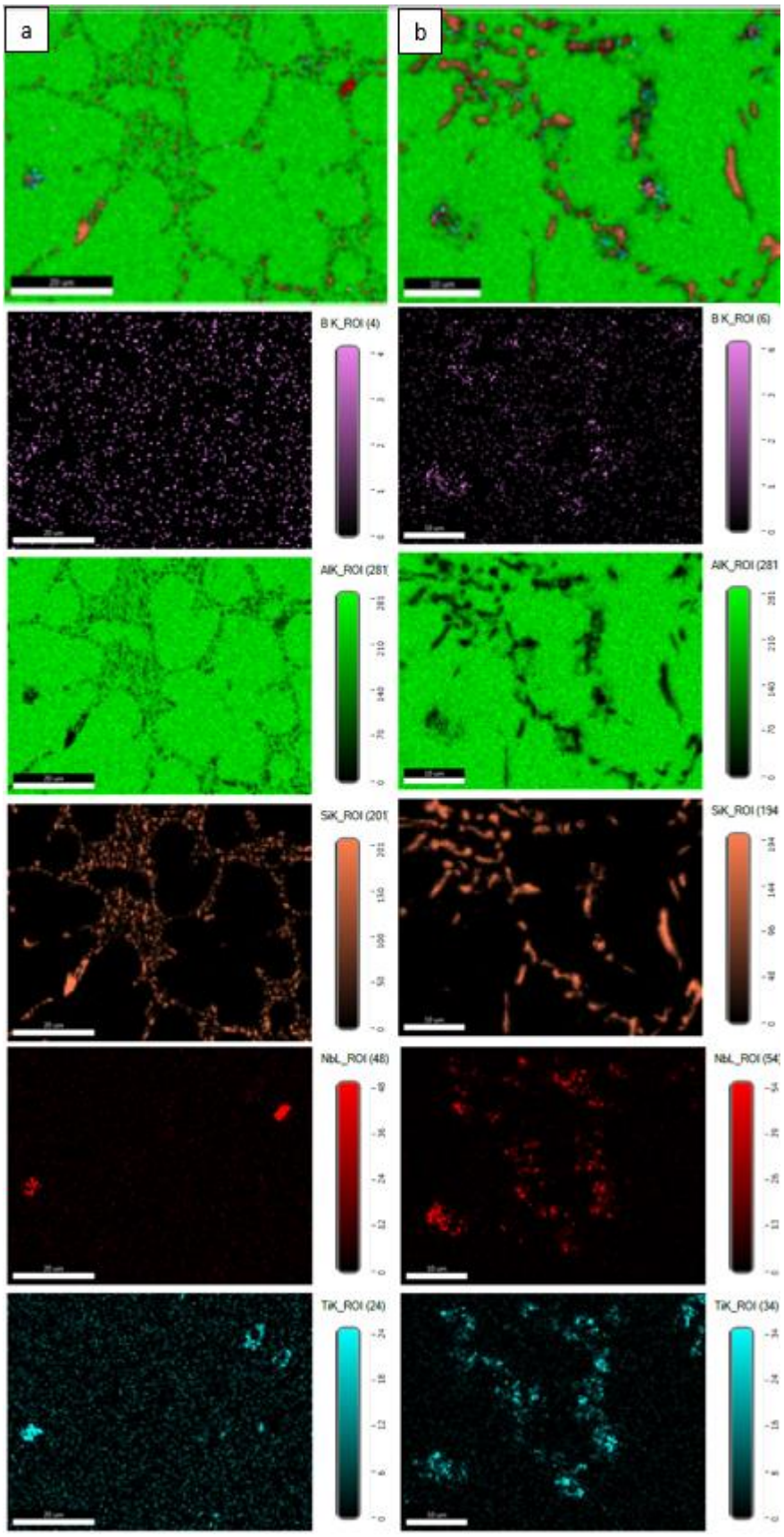

Figure 3.25: EDS Mapping of (a) R25 and (b) R27 samples in terms of the content and distribution of Al, Si, Nb, Ti and B.

Chapter 4

Conclusion

The tensile test results were processed using general factorial regression as preliminary model in Minitab 20 and then neuro-regression approach were performed in Mathematica, an innovative data processing technique combining machine learning and regression analysis, right after obtaining such a weak data fitting performance on the preliminary model. Neuro-regression yielded an R2 value of 0.99 for all optimization outputs, whereas general factorial regression yielded an R2 value of less than 0.40 on average, which did not adequately explain the phenomenon. According to the optimization data, the elemental inputs required for the first scenario, maximum material properties, are 1723.08, 836.885 and 1061.19 in ppm for Nb, Ti and B, respectively. In the second scenario, which is the worst-case scenario, these values are 1759.32, 989.568 and 788.532 respectively. In scenario 3, where A356, a wheel alloy, is given mechanical properties by OEM customers as an engineering design output, the required alloy inputs are 944, 975 and 458 for Nb, Ti and B, respectively. The most significant throughput of the final model is the capability to predict unknown tensile test data which the 20% of the whole data by randomly selected training data that corresponds %80 of tensile results thanks to neuro-regression approach. Nevertheless, output tensile data of optimization scenarios are needed to get iterated by determined composition input by neuro-regression based model, to converge the model to the real-time tensile test results.

The analyses performed on R25 and R27, which were selected as sample specimens in the characterization stages, showed that the most obvious difference between R25 and R27 specimens is the decrease in the eutectic modification performance of the R27 specimen containing 1800 ppm more B, thus coarsened eutectic Si is observed in the microstructure. On the other hand, the difference in the distribution of Ti in the solid solution observed by EDS Mapping, despite the fact that both samples contain the

same amount of Ti, may have revealed this difference in mechanical strength. The lattice mismatch between the Al-Matrix and the nucleant obtained with Ti observed on the surface of Nb aluminide, which is published in recent studies in the literature, has been reduced, increasing the grain refinement effectiveness. The theoretical values were also found by examining the mechanical strength output.

The planned future steps of this study are as follows,

- Generating new samples using the data obtained from the optimization as input with an iterative approach and adding the results to the model,
- Inclusion of the solidification rate of A356 alloy and the grain size of the alloy as inputs to the model and increasing model consistency and
- The usage of the outputs of the final optimization model on the production of aluminum alloy wheels and a validation study is designed with the tensile results obtained from the wheel itself.

References

[1] H. Kvande, “Occurrence and Production of Aluminum,” *Encyclopedia of Inorganic and Bioinorganic Chemistry*, pp. 1–10, Dec. 2015, doi: 10.1002/9781119951438.EIBC2350.

[2] “Introduction and Uses of Lightweight Materials,” *Lightweight Materials*, pp. 1–31, Oct. 2012, doi: 10.31399/ASM.TB.LMUB.T53550001.

[3] V. Semenovich. Zolotorevskiĭ, N. A. Belov, and M. V. Glazoff, “Casting aluminum alloys,” p. 530, 2007.

[4] G. K. Sigworth, “Fundamentals of Solidification in Aluminum Castings,” *International Journal of Metalcasting*, vol. 8, no. 1, pp. 7–20, 2014, doi: 10.1007/BF03355567.

[5] W. M. Jiang, Z. T. Fan, and D. J. Liu, “Microstructure, tensile properties and fractography of A356 alloy under as-cast and T6 obtained with expendable pattern shell casting process,” *Transactions of Nonferrous Metals Society of China (English Edition)*, vol. 22, no. SUPPL. 1, Oct. 2012, doi: 10.1016/S1003-6326(12)61676-8.

[6] D. Eduard, “International Alloy Designations and Chemical Composition Limits for Wrought Aluminum and Wrought Aluminum Alloys With Support for On-line Access From: Aluminum Extruders Council.” Accessed: Apr. 05, 2023. [Online]. Available: https://www.academia.edu/40558842/International_Alloy_Designations_and_Chemical_Composition_Limits_for_Wrought_Aluminum_and_Wrought_Aluminum_Alloys_With_Support_for_On_line_Access_From_Aluminum_Extruders_Council

[7] A. M. A. Mohamed and F. H. Samuel, “A Review on the Heat Treatment of Al-Si-Cu/Mg Casting Alloys,” *Heat Treatment - Conventional and Novel Applications*, Sep. 2012, doi: 10.5772/50282.

[8] K. Gall, N. Yang, M. Horstemeyer, D. L. McDowell, and J. Fan, “The influence of modified intermetallics and Si particles on fatigue crack paths in a cast A356 Al alloy,” *Fatigue Fract Eng Mater Struct*, vol. 23, no. 2, pp. 159–172, Feb. 2000, doi: 10.1046/J.1460-2695.2000.00239.X.

[9] F. A. Davis and T. S. Eyre, “The effect of silicon content and morphology on the wear of aluminium-silicon alloys under dry and lubricated sliding conditions,” *Tribol Int*, vol. 27, no. 3, pp. 171–181, Jun. 1994, doi: 10.1016/0301-679X(94)90042-6.

[10] M. F. Ibrahim, E. M. Elgallad, S. Valtierra, H. W. Doty, and F. H. Samuel, “Metallurgical Parameters Controlling the Eutectic Silicon Charateristics in Be-Treated Al-Si-Mg Alloys,” *Materials*, vol. 9, no. 2, 2016, doi: 10.3390/MA9020078.

[11] Taylor and J. A., “The effect of iron in Al-Si casting alloys,” *35th Australian Foundry Institute National Conference*, pp. 148–157, Jan. 2004.

[12] C. H. Caceres, C. J. Davidson, J. R. Griffiths, and Q. G. Wang, “The effect of Mg on the microstructure and mechanical behavior of Al-Si-Mg casting alloys,” *Metall Mater Trans A Phys Metall Mater Sci*, vol. 30, no. 10, pp. 2611–2618, 1999, doi: 10.1007/S11661-999-0301-8/METRICS.

[13] Q. G. Wang and C. J. Davidson, “Solidification and precipitation behaviour of Al-Si-Mg casting alloys,” *J Mater Sci*, vol. 36, no. 3, pp. 739–750, 2001, doi: 10.1023/A:1004801327556/METRICS.

[14] B. S. Murty, S. A. Kori, and M. Chakraborty, “Grain refinement of aluminium and its alloys by heterogeneous nucleation and alloying,” *http://dx.doi.org/10.1179/095066001225001049*, vol. 47, no. 1, pp. 3–29, 2013, doi: 10.1179/095066001225001049.

[15] E. Ghassemali, M. Riestra, T. Bogdanoff, B. S. Kumar, and S. Seifeddine, “Hall-Petch equation in a hypoeutectic Al-Si cast alloy: grain size vs. secondary dendrite arm spacing,” *Procedia Eng*, vol. 207, pp. 19–24, Jan. 2017, doi: 10.1016/J.PROENG.2017.10.731.

[16] S. J. Lloyd, “Effects of a Niobium-Boron grain refiner on undercooling and microstructural evolution of aluminium silicon alloys,” 2016, Accessed: Apr. 12, 2023. [Online]. Available: http://bura.brunel.ac.uk/handle/2438/15155

[17] Z. Fan and H. Men, “Heterogeneous Nucleation and Grain Initiation on a Single Substrate,” *Metals 2022, Vol. 12, Page 1454*, vol. 12, no. 9, p. 1454, Aug. 2022, doi: 10.3390/MET12091454.

[18] “A. Cibula: J. Inst. Metals, 76 (1949-1950), 321-360 - Google Akademik.” https://scholar.google.com/scholar?hl=tr&as_sdt=0%2C5&q=A.+Cibula%3A+J.+Inst.+Metals%2C+76+%281949-1950%29%2C+321-360&btnG= (accessed Apr. 12, 2023).

[19] A. L. Greer, A. M. Bunn, A. Tronche, P. V. Evans, and D. J. Bristow, “Modelling of inoculation of metallic melts: application to grain refinement of aluminium by Al-Ti-B,” *AcMat*, vol. 48, no. 11, pp. 2823–2835, Jun. 2000, doi: 10.1016/S1359-6454(00)00094-X.

[20] L. F. Mondolfo, “Aluminum–Magnesium, Aluminum–Manganese Alloys,” *Aluminum Alloys*, pp. 806–841, Jan. 1976, doi: 10.1016/B978-0-408-70932-3.50404-6.

[21] G. K. Sigworth, “The Grain Refining of Aluminum and Phase Relationships in the Al-Ti-B System,” *Metallurgical Transactions A*, vol. 15, no. 2, pp. 277–282, Feb. 1984, doi: 10.1007/BF02645112/METRICS.

[22] X. Wang, “The formation of AlB2 in an Al–B master alloy,” *J Alloys Compd*, vol. 403, no. 1–2, pp. 283–287, Nov. 2005, doi: 10.1016/J.JALLCOM.2005.04.204.

[23] P. S. Mohanty and J. E. Gruzleski, “Grain refinement mechanisms of hypoeutectic Al-Si alloys,” *Acta Mater.*, vol. 44, no. 9, pp. 3749–60, 1996, doi: 10.1016/1359-6454(96)00021-3.

[24] M. Easton and D. Stjohn, “Grain refinement of aluminum alloys: Part I. The nucleant and solute paradigms - a review of the literature,” *Metall Mater Trans A Phys Metall Mater Sci*, vol. 30, no. 6, pp. 1613–1623, 1999, doi: 10.1007/S11661-999-0098-5/METRICS.

[25] J. A. M. Antonio and L. F. M. Lfo, “Grain refinement in aluminum alloyed with titanium and boron,” *Metallurgical Transactions*, vol. 2, no. 2, pp. 465–471, Feb. 1971, doi: 10.1007/BF02663335.

[26] M. Johnsson and L. Backerud, “Nucleants in grain refined aluminium after addition of Ti- and B-containing master alloys,” *Zeitschrift fuer Metallkunde/Materials Research and Advanced Techniques*, vol. 83, no. 11, pp. 774–780, Nov. 1992, doi: 10.1515/IJMR-1992-831102/MACHINEREADABLECITATION/RIS.

[27] G. P. Jones and J. Pearson, “Factors affecting the grain-refinement of aluminum using titanium and boron additives,” *Metallurgical Transactions B*, vol. 7, no. 2, pp. 223–234, Jun. 1976, doi: 10.1007/BF02654921.

[28] I. Maxwell and A. Hellawell, “A simple model for grain refinement during solidification,” *Acta Metallurgica*, vol. 23, no. 2, pp. 229–237, 1975, doi: 10.1016/0001-6160(75)90188-1.

[29] T. E. Quested, A. T. Dinsdale, and A. L. Greer, “Thermodynamic modelling of growth-restriction effects in aluminium alloys,” *Acta Mater*, vol. 53, no. 5, pp. 1323–1334, Mar. 2005, doi: 10.1016/J.ACTAMAT.2004.11.024.

[30] P. Schumacher *et al.*, “New studies of nucleation mechanisms in aluminium alloys: implications for grain refinement practice,” *https://doi.org/10.1179/mst.1998.14.5.394*, vol. 14, no. 5, pp. 394–404, 2013, doi: 10.1179/MST.1998.14.5.394.

[31] R. G. Guan and D. Tie, “A Review on Grain Refinement of Aluminum Alloys: Progresses, Challenges and Prospects,” *Acta Metallurgica Sinica (English Letters) 2017 30:5*, vol. 30, no. 5, pp. 409–432, Mar. 2017, doi: 10.1007/S40195-017-0565-8.

[32] P. Duwez, R. H. Willens, and W. Klement, “Continuous series of metastable solid solutions in silver-copper alloys [19],” *J Appl Phys*, vol. 31, no. 6, pp. 1136–1137, 1960, doi: 10.1063/1.1735777.

[33] T. K. Han, S. J. Kim, Y. S. Yang, A. Inoue, Y. H. Kim, and I. B. Kim, “Nanocrystallization and High Tensile Strength of Amorphous Zr-Al-Ni-Cu-Ag Alloys,” *METALS AND MATERIALS International*, vol. 7, no. 2, pp. 91–94, 2001.

[34] Q. Pan, W. Huang, X. Lin, Y. Z.-J. of crystal growth, and undefined 1997, “Primary spacing selection of Cu□ Mn alloy under laser rapid solidification condition,” *Elsevier*, Accessed: Apr. 17, 2023. [Online]. Available: https://www.sciencedirect.com/science/article/pii/S002202489700273X

[35] J. F. Nie, M. Barnett, S. A. Kori, V. Auradi, B. S. Murty, and M. Chakraborty, “Poisoning and fading mechanism of grain refinement in Al-7Si alloy,” *repository.ias.ac.in*, vol. 29, 2005, Accessed: Apr. 17, 2023. [Online]. Available: http://repository.ias.ac.in/92783/

[36] J. A. Spittle and S. Sadli, “Effect of alloy variables on grain refinement of binary aluminium alloys with Al–Ti–B,” *Materials Science and Technology (United Kingdom)*, vol. 11, no. 6, pp. 533–537, 1995, doi: 10.1179/MST.1995.11.6.533.

[37] S. A. Kori, B. S. Murty, and M. Chakraborty, “Influence of silicon and magnesium on grain refinement in aluminium alloys,” *Materials Science and Technology*, vol. 15, no. 9, pp. 986–992, 1999, doi: 10.1179/026708399101506823.

[38] J. F. Nie, M. Barnett, S. A. Kori, V. Auradi, B. S. Murty, and M. Chakraborty, “Poisoning and fading mechanism of grain refinement in Al-7Si alloy,”

repository.ias.ac.in, vol. 29, 2005, Accessed: Apr. 17, 2023. [Online]. Available: http://repository.ias.ac.in/92783/

[39] C. D. Mayes, D. G. McCartney, and G. J. Tatlock, "Observations on the microstructure and performance of an Al□Ti□C grain-refining master alloy," *Materials Science and Engineering: A*, vol. 188, no. 1–2, pp. 283–290, Nov. 1994, doi: 10.1016/0921-5093(94)90383-2.

[40] Z. Fan, Y. Wang, Y. Zhang, T. Qin, X. Z.-A. Materialia, and undefined 2015, "Grain refining mechanism in the Al/Al–Ti–B system," *Elsevier*, Accessed: Apr. 18, 2023. [Online]. Available: https://www.sciencedirect.com/science/article/pii/S1359645414008192

[41] P. Schumacher, B. M.-J. of non-crystalline solids, and undefined 2003, "TEM investigation of heterogeneous nucleation mechanisms in Al–Si alloys," *Elsevier*, Accessed: Apr. 18, 2023. [Online]. Available: https://www.sciencedirect.com/science/article/pii/S0022309302019920

[42] "The Heterogeneous Nucleation Sequence at the Interface of TiB2 in Al Alloys," *cambridge.org*, Accessed: Apr. 18, 2023. [Online]. Available: https://www.cambridge.org/core/journals/microscopy-and-microanalysis/article/heterogeneous-nucleation-sequence-at-the-interface-of-tib2-in-al-alloys/E6459D59FFB143040E2338DE4762A321

[43] Y. B.-M. S. and Technology and undefined 2012, "Effect of silicon content in grain refining hypoeutectic Al–Si foundry alloys with boron and titanium additions," *Taylor & Francis*, vol. 28, no. 4, pp. 385–389, 2012, doi: 10.1179/1743284711Y.0000000049.

[44] Y. Li *et al.*, "Insight into Si poisoning on grain refinement of Al-Si/Al-5Ti-B system," *Acta Mater*, vol. 187, pp. 51–65, Apr. 2020, doi: 10.1016/J.ACTAMAT.2020.01.039.

[45] M. A. Kearns and P. S. Cooper, "Effects of solutes on grain refinement of selected wrought aluminium alloys,"

https://doi.org/10.1179/mst.1997.13.8.650, vol. 13, no. 8, pp. 650–654, 2013, doi: 10.1179/MST.1997.13.8.650.

[46] C. Limmaneevichitr and W. Eidhed, "Fading mechanism of grain refinement of aluminum–silicon alloy with Al–Ti–B grain refiners," *Materials Science and Engineering: A*, vol. 349, no. 1–2, pp. 197–206, May 2003, doi: 10.1016/S0921-5093(02)00751-7.

[47] "A. Pacz U.S Patent No. 1387900; 1921. - Google Akademik." https://scholar.google.com/scholar?hl=tr&as_sdt=0%2C5&q=A.+Pacz+U.S+Patent+No.+1387900%3B+1921.&btnG= (accessed Apr. 18, 2023).

[48] "Gruzleski E, Closset Bm (1990) The Treatment Of Liquid... - Google Akademik." https://scholar.google.com/scholar?hl=tr&as_sdt=0%2C5&q=Gruzleski+E%2C+Closset+Bm+%281990%29+The+Treatment+Of+Liquid+Al%E2%80%93Si+Alloys.+Afs+Inc.%2C+Des+Plaines%2C+Il%2C+Pp+1%E2%80%9368%2C+95%E2%80%93157%2C+213%E2%80%93237&btnG= (accessed Apr. 18, 2023).

[49] G. K. Sigworth, "The modification of Al-Si alloys: Important practical and theoretical aspects," *International Journal of Metalcasting*, vol. 2, no. 2, pp. 19–40, 2008, doi: 10.1007/BF03355425.

[50] "Iwahori, H. & Yonekura, K. & Yamamoto, Y. & Nakamura,... - Google Akademik." https://scholar.google.com/scholar?hl=tr&as_sdt=0%2C5&q=Iwahori%2C+H.+%26+Yonekura%2C+K.+%26+Yamamoto%2C+Y.+%26+Nakamura%2C+M..+%281990%29.+Occuring+Behaviour+Of+Porosity+And+Feeding+Capabilities+Of+Sodium+And+Strontium+Modified+Al-Si+Alloys.+Afs+Trans..+98.+167-173.&btnG= (accessed Apr. 18, 2023).

[51] "Fang, Q. T.; Granger, D. A. Porosity Formation In... - Google Akademik." https://scholar.google.com/scholar?hl=tr&as_sdt=0%2C5&q=Fang%2C+Q.+T.%3B+Granger%2C+D.+A.+Porosity+Formation+In+Modified+And+Unmod

ified+A356+Alloy+Castings.+Afs+Trans%2C+1989%2C+97.10%3A+989-1000.&btnG= (accessed Apr. 18, 2023).

[52] A. Knuutinen, K. Nogita, S. McDonald, A. D.-J. of light metals, and undefined 2001, "Modification of Al–Si alloys with Ba, Ca, Y and Yb," *Elsevier*, Accessed: Apr. 18, 2023. [Online]. Available: https://www.sciencedirect.com/science/article/pii/S1471531702000044

[53] S. Shankar, Y. Riddle, M. M.-A. Materialia, and undefined 2004, "Nucleation mechanism of the eutectic phases in aluminum–silicon hypoeutectic alloys," *Elsevier*, 2004, doi: 10.1016/j.actamat.2004.05.045.

[54] S. D. McDonald, A. K. Dahle, J. A. Taylor, and D. H. StJohn, "Eutectic grains in unmodified and strontium-modified hypoeutectic aluminum-silicon alloys," *Metall Mater Trans A Phys Metall Mater Sci*, vol. 35 A, no. 6, pp. 1829–1837, 2004, doi: 10.1007/S11661-004-0091-Y.

[55] K. Nogita, H. Yasuda, K. Yoshida, K. Uesugi, A. T.-S. materialia, and undefined 2006, "Determination of strontium segregation in modified hypoeutectic Al–Si alloy by micro X-ray fluorescence analysis," *Elsevier*, Accessed: Apr. 18, 2023. [Online]. Available: https://www.sciencedirect.com/science/article/pii/S1359646206005240

[56] C. Dinnis, A. Dahle, J. T.-M. S. and E. A, and undefined 2005, "Three-dimensional analysis of eutectic grains in hypoeutectic Al–Si alloys," *Elsevier*, Accessed: Apr. 18, 2023. [Online]. Available: https://www.sciencedirect.com/science/article/pii/S092150930401278X

[57] S. Z. Lu and A. Hellawell, "The mechanism of silicon modification in aluminum-silicon alloys: Impurity induced twinning," *Metallurgical Transactions A*, vol. 18, no. 10, pp. 1721–1733, Oct. 1987, doi: 10.1007/BF02646204.

[58] M. D. Hanna, S. Z. Lu, and A. Hellawell, "MODIFICATION IN THE ALUMINUM SILICON SYSTEM.," *Metallurgical transactions. A, Physical*

metallurgy and materials science, vol. 15 A, no. 3, pp. 459–469, 1984, doi: 10.1007/BF02644969.

[59] L. Bolzoni and N. Hari Babu, "Efficacy of Borides in Grain Refining Al-Si Alloys," *Metall Mater Trans A Phys Metall Mater Sci*, vol. 50, no. 2, pp. 746–756, Feb. 2019, doi: 10.1007/s11661-018-5017-1.

[60] M. Nowak, L. Bolzoni, and N. Hari Babu, "Grain refinement of Al-Si alloys by Nb-B inoculation. Part I: Concept development and effect on binary alloys," *Mater Des*, vol. 66, no. PA, pp. 366–375, Feb. 2015, doi: 10.1016/j.matdes.2014.08.066.

[61] L. Bolzoni, M. Nowak, and N. Hari Babu, "Grain refinement of Al-Si alloys by Nb-B inoculation. Part II: Application to commercial alloys," *Mater Des*, vol. 66, no. PA, pp. 376–383, Feb. 2015, doi: 10.1016/j.matdes.2014.08.067.

[62] L. Bolzoni, M. Nowak, and N. Hari Babu, "Assessment of the influence of Al-2Nb-2B master alloy on the grain refinement and properties of LM6 (A413) alloy," *Materials Science and Engineering A*, vol. 628, pp. 230–237, Mar. 2015, doi: 10.1016/j.msea.2015.01.053.

[63] Y. Li, B. Hu, Q. Gu, B. Liu, and Q. Li, "Achievement in grain-refining hypoeutectic Al-Si alloys with Nb," *Scr Mater*, vol. 160, pp. 75–80, Feb. 2019, doi: 10.1016/j.scriptamat.2018.09.037.

[64] M. Nowak, W. K. Yeoh, L. Bolzoni, and N. Hari Babu, "Development of Al-Nb-B master alloys using Nb and KBF4 Powders," *Mater Des*, vol. 75, pp. 40–46, Jun. 2015, doi: 10.1016/j.matdes.2015.03.010.

[65] M. Easton and D. St John, "An analysis of the relationship between grain size, solute content, and the potency and number density of nucleant particles," *Metall Mater Trans A Phys Metall Mater Sci*, vol. 36, no. 7, pp. 1911–1920, 2005, doi: 10.1007/S11661-005-0054-Y/METRICS.

[66] Y. Li, Y. Jiang, B. Hu, and Q. Li, "Novel Al-Ti-Nb-B grain refiners with superior efficiency for Al-Si alloys," *Scr Mater*, vol. 187, pp. 262–267, Oct. 2020, doi: 10.1016/j.scriptamat.2020.06.037.

[67] D. Wu *et al.*, “Revealing the mechanism of grain refinement and anti Si-poisoning induced by (Nb, Ti)B2 with a sandwich-like structure,” *Acta Mater*, vol. 219, Oct. 2021, doi: 10.1016/j.actamat.2021.117265.

[68] Y. Li, Y. Jiang, B. Liu, Q. Luo, B. Hu, and Q. Li, “Understanding grain refining and anti Si-poisoning effect in Al-10Si/Al-5Nb-B system,” *J Mater Sci Technol*, vol. 65, pp. 190–201, Feb. 2021, doi: 10.1016/j.jmst.2020.04.075.

[69] J. Xu *et al.*, “In-situ observation of grain refinement dynamics of hypoeutectic Al-Si alloy inoculated by Al-Ti-Nb-B alloy,” *Scr Mater*, vol. 187, pp. 142–147, Oct. 2020, doi: 10.1016/j.scriptamat.2020.06.020.

[70] L. Aydin, H. S. Artem, and S. Oterkus, *Designing engineering structures using stochastic optimization methods*.

[71] E. Kocaman, S. Şirin, and D. Dispinar, “Artificial Neural Network Modeling of Grain Refinement Performance in AlSi10Mg Alloy,” *International Journal of Metalcasting*, vol. 15, no. 1, pp. 338–348, Jan. 2021, doi: 10.1007/s40962-020-00472-9.

[72] I. Ghosh, S. K. Das, and N. Chakraborty, “An artificial neural network model to characterize porosity defects during solidification of A356 aluminum alloy,” *Neural Comput Appl*, vol. 25, no. 3–4, pp. 653–662, 2014, doi: 10.1007/s00521-013-1532-6.

[73] S. H. M. Anijdan, A. Bahrami, H. R. M. Hosseini, and A. Shafyei, “Using genetic algorithm and artificial neural network analyses to design an Al-Si casting alloy of minimum porosity,” *Mater Des*, vol. 27, no. 7, pp. 605–609, 2006, doi: 10.1016/j.matdes.2004.11.027.

[74] J. Antony, “Design of experiments for engineers and scientists,” 2014, Accessed: Apr. 19, 2023. [Online]. Available: https://books.google.com/books?hl=tr&lr=&id=p7pCAgAAQBAJ&oi=fnd&pg=PP1&dq=Antony,+J.+2014.+Design+of+Experiments+for+Engineers+and+Scientists.+2nd+Edition.+Elsevier,+London.&ots=BEvWYXtzGs&sig=LZRAGaE9k4bwks9kMvQ3WtxxNCE

[75] D. Montgomery, G. Runger, and N. Hubele, “Engineering statistics,” 2009, Accessed: Apr. 19, 2023. [Online]. Available: https://books.google.com/books?hl=tr&lr=&id=O-XmUTtpgSUC&oi=fnd&pg=PA488&dq=Montgomery,+D.C.,+Runger,+G.C.+and+Hubele,+N.F.+2010.+Engineering+Statistics.+5th+Edition.+John+Wiley+and+Sons,+USA.&ots=B_O6CI5uQ2&sig=RGjJtqRWGoSgvuwJ-Z9ELO6-Zyc

[76] J. Xu, Y. Li, B. Hu, Y. Jiang, and Q. Li, “Development of Al–Nb–B master alloy with high Nb/B ratio for grain refinement of hypoeutectic Al–Si cast alloys,” *J Mater Sci*, vol. 54, no. 23, pp. 14561–14576, Dec. 2019, doi: 10.1007/s10853-019-03915-9.

[77] L. Bolzoni and N. Hari Babu, “On the grain refining efficacy of Ti-free hypoeutectic AlSi via AlTiB, AlB and AlNbB chemical inoculation,” *J Alloys Compd*, vol. 817, Mar. 2020, doi: 10.1016/j.jallcom.2019.152807.

[78] “M. Drouzy, S. Jacob, and M. Richard: AFS Int. Cast... - Google Akademik.” https://scholar.google.com/scholar?hl=tr&as_sdt=0%2C5&q=M.+Drouzy%2C+S.+Jacob%2C+and+M.+Richard%3A+AFS+Int.+Cast+Met.+J.%2C+1980%2C+vol.+5%2C+pp.+43%E2%80%9350&btnG= (accessed Jun. 15, 2023).

[79] “D. C. Montgomery (1991) Design and Analysis of Experimen... - Google Akademik.” https://scholar.google.com/scholar?hl=tr&as_sdt=0%2C5&q=+D.+C.+Montgomery+%281991%29+Design+and+Analysis+of+ExperimentsThird+Edition%2C+John+Wiley+%26+Sons.&btnG= (accessed Jun. 19, 2023).

[80] J. Xu, R. Li, and Q. Li, “Effect of Agglomeration on Nucleation Potency of Inoculant Particles in the Al-Nb-B Master Alloy: Modeling and Experiments,” *Metall Mater Trans A Phys Metall Mater Sci*, vol. 52, no. 3, pp. 1077–1094, Mar. 2021, doi: 10.1007/s11661-020-06123-2.

Curriculum Vitae

Name Surname : Batuhan Doğdu

Education:

2016–2020 İzmir Kâtip Çelebi University, Dept. of Material Science and Eng., Undergraduate Degree

2020–2023 İzmir Kâtip Çelebi University, Dept. of Material Science and Eng., Master's Degree

Work Experience:

2019 –Current CMS Jant ve Makina Sanayi A.Ş.

Publications (if any):

1. 11. International Congress of Academic Research (ICAR'11), "Effect of Nb, Ti and B Element Ratios On the Grain Size of A356 Castings and Optimization by Multiple Regression Method", Paper ID: 190.